UC Santa Cruz

UC Santa Cruz Electronic Theses and Dissertations

Title

Advanced Electrode Materials for Electrochemical Energy Storage Devices

Permalink

https://escholarship.org/uc/item/9dg1693g

ISBN

9798293872428

Author

Pinongcos, Anica

Publication Date

2025-08-28

Peer reviewed|Thesis/dissertation

eScholarship.org Powered by the California Digital Library
University of California

UNIVERSITY OF CALIFORNIA

SANTA CRUZ

Advanced Electrode Materials for Electrochemical Energy Storage Devices

A dissertation submitted in partial satisfaction
of the requirements for the degree of

DOCTOR OF PHILOSOPHY

in

CHEMISTRY

by

Anica Bagamaspad Pinongcos

September 2025

The Dissertation of Anica Bagamaspad Pinongcos is approved:

Professor Yat Li, Chair

Professor Alexander Ayzner

Professor Scott Oliver

Peter F. Biehl

Vice Provost and Dean of Graduate Studies

Copyright © by

Anica Bagamaspad Pinongcos

2025

Table of Contents

List of Figures v

List of Tables ix

Abstract x

Dedication xii

Acknowledgements xiii

Chapter 1-Introduction 1

1.1 Abstract 1

1.2 Background 2

1.3 Types of Common EES devices' Electrode 3

1.3.1 Battery Electrodes 4

1.3.2 Supercapacitor Electrodes 5

1.4 Low Temperature Energy Storage Electrodes 8

1.4.1 Limiting Factors of Low Temperature Electrodes 9

1.5 Mechanically Robust Electrochemical Energy Storage Electrodes 19

1.6 References 21

Chapter 2-Nitrogen-Enriched Carbon Electrode with High Capacitance Retention for Low Temperature Energy Storage 31

2.1 Abstract 31

2.2 Introduction 32

2.3 Experimental 34

2.4 Results and Discussion 38

2.5 Conclusion 60

Table 2.1. 61

Table 2.2. 62

2.6 References 63

Chapter 3- Mechanically Reinforced 3D-Printed Graphene Aerogel Electrodes vis Covelent Crosslinking 69

3.1 Abstract 69
3.2 Introduction 70
3.3 Experimental 72
3.4 Results and Discussion 75
3.5 Conclusion 89
3.6 References 91
Chapter 4-Electrochemcial Behavior of Electrodeposited γ- and ε- Manganese dioxide in Aqueous and Non-aqueous Systems 96
4.2 Introduction 97
4.3 Experimental 99
4.4 Results and Discussions 102
4.5 Conclusion 116
4.6 References 117
Chapter 5- Outlook 121
5.2 References 125

List of Figures

Chapter 1

Figure 1.1. General overview of different types of EES device.

Figure 1.2. Schematic illustration of energy storage mechanisms for batteries, electric double layer capacitors, and pseudocapacitors.

Figure 1.3. Effect of decreasing the operating temperature on the electrode–electrolyte interfaces.

Figure 1.4. Schematic illustration of ion diffusion mechanisms with and without a vacancy involved.

Figure 1.5. Ionic mobility is based on the pore size of the electrode.

Figure 1.6. Mechanically robust electrochemical energy storage electrodes.

Chapter 2

Figure 2.1. Schematic illustration of fabricating nitrogen doped multiscale porous carbona aerogel electrodes.

Figure 2.2. Scanning electron microscope images of multiscale carbon aerogels (MCA) and nitrogen doped multiscale carbon aerogels (N-MCA).

Figure 2.3. Energy dispersive X-ray spectroscopy (EDS) elemental mapping images of N-MCA and XPS spectra of MCA and N-MCA.

Figure 2.4. Gravimetric capacitance of N-MCA and MCA electrodes.

Figure 2.5. Device performance of MCA and N-MCA at room temperature.

Figure 2.6. Cyclic voltammetry (CV) and galvanostatic charging and discharging (GCD) curves of N-MCA and MCA collected at -40°C, respectively.

Figure 2.7. Device performance of MCA and N-MCA at -40°C.

Figure 2.8. XPS spectra of N-MCA electrodes.

Figure 2.9. Nitrogen absorption–desorption isotherm and pore size distribution profile of N-MCA treated at different temperatures.

Figure 2.10. Gravimetric capacitance of MCA, N-MCA-700, N-MCA-800, N-MCA-900, and N-MCA-1000 electrodes.

Figure 2.11. Device performance of MCA, N-MCA-700, N-MCA-800, N-MCA-900, and N-MCA-1000

Figure 2.12. Electrochemical surface area of MCA, N-MCA-700, N-MCA-800, N-MCA-900, and N-MCA-1000.

Figure 2.13. CV curves and histogram illustrations of *b*-values of MCA, N-MCA-800, and N-MCA-1000.

Figure 2.14. Plot of areal capacitance vs. $v^{-1/2}$ for MCA, N-MCA-800, and N-MCA-1000. Histogram illustration of capacitance contributions in MCA, N-MCA-800, and N-MCA-1000 at a scan rate of 5 mV s^{-1}.

Figure 2.15. Volumetric energy and power densities of symmetric device with N-MCA-800 and N-MCA-1000 electrodes tested at 20 and -40 °C.

Chapter 3

Figure 3.1. Schematic illustration of fabrication of 3D printed gelled graphene aerogel (3D gelled GA).

Figure 3.2. SEM and STEM images of 3D gelled GA.

Figure 3.3. Surface characterization of 3D gelled GA via SEM, XPS, and contact angle analysis.

Figure 3.4. Electrochemical performance of 3D gelled GA electrode.

Figure 3.5. Electrochemical performance of 3D gelled GA symmetric device.

Figure 3.6. Electrochemical performance of 3D gelled GA symmetric device at different temperatures.

Figure 3.7. Conductance and electrochemical performance of 3D gelled GA at different bending states.

Figure 3.8. SEM images of 3D gelled GA before and after applied compression.

Figure 3.9. Electrochemical performance of 3D gelled GA symmetric device der different applied pressure.

Chapter 4

Figure 4.1. Schematic illustration of CC/γ-MnO_2 and CC/ε-MnO_2 fabrication.

Figure 4.2. Top view SEM images of CC/ε-MnO_2 and CC/γ-MnO_2 at different magnification.

Figure 4.3. Cross-section SEM images of CC/γ-MnO_2 and CC/ε-MnO_2.

Figure 4.4. SEM and EDS images of CC/ε-MnO_2 and CC/γ-MnO_2.

Figure 4.5. HRXRD of γ-MnO_2 and ε-MnO_2 electrodeposited on a carbon substrate.

Figure 4.6. Electrochemical performance of CC/γ-MnO_2 and CC/ε-MnO_2 in aqueous system.

Figure 4.7 Digital images of CC/ε-MnO_2 and CC/γ-MnO_2 after electrochemical testing.

Figure 4.8. Nyquist plot of CC/ε-MnO_2 and CC/γ-MnO_2 in 3M LiCl.

Figure 4.9. Plot of areal capacitance versus $\nu^{-1/2}$ for CC/ε-MnO_2 and CC/γ-MnO_2. Histogram illustration of capacitance contributions in CC/ε-MnO_2 and CC/γ-MnO_2 at a scan rate of 1 mV s^{-1} and 5 mV s^{-1}.

Figure 4.10. Electrochemical performance of CC/γ-MnO_2 and CC/ε-MnO_2 in non-aqueous system.

List of Tables

Chapter 2

Table 2.1 The electrochemical performance of other carbon-based electrodes at -40°C.

Table 2.2. Electrode characteristic values derived through analysis of the constant phase element (CPE, Q) from the equivalent circuit modeling of the electrochemical impedance spectroscopy data.

Abstract

Advanced Electrode Materials for Electrochemical Energy Storage Devices

by

Anica Bagamaspad Pinongcos

With the ever-increasing demand for portable electronic technologies, the development of new electrochemical energy storage (EES) devices such as supercapacitors and batteries that could withstand extreme conditions is urgently needed. Currently, the commercially available EES devices often suffer sever loss of energy and power densities under extreme operating temperatures and application of external mechanical deformation. These extreme conditions normally posed challenges on EES devices, limiting their applications. The electrodes are determined to play an important role in the overall performance of the EES devices. The specific capacity, rate capability, and energy and power densities of EES devices all depend on the electrode used. This dissertation covers different design and optimization strategies to enhance the performance of EES devices and broaden their application to extreme operating conditions.

The 1st Chapter presents the background for energy storage, the different types of EES devices' electrode, and their applications at extreme conditions. The goal of this section is to create a general framework for these two key research directions in energy storage. The 2nd Chapter focuses on enhancing the surface chemistry of the porous electrode for low temperature supercapacitors. In this chapter we explored how introducing nitrogen dopant can increase capacitance and achieve high retention even

at low operating temperature of -40°C. The 3rd Chapter addresses the challenge of mechanical integrity in 3D printed carbon aerogel electrodes which limit its practical application. In this chapter, we present a new ink formulation that enhances the mechanical properties of the resulting carbon aerogels. The 4th Chapter discusses the impact of manganese oxide polymorphism on electrochemical performance in aqueous and non-aqueous system. In this chapter, we aim to address how the structural characteristics of electrodeposited manganese oxide—specifically its crystal phase, crystallinity, and crystal size—affect its electrochemical performance in energy storage devices like batteries and supercapacitors. Lastly, 5th Chapter provides overview of challenges and perspective research directions for the advancement of EES devices.

Dedication

This dissertation is dedicated to my parents, Anita and Narciso Pinongcos, my grandparents, Australis and Alicia Bagamaspad, and my siblings, Angelica and Dan Pinongcos.

Acknowledgements

I honestly don't know how to write this part of my thesis without being too emotional and knowing it's the part most people read adds extra pressure. Throughout the years there are so many people I want to acknowledge, and words can't describe how grateful I am towards them. It may sound cliché, but every single one of them shaped me into the person I am today.

Everyone says it takes a village to raise a child. It may sound bizarre, but I believe it also takes a village to train someone to be a scientist. Teaching and training, especially in a field that is unfamiliar, requires patience and dedication. I am forever thankful for the knowledge, support, and motivation I have received throughout my PhD journey. First and foremost, I want to sincerely thank my advisor, Prof. Yat Li, for patiently guiding me through the challenges of graduate school. When I started UCSC during the pandemic, I felt lost and uncertain about what to expect from graduate school. Prof. Yat Li, you greatly helped me in establishing a strong foundation in the field of energy storage research. You have trained me to think critically, work independently, and appreciate the values of science inside and outside the lab. You exemplify what it means to be both a great mentor and a dedicated scientist. You always remind each one of us that life is more than any science experiment. You are a great inspiration to us all, especially to your students. I'm grateful and proud to be part of the Li Research Group! It was one of the best decisions I made.

I would like to thank the other members of my committee, Prof. Alexander Ayzner and Prof. Scott Oliver, for guiding me through my 2nd year seminar, and

qualification exam. Thank you, Prof. Oliver, for helping me with the XRD analysis. Thank you, Prof. Ayzner, for guiding me through my qualification exam and reminding me to identify the fundamental question on each research proposal I present. I would like to thank my outside member of my committee, Dr. Tyson Back, for guiding me through the field emission research area and offering me opportunity to work at the Air Force Research Laboratory (AFRL). My experience at AFRL offered me a unique opportunity to learn and work in an interdisciplinary research environment outside the conventional academic setting. I learned a lot of synthesis and characterization techniques that I would not have a chance to learn at my home institution. I would like to thank Dr. Ali Sayir of Air Force Office of Scientific Research for connecting with the AFRL and introducing us to the NSF-AFRL program. No words can describe how grateful I am for connecting our team to AFRL.

Thank you to our collaborators at Lawrence Livermore National Laboratory (LLNL), especially Dr. Marcus A. Worsley and Dr. Swetha Chandrasekaran, whose guidance and support played an essential role in the completion of my PhD. My three summer internships were an extraordinary experience. Dr. Chandrasekaran, thank you so much for being my mentor. It's been an honor working with you. I can't believe I learned ink formation and 3D printing of energy storage from one of the world-renowned scientists. I also want to thank AESTEC Team from LLNL: Dr. Marissa Wood, Dr. Christine Orme, Dr. Seongkoo Cho, Dr. Nicholas Brady, Dr. Jianchao Ye, and Asya Orhan; and from UCLA: Prof. Bruce Dun, Makena White, Bintao Hu, and Minseok Choi. It was a pleasure working with you all.

To the former members of Li Research Groups; Dr. Tianyi Kou, Dr. Mingpeng Chen, Dr. Shanwen Wang, Dr. Megan Frayman, and Dr. Dun Lin thank you for welcoming me at the lab and passing the knowledge. Energy storage was very new to me when I started at the lab. Your patience in teaching me the fundamentals made all the difference. I would like to thank the current members of the lab: Xinzhe Xue, Samuel Eisenberg, Qiu Ren, Nathan Delaney, Cassidy Tran, and Ella Davidi. Over the past years, you have witnessed both my lowest moments and my proudest achievements. I can't thank you guys enough for being there for me throughout the years. You made my whole PhD journey memorable. I feel so fortunate to have you not only as labmates but also as lifelong friends. I also would like to thank my former undergraduate students, Frances Li, Eric Po Ching Hsu, Emma Coester, and Cathleen Hsieh, for your contributions. Your curious minds helped me understand the fundamentals of energy storage. I wish you guys all the best.

I would like to thank my peers from current and past members of Ayzner's lab: Rachel Richards, Ivette Mora, Julia Penick, Matt Bittner, Jameson Spence, and Dr. Anna Johnston; from the Zhang's lab: Kai Chun (Kevin) Chou, Mariam Khvichia, David Zeitz, Dr. Vivien Cherrette, and Dr. Malissa Guarino-Hotz; from Oliver's lab: Riley Ball; from MacMillian lab: Riley Blue; from Braslau Lab: Chayo Fuentes and Gabriel Parkinson; and from Wang Lab: Jorge Ruiz Gonzalez. It has been an honor to know and work alongside you all. I want to thank the professors of the UCSC Department of Chemistry and Biochemistry: Prof. Xiao Wang, Prof. Rebecca Braslau,

Prof. Timothy Johnstone and Prof. Jin Z. Zhang, for the knowledge you shared with me.

To my former mentors at UCLA — Prof. Sarah H. Tolbert, Dr. Jeff Kurish, and Dr. Stephen Sasaki — thank you for opening the door to research for me. Without your guidance, I would not have had the chance to begin this journey.

My lifelong friends—Dr. Shirley Chang, Dr. Joseph Nguyen, Dr. Madeline Riffel, Dewi Ramlan, and Daniel Kim—thank you for being there since undergraduate. Chemistry wouldn't be enjoyable without you guys.

To Michael Feany, thank you so much for your unwavering support. From dropping me off in Santa Cruz, Ohio, and then later in Livermore to listening patiently to my stories about daily life in the lab, you have always been there for me. Thank you for going on adventures with me. I can't wait for what life holds for us.

Last but not the least, I would like to thank my family. I would like to thank my mom, Dr. Anita Pinongcos, my uncle, Dr. Alfredo Bagamaspad, my aunt, Dr. Arlene Bagamaspad, and my grandma, Alicia Bagamaspad, for their love and care. Thank you for the sacrifice you made just for us to have a better life in the US. To my siblings, Angelica and Dan Pinongcos, thank you for supporting me. I am sure dad is so proud of us.

This dissertation includes reprints of the previously published material:

1. **Pinongcos, A. B.**, Xue, X., Chandrasekaran, S., Worsley, M. A. & Li, Y. Innovative Electrode Design for Low-Temperature Electrochemical Energy Storage: A Mini Review. *Energy Fuels* **39**, 6078–6096 (2025).
2. **Pinongcos, A. B.**, Xue, X., Freyman, M. C., Cho, S., Chandrasekaran, S., Ren, Q., Delaney, N., Coester, E., Woods, M., Worsley, M. A., & Li, Y. Nitrogen-Enriched Carbon Electrode with High Capacitance Retention for Low-Temperature Energy Storage. (In preparation).
3. **Pinongcos, A. B.** †, Chandrasekaran, S † (equal contribution), Freyman, M. C., Xue, X., Worsley, M. A. & Li, Y. Mechanically Reinforced 3D-Printed Graphene Aerogel Electrodes via Covalent Crosslinking. (In preparation).

Chapter 1
Introduction on Electrochemical Energy Storage Electrodes

1.1 Abstract

As the demand for portable technologies rises, there is a pressing need for EES devices with wide temperature tolerance and those with mechanically flexibility. Commercially avaible EES devices often suffer sever loss of energy and power densities under extreme operating temperatures and application of external mechanical deformation. These elevated conditions normally posed challenges on EES devices which hinder their wide range of applications. Supercapacitors and batteries are two leading EES devices and the most investigated system. However, the increasing demand requires improvements in their performance. While electrolyte research has garnered significant attention, electrode design is equally critical for enhancing the performance of EES devices. In this chapter, the background for energy storage, the types of EES devices' electrode, and their applications at extreme conditions were presented. The goal of this section is to create a general framework for these two key research directions in energy storage.

1.2 Background

Electrochemical energy storage (EES) devices are essential to our daily lives, and their demand continues to rise. Extensive efforts have been devoted to match this growing demand for state-of-the-art technologies. Currently, the development of electrodes with wide temperature tolerance and those with mechanically flexibility are two key research directions in energy storage.

For wide temperature energy storage applications, low-temperature energy storage systems are particularly critical for human exploration in the polar regions and celestial bodies in outer space, where average temperatures drop below −60 °C.[1,2] However, commercial energy storage devices, such as batteries and supercapacitors, are typically designed to operate within a low temperature range of −20 to −40 °C.[3–5] Further decreasing the operating temperature presents significant challenges.

To enhance the performance of EES devices at low temperatures, some researchers incorporate external or self-heating components into the devices to enable operation under such conditions.[1,6,7] For instance, the battery cells used in the 2012 Mars Curiosity rover were equipped with onboard radioisotope heating systems to ensure stable operation from −20 to 30 °C.[1] While effective, this strategy increases both the mass and the cost of the devices. Alternatively, researchers over the past decade have focused on developing electrolytes with improved properties for low-temperature operation.[8,9] Ideal low-temperature electrolytes should have a low viscosity, a high dielectric, and a wide electrochemical stability window. While electrolyte research on

low temperature has garnered significant attention, electrode design is equally critical for enhancing the performance of low-temperature energy storage systems.

Another highly active research area is the development of electrode with high mechanical integrity. Development of flexible energy storage devices has gained significant attention due to the demand for wearable devices, bendable phones, roll-up displays, and medical devices.[10,11] In a conventional energy storage device, the electrodes hinder the flexibility of it. In general, electrodes are made out of rigid materials that could be easily damage and diminished the performance when an external force such as bending applies.[12] Numerous works both experimentally and theoretically simulation have been conducted in the past to the study the effect of external force on the electrochemical energy storage.[13,14] In turns out, the most common factors on limiting the mechanical integrity of the common electrodes is the absence of plastic flow, high stress level.[15] Overall, electrodes with superior mechanical integrity and highly conductivity are much needed to develop the next generation technology.

1.3 Types of Common EES devices' Electrode

There are four main EES device capacitors, fuel cells, batteries, and supercapacitors. All of these rely on electrochemical processes that occurred during the chemical reaction and share similar configurations, consisting of two electrodes separated by a porous separator and filled with an electrolyte containing charge-carrying ions.[16] However, their different charge-storage properties draw a distinction which can be easily compared through the Ragone-plot (**Figure 1.1a**).[17] In this plot,

the energy density is the amount of energy that can be stored in a mass, area, or volume. Meanwhile, power density is the speed at which the energy is stored. Among the four EES devices, batteries and supercapacitors are the two leading energy storage devices which can be categorized based on the mode of charge storage (**Figure 1.1b**).[18] Although fuel cells have high energy densities compared to batteries and supercapacitors, these devices are less desirable in the market due to the cost and slow transient response.[19]

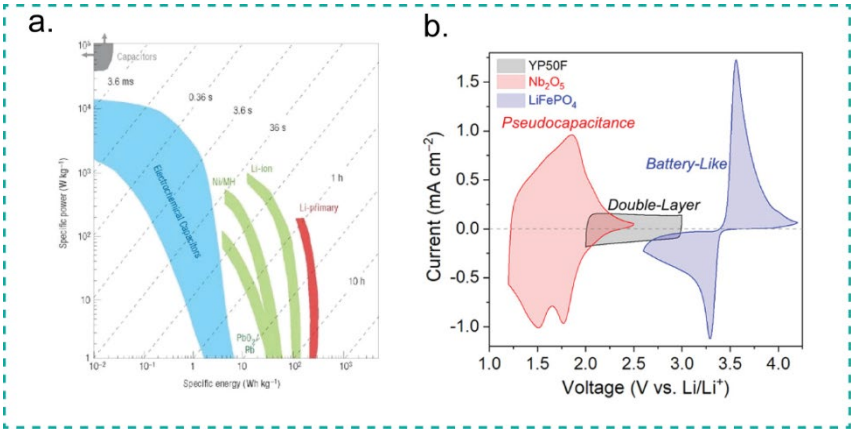


Figure 1.1 (a) Ragone plot different energy storage. Reproduced from ref (17). Copyright 2008, Springer Nature. (b) Cyclic voltammogram curves of battery-like, pseudocapacitance, and double-layer electrodes. Reproduced from ref (18). Copyright 2020, American Chemical Society.

1.3.1 Battery Electrodes

In batteries such as lithium-ion batteries (LIBs), charge is stored through the intercalation and deintercalation of ions, a faradaic process involving charge transfer at the electrode-electrolyte interface (redox). [20–22] During charging, electrons and Li ions

are simultaneously released from the cathode. The Li ions pass through the cathode–electrolyte interphase (CEI), solvated with the solvent molecules and anions in the bulk electrolyte. Before entering the solid–electrolyte interface (SEI) at the anode's surface, the Li ions need to undergo desolvation (**Figure 1.2a**). They are then intercalated into the anode material. This process is reversed during discharge.

1.3.2 Supercapacitor Electrodes

Supercapacitors are EES devices that bridge the gap between the capacitors and batteries. These devices can charge and discharge fast and store sufficient amounts of energy. Supercapacitors can be categorized into two: electrical double layer capacitors (EDLC).

1.3.2.1 Electrical Double Layer Capacitors (EDLC) Electrodes

EDLCs store charges on electrode surfaces through non-Faradaic reactions, via physical adsorption/desorption of ions, which leads to high power density (**Figure 1.2b**).[23] During charging, solvated cations and anions diffuse to the negative and positive electrodes, respectively, producing a Helmholtz double layer capacitance. Over the years, the Helmholtz double layer capacitance model was later refined by Gouy and Chapman, and Stern and Geary. Both models suggested the presence of the diffuse layer in the electrolyte due to the accumulation of ions near the electrode surface. These models guided researchers on understanding and further developing EDLC devices.

Carbon based materials such as graphene oxide, carbon nanotubes, and activated carbon are commonly used as EDLC electrodes. These materials generally have high electrical conductivity, low cost, and are chemically and thermally stable. Since EDLCs' performance depends on the absorption of ions on a high specific surface area of the electrode, many efforts on enhancing the capacitance of it are through increasing the pore volume. Some studies suggested that capacitance has no linear relationship with surface area of the electrode. Since not all pores are accessible to ions, the sizes of the pore and the ion need to be considered in designing porous electrodes.

1.3.2.2 Pseudocapacitors

Pseudocapacitors store charges through surface-controlled, kinetically fast Faradaic redox reactions. [23–25] There are three reversible redox mechanisms that contribute to pseudocapacitance: underpotential deposition, surface redox reactions, and rapid insertion/desertion of electrolyte ions into the active material, similar to the intercalation/deintercalation process in LIBs (**Figure 1.2c**).[25,26] However, unlike batteries, pseudocapacitors do not undergo phase changes during charge storage.

Manganese oxide (MnO_2) is one of the common pseudocapacitive materials that was first investigated by Lee and Goodenough in 1999.[27] This is one of the most promising electrode materials because of its an earthly abundant, low cost, environmental friendliness and high theoretical specific capacitance of 1370 F g^{-1}.[28] MnO_2 involves a charge storage mechanism of ion intercalation and deintercalation accompanied with one electron redox of Mn between the +4 and +3 oxidation. [25,29]

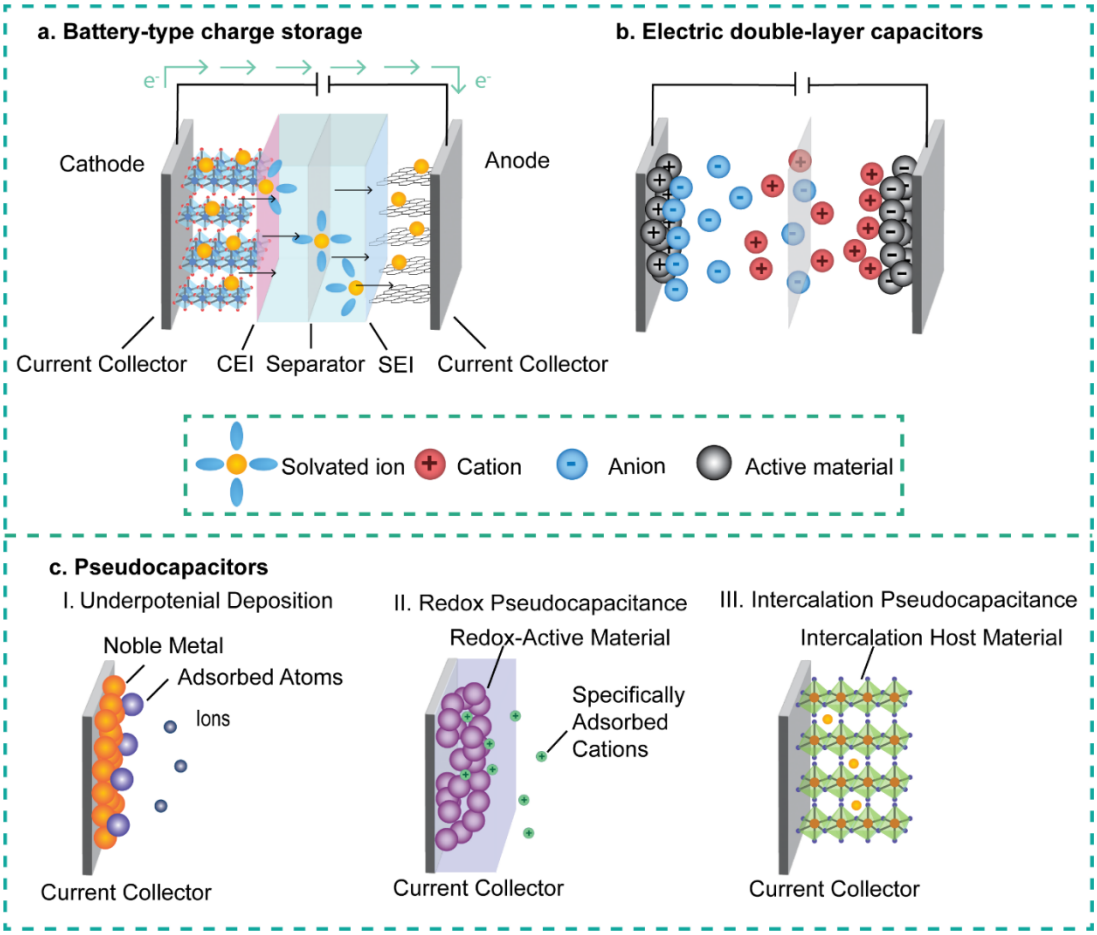


Figure 1.2. Schematic illustration of energy storage mechanisms for (a) batteries, (b) electric double layer capacitors, and (c) pseudocapacitors. Reproduced from (30). Copyright 2025, American Chemical Society.

1.4 Low Temperature Energy Storage Electrodes

The performance of EES electrodes is highly dependent on operating temperature, as described by the Arrhenius equation:

$$k = A\, e^{-E_a/RT} \qquad \textbf{(Eq. 1.1)}$$

where k is the rate constant, A is the pre-exponential factor, Ea is the activation energy, R is the ideal gas constant, and T is the absolute temperature. According to this equation, the reaction rate decreases exponentially as the temperature decreases due to an increase in the energy barrier. At low temperatures, the ionic conductivity of the electrolyte decreases because of increased viscosity and slower ion mobility.[9,31] Common strategies to improve EES low-temperature performance include using organic solvents with low freezing points, increasing salt concentration, and adding additives to prevent freezing and enhance ion mobility.[31] Beyond the electrolyte, the performance of EES devices at low temperatures is also heavily influenced by the electrodes. Although the pre-exponential factor (A) can also exhibit temperature dependence, most experimental studies on low-temperature energy storage treat it as constant. This might be due to the difficulty of isolating it experimentally, and the activation energy typically has a much stronger influence on the temperature dependence of charge-transfer kinetics. Over the past decade, researchers have been working to overcome the limitations that hinder EES performance at low temperatures. Various experimental characterization techniques have been utilized to investigate the performance of the EES electrode at low operating temperatures. Electrochemical

techniques such as cyclic voltammetry, chronopotentiometry, and electrochemical impedance spectroscopy were employed to analyze ion diffusion, chemical reaction mechanisms, and kinetics influenced by the electrodes' structure and composition. [3,32,33]Microscopy techniques such as transmission electron microscopy and scanning electron microscopy provided visual insights into surface morphology and the crystallographic characteristic of the electrode–electrolyte interface and electrode materials. [3,34,35]

1.4.1 Limiting Factors of Low Temperature Electrodes

The performance of EES devices is directly proportional to the operational temperature. The key factors impacting electrode performance at low temperatures were identified as: (1) slow interfacial reaction kinetics, (2) sluggish ion diffusion through the bulk electrode, and (3) unfavorable electronic and ionic properties determined by the electrode's structure and composition.[20,30]

1.4.1.1 Slow Interfacial Reaction Kinetic

The first factor limiting the EES performance at low temperatures is the slow interfacial reaction kinetics. Xu et al. identified charge transfer at the electrode–electrolyte interface as the rate-limiting step (**Figure 1.3a**).[33] This process involves ion desolvation and migration within the solid-electrolyte interface (SEI). The complex structure of the SEI makes it challenging to separate the mechanisms of desolvation from the diffusion of Li^+ ion through the SEI.[20]

In a typical LIB, solvated ions must desolvate and migrate to the electrolyte/electrode interface before being intercalated into the electrode. Li et al. showed that the Li^+ desolvation process is the major kinetic barrier to Li^+ transport at low temperatures.[21] Xu et al. reported that at −70 °C, desolvation takes approximately 3 h to overcome a minimum energy barrier of 0.65 eV.[32] Desolvation, which involves stripping of a solvated Li^+, is an energy-intensive step, and this energy barrier becomes more significant as the temperature decreases.[21,33] Once desolvated, the ion migrates through the SEI layer to the electrode. The SEI layer, a thin electronically insulating film, forms as a result of electrolyte decomposition.[36,37] This layer consists of a porous organic layer (at the interface with electrolyte) and a compact inorganic layer (at the interface with the anode surface), allowing only Li^+ transport.[37,38] The SEI is believed to contribute to the irreversible capacity lost during the first cycle and capacity fading in subsequent cycles.[37] Lin et al., through density functional theory (DFT) calculations, discovered that only the initial capacity loss is due to the SEI's self-limiting electron tunneling properties, while the subsequent capacity fading may be caused by other electron transport mechanisms, such as defects and polarons.[37]

At low temperatures, the rate of ion transport through the SEI layer is reduced due to decreased kinetic energy, as described by the Arrhenius equation (**Eq. 1.1**). In addition, the low temperature changes the thermodynamics of electrolyte decomposition, leading to the formation of different intermediate products and insulating species that could increase guest ion transport resistance (**Figure 1.3b**).[36] These undesirable and uncontrollable reactions can result in dendrite

formation and reduce the device's lifecycle.[36,38] Previous works have shown that temperature plays an important role in formation of Li metal morphology on the surface of the lithium–metal battery (LMB) current collector.[35,39] Yan et al. and Thenuwara et al. observed that as temperature decreases, the size of Li nuclei decreases while nucleation density increases (**Figure 1.3c,d).**[34,35] This results in nonuniform Li growth on the current collector surface, eventually leading to inhomogeneous deposition and dendrite formation.

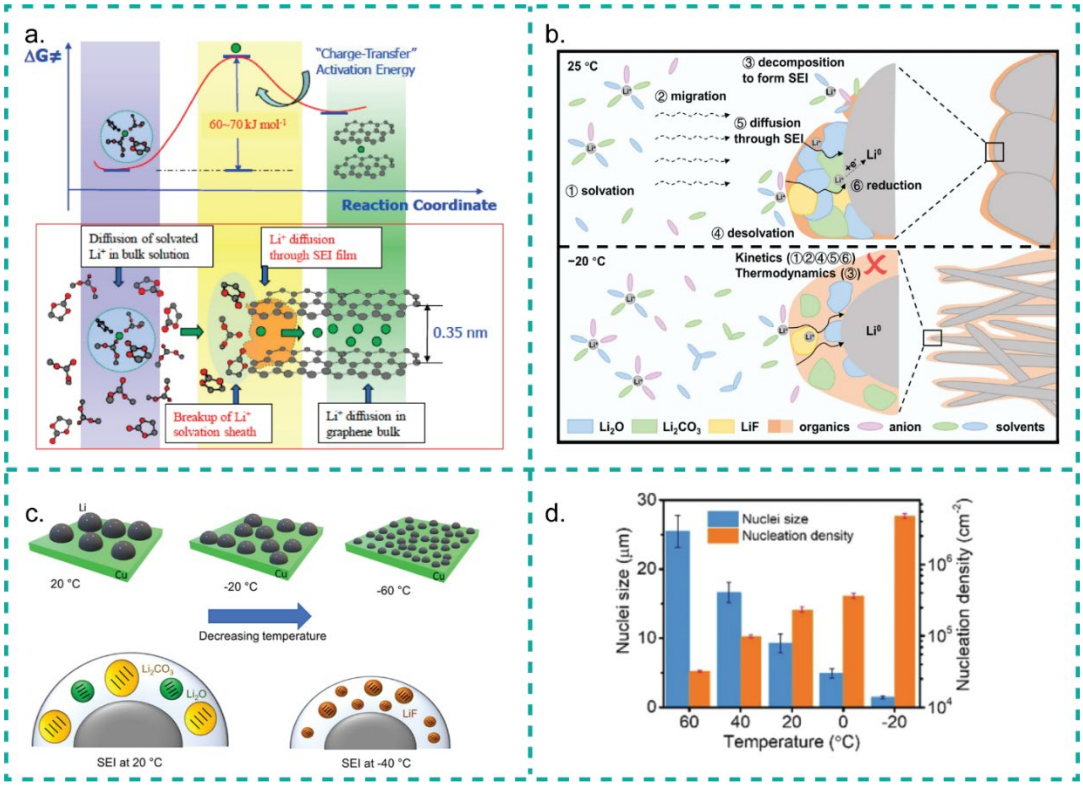


Figure 1.3. Effect of decreasing the operating temperature on the electrode–electrolyte interfaces. (a) Schematic illustration of the energy coordinate for solvated Li ion intercalation into a graphene structure showing that desolvation of ion is kinetically challenged process, usually characterized by an activation energy barrier. Reproduced

from ref (33). Copyright 2010 American Chemical Society. (b) Schematic illustration of ion diffusion during Li plating in LMB at 25 and −20 °C. Reproduced from ref (36). Available under a CC-BY 4.0 license. Copyright 2023, Nature Comm. (c) Schematic diagram showing changes in Li metal nucleation size, nucleation density, and SEI composition as a function of temperature. It shows the formation of dendrites at low temperatures is due to incomplete decomposition of the electrolyte. Reproduced from ref (35). Copyright 2019 American Chemical Society. (d) Histograms show Li nuclei size and nucleation density on the current collector surface at different operating temperatures. Reproduced with permission from ref (33). Copyright 2019 John Wiley and Sons.

1.4.1.2 Sluggish ion diffusion

The second factor that limits EES performance at low temperatures is the slow ion diffusion in solid-state electrodes. In battery systems such as LIBs, ions diffuse through the cathode's crystal structure after passing through the CEI during discharge. Ion diffusion, which is the transport of charged ions through an electrochemical system, influences both the charge–discharge rate and the electrochemical stability of the device. This process can be described by Ficks's law:

$$J = -D\nabla C \qquad \textbf{(Eq.1.2)}$$

where J is the particle flux, D is the diffusion coefficient, and C is the concentration. .[40,41] In liquid medium, ion diffusion is driven by the concentration gradient.[40] However, in solid medium such as EES electrodes, diffusion is also governed by the random motion of atoms, which can cause lattice distortion.[40] For ion

diffusion to occur, the adjacent site must be vacant, and the atom must have enough energy to overcome the energy barrier.[41,42] This process significantly affects ionic mobility and conductivity.[40] Ion diffusion mechanisms in solids are classified into two categories: nonvacancy/nondefect-mediated mechanism and vacancy/defect-mediated mechanism (**Figure 1.4**).[41,43] Of the two, the nonvacancy/nondefect-mediated mechanism requires lower activation energies due to weaker bonding of the interstitial atoms to neighboring atoms. In EES devices such as supercapacitors and LIBs, ion diffusion within the electrode primarily occurs via interstitial diffusion, where ions such as Li^+ move through the electrode's crystal structure.[42]

The rate of ion diffusion through the bulk electrode, regardless of the mechanism, is temperature-dependent and follows the Arrhenius equation (Eq. 1). At low operating temperatures, the cathode often experiences limited ion diffusion, leading to capacity degradation.[44,45] Lithium iron phosphate ($LiFePO_4$) is a widely used cathode for LIB due to its high theoretical capacity of ~170 mAh g^{-1} and a redox potential of 3.4 V vs Li/Li^+.[46] However, its low ion diffusivity (~10^{-14} cm^2 S^{-1}) limits its performance at low temperatures.[44,47] In comparison to cathodes, anodes are even more detrimentally affected by low operating temperatures. A study by Huang et al. showed that sluggish Li^+ diffusion within carbon anode significantly reduces their performance at −30°C.[48] Slow ion diffusion through the anode can lead to the accumulation of inactive ions on the electrode surface, resulting in dendrite growth, which increase the risk of short circuits and severe safety hazards.[45] Dendrite growth is a major concern for both LIBs and lithium metal batteries (LMBs), especially at low

temperatures.[44,49,50] Graphite is the most commonly used anode for LIBs. While pristine graphite offers favorable capacity (372 mAh g^{-1}) and long cycle life, its poor Li^+ diffusion kinetics and operating potential (~0.1 V vs Li/Li^+), close to that of Li metal (0 V vs Li/Li^+), hinders its performance at low temperatures due to the increased likelihood of Li plating on its surface.[48,51,52]

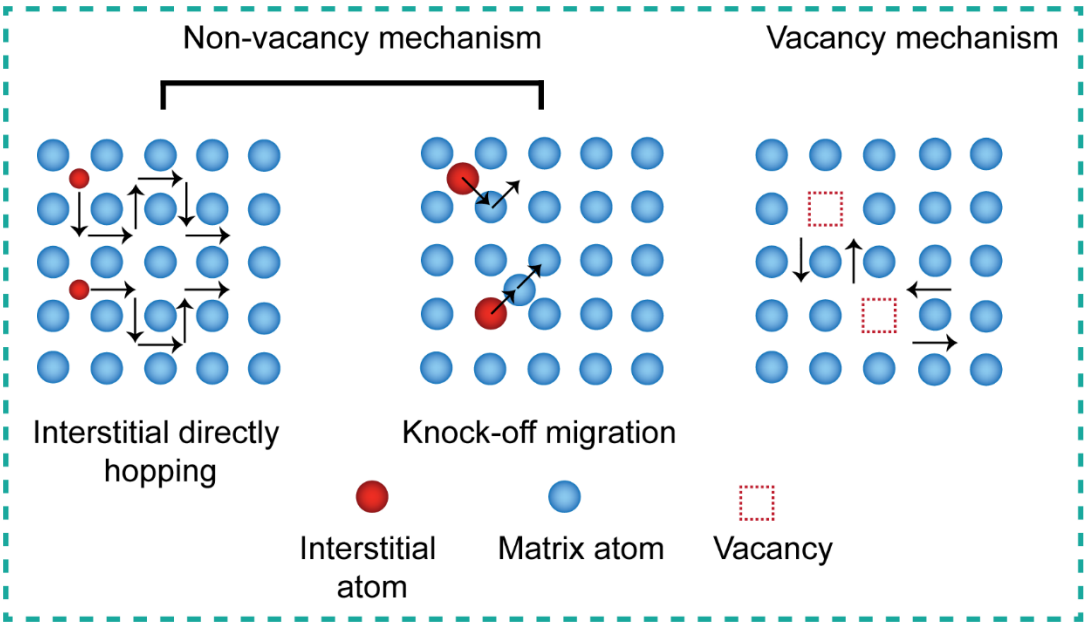


Figure 1.4. Schematic illustration of ion diffusion mechanisms with and without a vacancy involved. In EES devices such as supercapacitors and LIBs, ion diffusion within the electrode primarily occurs via interstitial diffusion, where ions such as Li^+ move through the electrode's crystal structure. Reproduced from (30). Copyright 2025, American Chemical Society.

1.4.1.3 Unfavorable Electronic and Ionic Properties of the Electrode

1.4.1.3.1 Electrode Microstructure

The structure of the electrode, such as porosity, the size and spatial distribution of pores, and tortuosity, greatly influences the performance of the EES device at low temperatures. As mentioned earlier, SC stores charges on or near the electrode surface. Porous materials allow ions to penetrate deeper into the electrode, increasing the accessible surface area and promoting more surface reactions. However, many electrodes have low porosity and narrow channels, which restrict ion diffusion. EDLC store charges through non-Faradaic processes, where ions adsorb at the interface between the electrode and the electrolyte when an external voltage is applied.[53] This process is highly dependent on the ion-accessible surface area of the electrode.[54]

Carbon-based electrodes are the most commonly used EDLC and often feature a range of pore sizes: macropores (>50 nm), carbon mesopores (2–50 nm), and micropores (<2 nm). [53] The pore size greatly impacts the charge storage mechanism in the EDLCs. Since macropores and mesopores are generally larger than solvated ions (∼1 nm), both anions and cations can enter the pore walls, forming densely packed ions that affect ion-transport and eventually slow ionic diffusion due to strong cation–anion interaction (**Figure1.5a**).[53,55–57] Jäckel et al. stated that excessively large pores limit specific surface area and thus reduce energy storage capacity (**Figure 1.5b**).[58] On the other hand, pores that are too small restrict ion accessibility, also leading to low capacity. Using DFT models, Jäckel et al. calculated the electrochemically active surface of different carbon materials, showing that pores smaller than the ion size of BF_4^- (0.45 nm) and TEA^+ (0.67 nm) are inaccessible (**Figure 1.5c**)

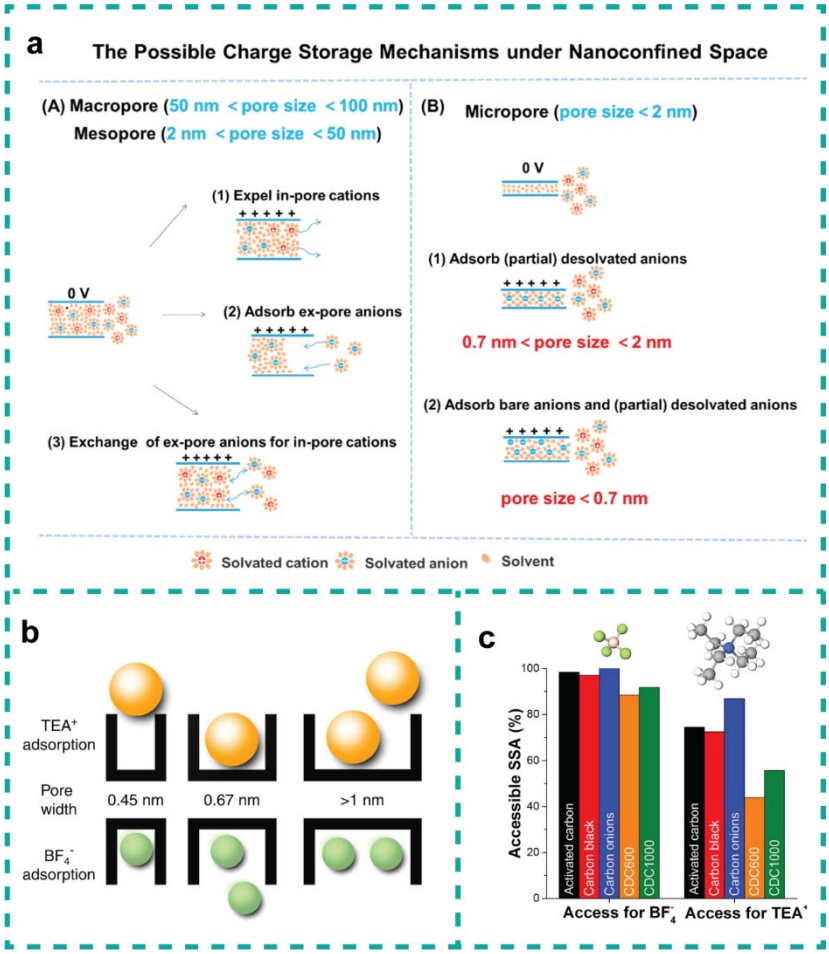


Figure 1.5. Ionic mobility is based on the pore size of the electrode. (a) Various possible charging mechanisms when the electrode is charged to a positive voltage. Reproduced from ref (52) (b) Absorption of cation (TEA^+) and anion (BF_4^-) in pores of different sizes. (c) Pore size distribution and porosity analysis of different carbon materials. Reproduced from ref (58). Copyright 2016, American Chemical Society.

Adding another layer of complexity to the narrative, the particle size and crystal structure of the electrode also impact EES performance. The particle size of the electrode's active material determines the diffusion path length for both ionic and

electronic transport.[49,59] Larger particles increase the diffusion path length and reduce the electrode–electrolyte surface contact, which limits performance, especially at low temperatures.[60] However, simply reducing particle size does not always solve the issue. Smaller particles often require more binders and can increase the likelihood of side reactions, both of which are detrimental at low temperatures.[61,62]

The crystal structure of the active material also affects the ion diffusion paths. During charging–discharging, structural changes occur in the cathode and anode, which impact the overall battery stability. Ion diffusion paths in crystal structures are classified into four types: nonframework (e.g., CuF_2 and FeF_2), one-dimensional (e.g., $LiFePO_4$, $Li_3V_2(PO_4)_3$, and $LiVPO_4F$), two-dimensional (e.g., $LiCoO_2$, graphite, and V_2O_5), and three-dimensional (e.g., $LiMn_2O_4$, and $Li_4Ti_5O_{12}$).[63,64] Each classification influences the ion diffusion differently.

1.4.1.3.2 Electrode Material Composition

The electronic conductivity of the electrode is crucial to the electrochemical performance of EES devices. While many EES electrode active materials have high theoretical capacity and capacitance, their poor electrical conductivity limits their effectiveness, particularly at low operating temperatures. One strategy to improve conductivity is elemental doping, which stabilizes the crystal structure of the active material during charge/discharge cycles and facilitates faster ion intercalation/deintercalation.[65] While doping methods have been shown to improve the performance of various electrode materials at room temperature, its effectiveness may

be limited at low temperatures. For example, Zhao et al. attempted to enhance the electrical conductivity of pristine $LiFePO_4$ via doping.[66] However, in the $LiFePO_4$/C cathode, impurities introduced through doping hinder diffusion of the ions in the solid state and cause lattice distortion, decreasing the diffusion coefficient at low temperatures.

The stability and capacity losses of EES devices are also influenced by the properties of the binders used. Binders are nonactive materials that bond the active materials, other additives, and the current collector together.[62,67] Poly(vinylidene fluoride) (PVDF) is the most used binder in LIBs due to its excellent electrochemical stability and strong adhesion.[67] However, PVDF is expensive, poses safe disposal concerns, requires the use of flammable solvents in its synthesis, and, most importantly, has been found to hinder Li^+ diffusion. Various materials have been explored in the past decade as an alternative to PVDF. For example, Mancini et al. compared the performance of an LIB prepared with water-soluble sodium carboxymethyl cellulose (CMC) and PVDF as binders.[67] At 30 °C, the CMC-based anode achieved a discharge capacity higher than that of the PVDF-based anode. The higher capacity is due to the more uniform electrode surface achieved with CMC, which improves the electrode/electrolyte interface morphology and enhances interface kinetics.[67] However, this comparison was performed at room temperature. At low temperature, most polymers become stiff, which is detrimental to the device's cycling performance.[62] Eom et al. found that even though the anode with a CMC-based binder performed better at room temperature, the anode with a PVDF-based binder still

exhibited better cycling performance at low temperature due to its lower glass transition temperature property.[68]

1.5 Mechanically Robust Electrochemical Energy Storage Electrodes

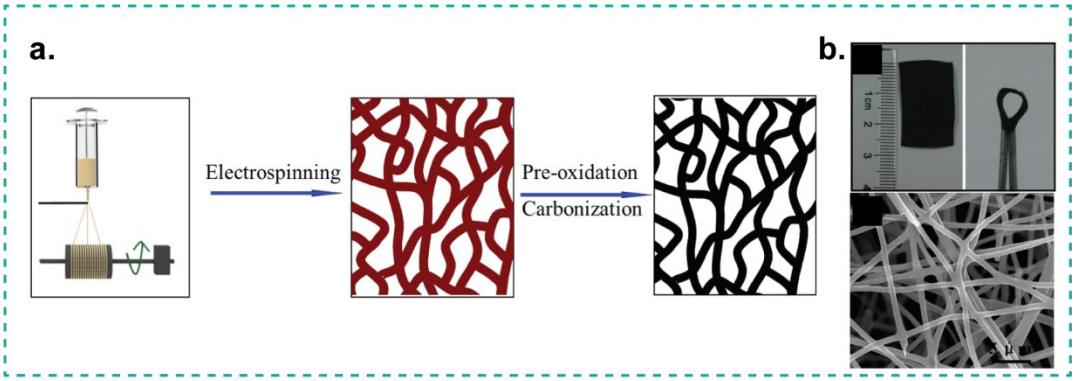


Figure 1.6. (a). Schematic diagram of the preparation of cross-linked carbon nanofibers. (b). Digital images of the cross-linked carbon nanofiber before and under folding condition (top) and SEM image of it (bottom). Reproduced from ref(69). Copyright 2015, Elsevier.

Similar to the temperature, the mechanical properties of the electrodes also play an important role in their performance and the applications. Flexible, bendable, and compressible energy storage devices received considerable attention due to the increase in the demand for the research and development of "new generation" technologies such as wearable devices, bendable phones, roll-up displays, and medical devices.[70–72] Currently, energy storage devices are usually rigid and bulky which can't support the requirements for these "next generation" technologies.[70] Among the two main component of energy storage devices, electrodes serves as the limiting factor on

developing of these “next generation” technologies. Therefore, development of thin, flexible, and lightweight electrodes with high electrical conductivity and excellent mechanical robustness is urgent and highly desirable. Carbonaceous materials are widely used electrode material either as a scaffold or the active material.[73,74] Carbon nanotubes, graphene, graphite, carbon fiber, and MXenes are the common carbon-based material used to achieve a mechanically robust, lightweight, and highly conductive electrode.[70,75–77] Cheng et al. fabricated a solid state supercapacitor using a flexible nitrogen doped carbon nanofiber via electrospinning and carbonization process (**Figure 1.6a**).[69] The combination of carbon fiber cross linking and heteroatom doping increase the conductivity and added pseudocapacitance which increase the capacitance of the carbon. This device showed no capacitance loss even when the device was bent to 180° (**Figure 1.6b)**. Over the past decade, multiple fabrication and synthesis methods were done to develop novel flexible electrodes.[10,78] Printing, slurry coating, and vacuum filtration are some of the process on fabricating thin, flexible electrodes.[78] One of the novel way to fabricate a thin, flexible electrode was done by El-Kady et al. El-Kady et al. developed a flexible graphene-based supercapacitors by directly reduce graphite oxide film using an infrared laser producing laser-scribed graphene.[79] Using a polymer based electrolyte, they fabricated a flexible device that shows no effect on the capacitive behavior after tested under different bending conditions.

1.6 References

1. Smart, M. C. *et al.* The use of lithium-ion batteries for JPL's Mars missions. *Electrochimica Acta* **268**, 27–40 (2018).
2. Viola, W. & Andrew, T. L. An Aqueous Eutectic Electrolyte for Low-Cost, Safe Energy Storage with an Operational Temperature Range of 150 °C, from −70 to 80 °C. *J. Phys. Chem. C* **125**, 246–251 (2021).
3. Yao, B. *et al.* Printing Porous Carbon Aerogels for Low Temperature Supercapacitors. *Nano Lett.* **21**, 3731–3737 (2021).
4. Brandon, E. J., West, W. C., Smart, M. C., Whitcanack, L. D. & Plett, G. A. Extending the low temperature operational limit of double-layer capacitors. *Journal of Power Sources* **170**, 225–232 (2007).
5. Xu, J. *et al.* Extending the low temperature operational limit of Li-ion battery to −80 °C. *Energy Storage Materials* **23**, 383–389 (2019).
6. Wang, C.-Y. *et al.* Lithium-ion battery structure that self-heats at low temperatures. *Nature* **529**, 515–518 (2016).
7. Ji, Y. & Wang, C. Y. Heating strategies for Li-ion batteries operated from subzero temperatures. *Electrochimica Acta* **107**, 664–674 (2013).
8. Gupta, A. & Manthiram, A. Designing Advanced Lithium-Based Batteries for Low-Temperature Conditions. *Advanced Energy Materials* **10**, 2001972 (2020).
9. Li, Q. *et al.* Low-Temperature Electrolyte Design for Lithium-Ion Batteries: Prospect and Challenges. *Chemistry – A European Journal* **27**, 15842–15865 (2021).

10. Wang, Y., Yang, Q., Zhao, Y., Du, S. & Zhi, C. Recent Advances in Electrode Fabrication for Flexible Energy-Storage Devices. *Advanced Materials Technologies* **4**, 1900083 (2019).
11. Kim, B. C., Hong, J.-Y., Wallace, G. G. & Park, H. S. Recent Progress in Flexible Electrochemical Capacitors: Electrode Materials, Device Configuration, and Functions. *Advanced Energy Materials* **5**, 1500959 (2015).
12. Li, W. *et al.* Damage of prismatic lithium-ion cells subject to bending: Test, model, and detection. *EcoMat* **4**, e12257 (2022).
13. Bower, A. F., Guduru, P. R. & Sethuraman, V. A. A finite strain model of stress, diffusion, plastic flow, and electrochemical reactions in a lithium-ion half-cell. *Journal of the Mechanics and Physics of Solids* **59**, 804–828 (2011).
14. Song, Y. C., Li, Z. Z., Soh, A. K. & Zhang, J. Q. Diffusion of lithium ions and diffusion-induced stresses in a phase separating electrode under galvanostatic and potentiostatic operations: Phase field simulations. *Mechanics of Materials* **91**, 363–371 (2015).
15. Shi, Y. *et al.* The effect of bending deformation on flexible electrodes during charging and discharging. *Mechanics of Materials* **161**, 104024 (2021).
16. Zuo, W. *et al.* Battery-Supercapacitor Hybrid Devices: Recent Progress and Future Prospects. *Advanced Science* **4**, 1600539 (2017).
17. Simon, P. & Gogotsi, Y. Materials for electrochemical capacitors. *Nature Mater* **7**, 845–854 (2008).

18. Ko, J. S. *et al.* Differentiating Double-Layer, Pseudocapacitance, and Battery-like Mechanisms by Analyzing Impedance Measurements in Three Dimensions. *ACS Appl. Mater. Interfaces* **12**, 20145–20145 (2020).
19. Dutta, A., Mitra, S., Basak, M. & Banerjee, T. A comprehensive review on batteries and supercapacitors: Development and challenges since their inception. *Energy Storage* **5**, e339 (2023).
20. Feng, Y. *et al.* Challenges and advances in wide-temperature rechargeable lithium batteries. *Energy & Environmental Science* **15**, 1711–1759 (2022).
21. Li, Q. *et al.* Li+-Desolvation Dictating Lithium-Ion Battery's Low-Temperature Performances. *ACS Appl. Mater. Interfaces* **9**, 42761–42768 (2017).
22. Guan, L., Yu, L. & Chen, G. Z. Capacitive and non-capacitive faradaic charge storage. *Electrochimica Acta* **206**, 464–478 (2016).
23. Choi, C. *et al.* Achieving high energy density and high power density with pseudocapacitive materials. *Nat Rev Mater* **5**, 5–19 (2020).
24. Liu, T. & Li, Y. Addressing the Achilles' heel of pseudocapacitive materials: Long-term stability. *InfoMat* **2**, 807–842 (2020).
25. Augustyn, V., Simon, P. & Dunn, B. Pseudocapacitive oxide materials for high-rate electrochemical energy storage. *Energy Environ. Sci.* **7**, 1597–1614 (2014).
26. Chodankar, N. R. *et al.* Supercapacitors operated at extremely low environmental temperatures. *J. Mater. Chem. A* **9**, 26603–26627 (2021).
27. Lee, H. Y. & Goodenough, J. B. Supercapacitor Behavior with KCl Electrolyte. *Journal of Solid State Chemistry* **144**, 220–223 (1999).

28. Jabeen, N. *et al.* Enhanced Pseudocapacitive Performance of α-MnO2 by Cation Preinsertion. *ACS Appl. Mater. Interfaces* **8**, 33732–33740 (2016).
29. Xue, X. & Li, Y. Advancing Mn2+/MnO2 Conversion Chemistry through Redox Mediation: Mechanistic Insights and Outlook. *ACS Energy Lett.* 3275–3286 (2025) doi:10.1021/acsenergylett.5c01329.
30. Pinongcos, A. B., Xue, X., Chandrasekaran, S., Worsley, M. A. & Li, Y. Innovative Electrode Design for Low-Temperature Electrochemical Energy Storage: A Mini Review. *Energy Fuels* **39**, 6078–6096 (2025).
31. Li, Z. *et al.* 40 Years of Low-Temperature Electrolytes for Rechargeable Lithium Batteries. *Angewandte Chemie International Edition* **62**, e202303888 (2023).
32. Xu, J. *et al.* Temperature-independent capacitance of carbon-based supercapacitor from −100 to 60 °C. *Energy Storage Materials* **22**, 323–329 (2019).
33. Xu, K., von Cresce, A. & Lee, U. Differentiating Contributions to "Ion Transfer" Barrier from Interphasial Resistance and Li+ Desolvation at Electrolyte/Graphite Interface. *Langmuir* **26**, 11538–11543 (2010).
34. Yan, K. *et al.* Temperature-Dependent Nucleation and Growth of Dendrite-Free Lithium Metal Anodes. *Angewandte Chemie* **131**, 11486–11490 (2019).
35. Thenuwara, A. C., Shetty, P. P. & McDowell, M. T. Distinct Nanoscale Interphases and Morphology of Lithium Metal Electrodes Operating at Low Temperatures. *Nano Lett.* **19**, 8664–8672 (2019).
36. Weng, S. *et al.* Temperature-dependent interphase formation and Li+ transport in lithium metal batteries. *Nat Commun* **14**, 4474 (2023).

37. Lin, Y.-X. *et al.* Connecting the irreversible capacity loss in Li-ion batteries with the electronic insulating properties of solid electrolyte interphase (SEI) components. *Journal of Power Sources* **309**, 221–230 (2016).

38. Yuan, S. *et al.* Revisiting the designing criteria of advanced solid electrolyte interphase on lithium metal anode under practical condition. *Nano Energy* **83**, 105847 (2021).

39. Lin, D., Liu, Y. & Cui, Y. Reviving the lithium metal anode for high-energy batteries. *Nature Nanotech* **12**, 194–206 (2017).

40. Shao, T. *et al.* Recent Research on Strategies to Improve Ion Conduction in Alkali Metal-Ion Batteries. *Batteries & Supercaps* **2**, 403–427 (2019).

41. Wu, M., Xu, B. & Ouyang, C. Physics of electron and lithium-ion transport in electrode materials for Li-ion batteries*. *Chinese Phys. B* **25**, 018206 (2015).

42. Park, M., Zhang, X., Chung, M., Less, G. B. & Sastry, A. M. A review of conduction phenomena in Li-ion batteries. *Journal of Power Sources* **195**, 7904–7929 (2010).

43. Zhang, B. *et al.* Mechanisms and properties of ion-transport in inorganic solid electrolytes. *Energy Storage Materials* **10**, 139–159 (2018).

44. Zhang, N. *et al.* Critical Review on Low-Temperature Li-Ion/Metal Batteries. *Advanced Materials* **34**, 2107899 (2022).

45. Zhang, D. *et al.* Constructing advanced electrode materials for low-temperature lithium-ion batteries: A review. *Energy Reports* **8**, 4525–4534 (2022).

46. Morley, J. D., George, C., Hadler, K. & Brito-Parada, P. R. Crystallography of Active Particles Defining Battery Electrochemistry. *Advanced Energy Materials* **14**, 2302893 (2024).

47. Prosini, P. P., Lisi, M., Zane, D. & Pasquali, M. Determination of the chemical diffusion coefficient of lithium in LiFePO4. *Solid State Ionics* **148**, 45–51 (2002).

48. Huang, C.-K., Sakamoto, J. S., Wolfenstine, J. & Surampudi, S. The Limits of Low-Temperature Performance of Li-Ion Cells. *J. Electrochem. Soc.* **147**, 2893 (2000).

49. Luo, H. *et al.* Lithium-Ion Batteries under Low-Temperature Environment: Challenges and Prospects. *Materials (Basel)* **15**, 8166 (2022).

50. Lyu, T. *et al.* Carbon/Lithium Composite Anode for Advanced Lithium Metal Batteries: Design, Progress, In Situ Characterization, and Perspectives. *Advanced Energy Materials* **12**, 2201493 (2022).

51. Cai, W. *et al.* A review on energy chemistry of fast-charging anodes. *Chem. Soc. Rev.* **49**, 3806–3833 (2020).

52. Pender, J. P. *et al.* Electrode Degradation in Lithium-Ion Batteries. *ACS Nano* **14**, 1243–1295 (2020).

53. Tan, J., Li, Z., Ye, M. & Shen, J. Nanoconfined Space: Revisiting the Charge Storage Mechanism of Electric Double Layer Capacitors. *ACS Appl. Mater. Interfaces* **14**, 37259–37269 (2022).

54. Celine Largeot, † *et al.* Relation between the Ion Size and Pore Size for an Electric Double-Layer Capacitor. *ACS Publications* https://pubs.acs.org/doi/full/10.1021/ja7106178 (2008) doi:10.1021/ja7106178.

55. Forse, A. C., Merlet, C., Griffin, J. M. & Grey, C. P. New Perspectives on the Charging Mechanisms of Supercapacitors. *J. Am. Chem. Soc.* **138**, 5731–5744 (2016).

56. Hu, A. *et al.* Ion Transport Kinetics in Low-Temperature Lithium Metal Batteries. *Advanced Energy Materials* **12**, 2202432 (2022).

57. Sun, Y., Liu, B., Liu, L. & Yan, X. Ions Transport in Electrochemical Energy Storage Devices at Low Temperatures. *Advanced Functional Materials* **32**, 2109568 (2022).

58. Jäckel, N., Simon, P., Gogotsi, Y. & Presser, V. Increase in Capacitance by Subnanometer Pores in Carbon. *ACS Energy Lett.* **1**, 1262–1265 (2016).

59. Brezesinski, T., Wang, J., Polleux, J., Dunn, B. & Tolbert, S. H. Templated Nanocrystal-Based Porous TiO2 Films for Next-Generation Electrochemical Capacitors. *J. Am. Chem. Soc.* **131**, 1802–1809 (2009).

60. Kondrat, S., Pérez, C. R., Presser, V., Gogotsi, Y. & Kornyshev, A. A. Effect of pore size and its dispersity on the energy storage in nanoporous supercapacitors. *Energy Environ. Sci.* **5**, 6474–6479 (2012).

61. Pohjalainen, E., Rauhala, T., Valkeapää, M., Kallioinen, J. & Kallio, T. Effect of Li4Ti5O12 Particle Size on the Performance of Lithium Ion Battery Electrodes at High C-Rates and Low Temperatures. *J. Phys. Chem. C* **119**, 2277–2283 (2015).

62. Guo, R. & Han, W. The effects of electrolytes, electrolyte/electrode interphase, and binders on lithium-ion batteries at low temperature. *Materials Today Sustainability* **19**, 100187 (2022).
63. Lee, W. *et al.* Advances in the Cathode Materials for Lithium Rechargeable Batteries. *Angewandte Chemie International Edition* **59**, 2578–2605 (2020).
64. Wang, R. *et al.* "Fast-Charging" Anode Materials for Lithium-Ion Batteries from Perspective of Ion Diffusion in Crystal Structure. *ACS Nano* **18**, 2611–2648 (2024).
65. Shi, Q. *et al.* Niobium-doped layered cathode material for high-power and low-temperature sodium-ion batteries. *Nat Commun* **13**, 3205 (2022).
66. Zhao, N., Li, Y., Zhao, X., Zhi, X. & Liang, G. Effect of particle size and purity on the low temperature electrochemical performance of LiFePO4/C cathode material. *Journal of Alloys and Compounds* **683**, 123–132 (2016).
67. Mancini, M., Nobili, F., Tossici, R., Wohlfahrt-Mehrens, M. & Marassi, R. High performance, environmentally friendly and low cost anodes for lithium-ion battery based on TiO2 anatase and water soluble binder carboxymethyl cellulose. *Journal of Power Sources* **196**, 9665–9671 (2011).
68. Eom, J.-Y. & Cao, L. Effect of anode binders on low-temperature performance of automotive lithium-ion batteries. *Journal of Power Sources* **441**, 227178 (2019).
69. Cheng, Y. *et al.* Flexible and cross-linked N-doped carbon nanofiber network for high performance freestanding supercapacitor electrode. *Nano Energy* **15**, 66–74 (2015).

70. Wang, X. *et al.* Flexible Energy-Storage Devices: Design Consideration and Recent Progress. *Advanced Materials* **26**, 4763–4782 (2014).

71. Mao, L., Meng, Q., Ahmad, A. & Wei, Z. Mechanical Analyses and Structural Design Requirements for Flexible Energy Storage Devices. *Advanced Energy Materials* **7**, 1700535 (2017).

72. Sumboja, A. *et al.* Electrochemical energy storage devices for wearable technology: a rationale for materials selection and cell design. (2018) doi:10.1039/C8CS00237A.

73. Yao, B. *et al.* 3D-Printed Structure Boosts the Kinetics and Intrinsic Capacitance of Pseudocapacitive Graphene Aerogels. *Advanced Materials* **32**, 1906652 (2020).

74. Yao, B. *et al.* Efficient 3D Printed Pseudocapacitive Electrodes with Ultrahigh MnO2 Loading. *Joule* **3**, 459–470 (2019).

75. Guo, S. *et al.* MXene-based all-solid flexible electrochromic microsupercapacitor. *Microsyst Nanoeng* **10**, 89 (2024).

76. Zhu, S., Sheng, J., Chen, Y., Ni, J. & Li, Y. Carbon nanotubes for flexible batteries: recent progress and future perspective. *National Science Review* **8**, nwaa261 (2021).

77. Hong, J.-Y., Bak, B. M., Wie, J. J., Kong, J. & Park, H. S. Reversibly Compressible, Highly Elastic, and Durable Graphene Aerogels for Energy Storage Devices under Limiting Conditions. *Advanced Functional Materials* **25**, 1053–1062 (2015).

78. Yao, B. *et al.* Paper-Based Electrodes for Flexible Energy Storage Devices. *Advanced Science* **4**, 1700107 (2017).

79. El-Kady, M. F., Strong, V., Dubin, S. & Kaner, R. B. Laser Scribing of High-Performance and Flexible Graphene-Based Electrochemical Capacitors. *Science* **335**, 1326–1330 (2012).

Chapter 2

Nitrogen-Enriched Carbon Electrode with High Capacitance Retention for Low-Temperature Energy Storage

2.1 Abstract

A reliable, high-performance, lightweight, and safe energy storage device such as supercapacitors are necessary for prolonged deep space exploration. Supercapacitors received considerable attention due to their safety, high power density, fast charging capability, and electrochemical stability. However, most supercapacitors' performance rapidly decreases at low temperatures due to sluggish ion diffusion. The combined merits of multiscale porous carbon aerogel (MCA) and nitrogen dopant allow faster diffusion of ions and thus achieve high capacitance retention at low operating temperature. Here, we introduce N-dopant on a highly porous carbon electrode via high temperature post-treatment in NH_3/N_2 gas mixture. At low temperature, N-doped MCA (N-MCA-1000) achieved a high capacitance retention of 9%. This impressive result highlights the essential role of balancing the porosity and nitrogen content for retaining the capacitance at low operating temperatures.

2.2 Introduction

Demand for electrochemical energy storage (EES) devices that could withstand extreme environments is rapidly rising over the past few years.[1–7] Performance degradation at low operating temperature is the significant limitation of most EES devices which are essential for space and polar region explorations.[8] Supercapacitors deliver higher power density and could withstand low operating temperatures better compared to batteries.[1] However, these devices still suffer from low energy density. Numerous efforts on electrolyte over the past decade have been conducted to enhance the low temperature properties of EES devices.[1,3,5,9–11] Meanwhile, the electrode also plays an important role on the development of low temperature supercapacitors.

Carbon based materials are one of the leading active electrode materials for supercapacitors due to their low cost, high conductivity property, and tunable porosity.[5] As the operating temperature decrease, the diffusion rate of the ion severely hinders the over performance of the supercapacitors.[6] Structural engineering have demonstrated to enhanced the diffusion of the ion.[6,12–16] Multiscale porous carbon aerogels (MCA) has been demonstrated as an excellent candidate to enhance the performance of low temperature supercapacitors.[13] Yao et al. demonstrated that combining chemical modification with 3D printing to optimize carbon-based electrode architecture significantly promoted ion diffusion, and thus enhanced device performance under low-temperature operating conditions.[13] However, increasing the surface area of the electrode is not sufficient to retain its room temperature performance at ultra-low operating temperatures. Various works have shown that introducing surface functional

groups can effectively enhance the electrochemical performance of electrode material.[2,14,16,17] For example, Liu et al. tunned electrochemical properties of a carbon based electrode by modifying the pyrolysis protocol which doped the carbon with nitrogen functional groups.[17] Yao et al. increased the surface area via 3D printing and introduced surface functional groups on a carbon based electrode to boosted capacitance of the supercapacitor.[16] Overall, these works showed an outstanding electrochemical performance at ambient temperatures. However, little work has been done on enhancing the low temperature performance of supercapacitors via surface functionalization.

Herein we design a nitrogen enriched multiscale porous carbon aerogel (N-MCA) for low temperature supercapacitor using a highly abundant, cheap crystal nanocellulose (CNC) as the carbon source (**Figure 2.1**). Symmetric device was fabricated and achieved a high capacitance retention at low operating temperature of -40°C. Surface functionalization via high temperature mixed ammonia/ nitrogen (NH_3/N_2) atmosphere treatment introduced nitrogen functional groups that improved the electronic structure of the electrode and increased the adsorption energies between the electrolyte and the surface of the electrode, thereby enhanced the overall performance and achieved a high retention rate at -40°C.

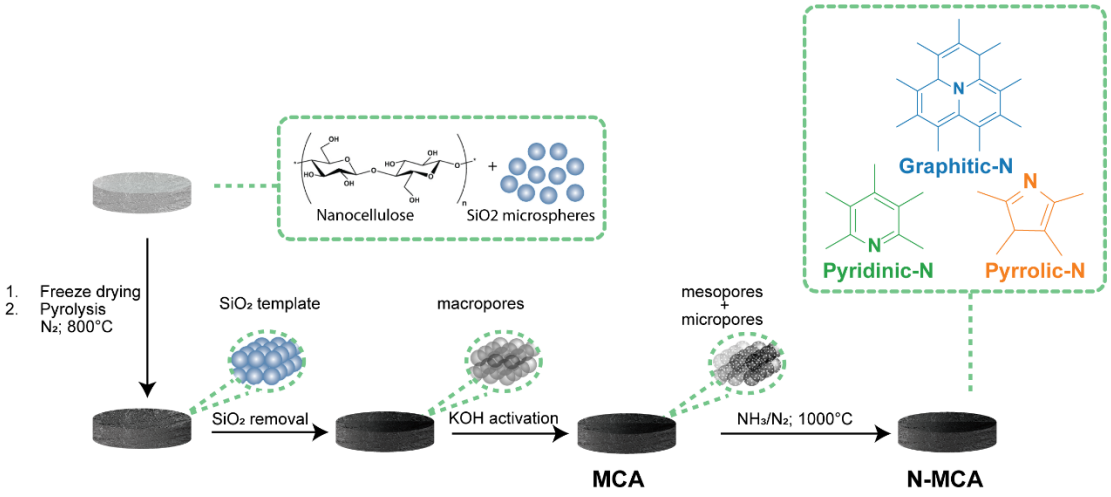


Figure 2.1. Schematic illustration of fabricating N-MCA electrodes.

2.3 Experimental

2.3.1 Preparation of Nitrogen-doped multiscale porous carbon aerogel electrode

Following a protocol published previously, SiO_2 nanospheres were synthesized via modified Stöber method. A gram of SiO_2 nanospheres were sonicated in 2mL of Milli-Q water for 24 h in ice water. The dispersed SiO_2 was then mixed with 1g CNC powder and 2mL Milli-Q water in a planetary Thinky mixer at 2000 rpm.

The viscous ink was molded with silicon-based molder and froze in dry ice for 30 min before freeze-dried for 48 h in vacuum. The cellulose-SiO_2 aerogel were carbonized in a tube furnace at 800°C for 2 h under N_2 (40 standard cubic centimeter per minute (sccm)) with a ramping rate of 5°C/min. Then the samples were soaked in 4M NaOH solution at 80°C for 2 days to dissolve the SiO_2 and create macropores. This was followed by soaking the samples in water at 80°C overnight to remove any residual NaOH and silicate salts. The samples were then dry at 80°C for 2 h before immersing

1M KOH solution for 8h. After that, the samples were dried in an electric oven at 80 °C for at least 2h and then annealed in a tube furnace at 800°C for 1 h under N_2 (40 standard cubic centimeter per minute (sccm)) with a ramping rate of 5°C/min. Once cooled down at room temperature, the samples were immediately washed with a 0.5M HCl aqueous solution, rinsed with water until the pH reached 7, and then dried in an electric oven at 80 °C overnight. To dope the electrode, ammonia treatment was conducted. The samples were again annealed at 800 °C for 10 min under NH_3/N_2 mixture (NH_3 flow rate, 10 sccm; N_2 flow rate, 50 sccm) with the ramping rate of 5°C and then continue at the same temperature for 110 min under N_2. Afterwards, the tube furnace cooled down naturally at room temperature. For comparison, the undoped electrodes, denoted as MCA, were prepared identical steps except without the ammonia treatment at the end. The preparation method is schematically shown in **Figure 2.1.**

2.3.2 Material Characterization

The structural and surface properties of the electrodes were analyzed with scanning electron microscopy (SEM) and energy-dispersive spectroscopy (EDS) using Thermo Scientific Scios 2 DualBeam, equipped with an Oxford Instruments AZtecLive Ultim Max 100 EDS detector. The chemical composition of the functional groups was investigated by X-ray photoelectron spectroscopy (XPS, Nexus X-ray Photoelectron Spectrometer) using monochromatic Al Kα X-ray (1486.6 eV) with 400 μm spot size. Nitrogen porosimetry was carried out using an Autosorb iQ. The sample was degassed for 10 hours at 110 °C under vacuum. Surface area and pore distribution were

determined by Brunauer-Emmett-Teller (BET) and Barrett-Joyner-Halenda (BJH) methods.

2.3.3 Electrochemical Characterization

The electrochemical performance of electrode materials was measured in a three-electrode configuration using electrochemical stations (BioLogic EC-Lab SP-300 and VMP-3e) inside the glovebox filled with Ar gas. The doped and undoped MCA with geometric area of 0.79 cm^2 were used as working electrode. Pt/Pt^+ and carbon paper were used as reference electrode and counter electrode, respectively. Symmetric devices were fabricated in a coin cell by assembling two pieces of identical carbon aerogel, sandwiching a 16 mm diameter glass microfiber filter (Whatman 1820-125 GF/A, 1.6μm). Each electrode was compressed between two Ni-foam to improve the contact of the electrodes with the current collectors. The electrolyte used for all measurements is a mixed solution containing 0.5 M tetraethylammonium tetrafluoroborate ($TEABF_4$) in 1:1 acetonitrile (AN)/ methyl formate (MF).

2.3.4 Calculations

The gravimetric capacitance ($C_{G,}$ F g^{-1}) of single electrodes was calculated based on the galvanostatic charging and discharging (GCD) curves using Eq. 1:

$$C_G = \frac{I \times t}{\Delta U \times m} \qquad \text{(Eq. 2.1)}$$

where I *is* the current (mA), t is the discharge time (s), ΔU is the potential window excluding the iR drop, and m is the mass (mg).

The volumetric capacitance (C_V, mF cm^{-3}) of the symmetric device calculated based on the GCD curves using Eq. 2:

$$C_V = \frac{I \times t}{\Delta U \times V} \quad \text{(Eq. 2.2)}$$

where *I is* the current (mA), *t* is the discharge time (s), *ΔU* is the potential window excluding the *iR* drop, *V* is the volume of the two electrodes (cm^3).

The volumetric energy density (E, Wh L^{-1}) and power density (P, W L^{-1}) of the symmetric supercapacitor device are calculated using the following equations:

$$E_V = \frac{C_V \Delta U^2}{2 \times 3600} \quad \text{(Eq.2.3)}$$

$$P_V = \frac{E_V \times 3600}{t} \quad \text{(Eq. 2.4)}$$

where C_V is the volumetric capacitance (mF cm^{-3}), *ΔU* is the potential window excluding the *iR* drop, and *t* is the discharge time (s) obtained from the GCD curve.

Kinetic Analysis: The difference in charge storage kinetics was determined by relating the current to the sweep rate (ν) extracted from the cyclic voltammetry curve. The *b* value from Eq. provides information on the charge storage kinetics. The *b* value can be obtained by plotting the logarithm of the absolute current density (*i*) versus the logarithm of sweep rate ($\log i = b \log \nu + k$). A *b* value of 1 indicates that electrochemical process is dominated by an ideal capacitive behavior, meanwhile a *b* value of 0.5 indicates the process is dominated by diffusion-controlled process. The *b* value can

vary between 0.5 to 1 depending on the potential. Trasatti method was utilized to quantify the capacitance contribution by the surface and bulk.[18] Areal capacitance (*C*) at different scan rates were evaluated from the cyclic voltammetry (CV) curves using Eq 5:

$$C = \frac{S_{CV}}{2v\,\Delta U} \qquad \text{(Eq.2.5)}$$

where S_{CV} is the area enclosed by the CV curve (mA V cm^{-2}), v is the scan rate (V s^{-1}), and ΔU is the working potential (V). By assuming a semi-finite ion diffusion, a linear dependence of C vs. $v^{-1/2}$ can be drawn at slow scan rates (1–5 mV s^{-1}). A linear fit was extrapolated at low scan rates and the determined the y-intercept ($v \rightarrow +\infty$) which represents the areal capacitance contributed by the surface ($C_{SURFACE}$). Since the total capacitance (C) at each scan rate was a sum of $C_{SURFACE}$ and C_{BULK}, the percentage of capacitance from surface and bulk can be calculated.

2.4 Results and Discussion

The fabrication of multiscale porous carbon aerogel (MCA) and nitrogen-doped multiscale carbon aerogel (N-MCA) were depicted in **Figure 2.1**. Crystal nanocellulose (nanocelluse) and silica microspheres were combined to create a homogeneous and highly viscous mixture suspension. The silica microspheres serve as hard temperate to create macropores. After carbonization of the freeze-dried monolith, the silicate microspheres template was removed and followed by KOH activation to achieve the multiscale pore structures of MCA. Nitrogen dopant was introduced via. high temperature ammonia treatment in a NH_3/N_2 mixed atmosphere (20 vol% NH_3) at 1000

°C for 10 min and then keeping the samples under N_2 atmosphere at the respective temperature until the total pyrolysis time was 160 min. The resultant electrode was denoted as N-MCA (N-MCA-1000). The rationale of annealing the MCA in the mixed gas atmosphere first was discussed in the previous report elsewhere.[17]

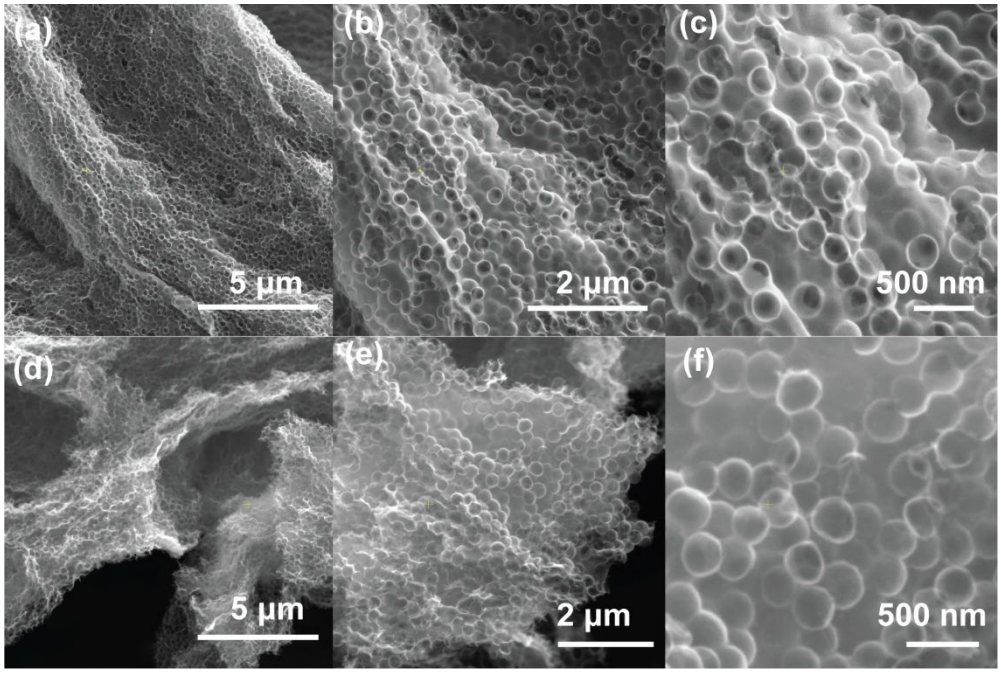


Figure 2.2. SEM images of (a-c) MCA and N-MCA (d-f).

Scanning electron microscopy (SEM) and Tuning electron microscopy (TEM) revealed the formation of the periodic pore channels in the MCA and N-MCA (**Figure 2.2**). Micron size pores (ca. 5-50 µm) were created by sublimation of ice during the freeze-drying process.[13] The creation of these pores helps with diffusion of electrolytes through the electrode. Interconnected carbon spheres are macropores (*ca.* 300 nm) obtained after the removal of silica templates.[13] These pores serve as electrolyte reservoirs which decrease the ion diffusion length. Mesopores and micropores (*ca*. 2-4

nm) were created via. KOH activation further increases the active surface area. Annealing at the high temperature in NH_3 /N_2 atmosphere alters the surface chemistry of carbon aerogels.[17]

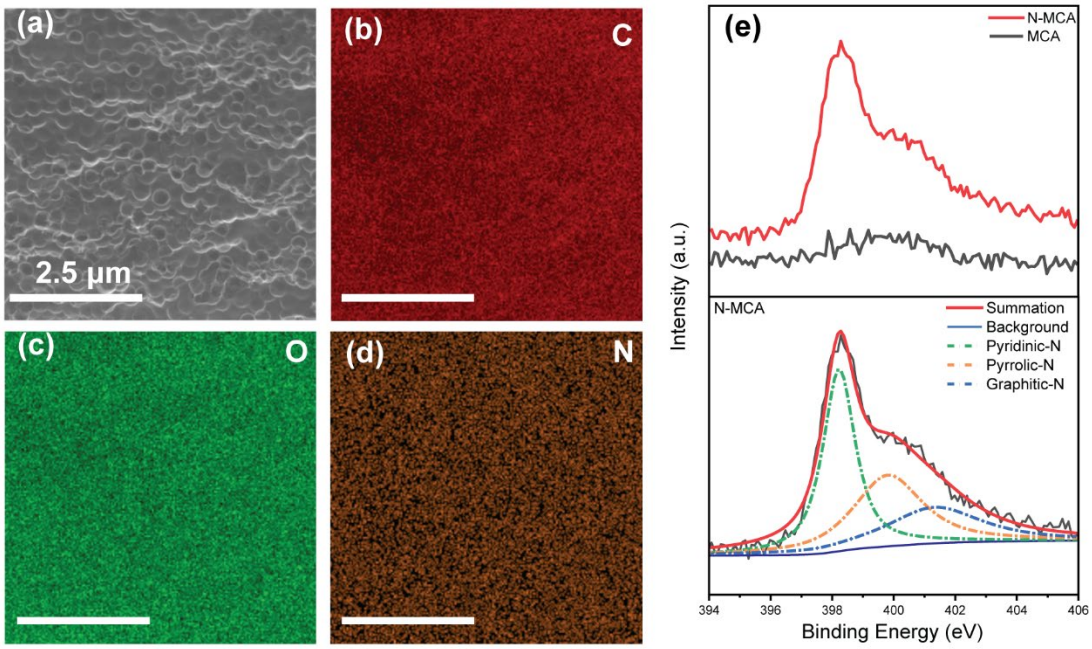


Figure 2.3. (a) SEM image of N-MCA and its corresponding energy dispersive spectroscopy (EDS) mapping images of (b) carbon, (c) oxygen, and (d) nitrogen. (e) Core N 1s XPS spectra of the MCA and N-MCA. The bottom part is the deconvoluted core N 1s XPS spectra of N-MCA. Dashed lines outline the deconvoluted peaks corresponding to pyridinic-N (green), pyrrolic-N (orange), and graphitic-N (blue).

Surface properties were analyzed using the energy dispersive X-ray spectroscopy (EDS) elemental which revealed that N-MCA is fully covered with nitrogen (**Figure 2.3a-d)**. The core N 1s X-ray photoelectron spectroscopy (XPS) spectra revealed the NH_3/N_2 post-treatment introduced nitrogen functional groups on

the MCA surface. The core N 1s XPS of N-MCA revealed that pyridinic-N (green), pyrrolic-N (orange), and graphitic-N (blue) were introduced into the MCA surface (**Figure 2.3e**).

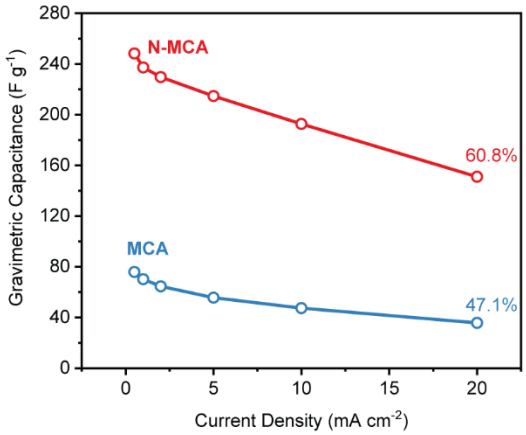


Figure 2.4. Gravimetric capacitance of N-MCA and MCA collected in 0.5M $TEABF_4$ in 1:1 acetonitrile and methyl formate electrolyte via three-electrode testing configuration with carbon paper and platinum wire as counter and reference electrodes, respectively.

Electrochemical performance MCA and N-MCA electrodes were evaluated in three-electrode configuration using 0.5M $TEABF_4$ in 1:1 AN/MF as the electrolyte, and carbon paper and platinum wire as counter and reference electrodes, respectively. Based on the gravimetric capacitance of the electrode, calculated from galvanostatic charge and discharge (GCD) curves, introduction of nitrogen functional groups on MCA through NH_3/N_2 post-treatment boost the performance of the MCA from 75.9 F g^{-1} to 248.3 F g^{-1} at 0.5 mA cm^{-2} (**Figure 2.4**). N-MCA achieved a capacitance retention

of 60% from 0.5 to 20 mA cm^{-2}. Meanwhile, MCA achieved 47% capacitance retention from 0.5 to 20 mA cm^{-2} current densities.

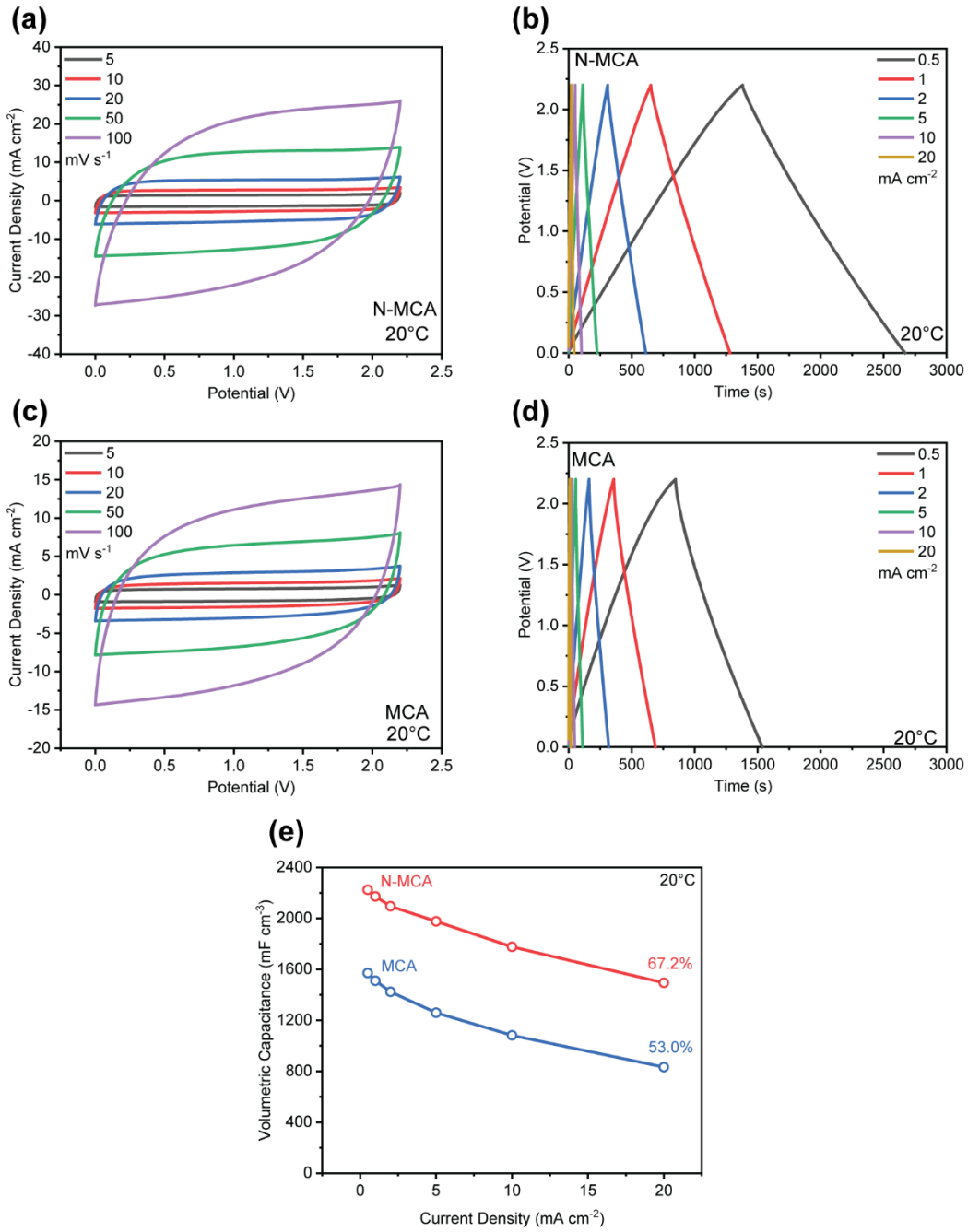


Figure 2.5. Cyclic voltammetry (CV) and galvanostatic charging and discharging (GCD) curves of (a,b) N-MCA and (c,d) MCA collected at 20°C, respectively. (e)Volumetric capacitance of symmetric device with N-MCA and MCA at current density of 0.5-20 mA cm^{-2}, collected at 20 °C.

To evaluate the performance of the N-MCA and MCA with respect to the operating temperature, symmetric supercapacitors were fabricated by assembling two identical electrodes. The MCA and N- MCA electrodes were compressed between two nickel-foam to reduce the contact resistance between the active material and the current collector and control the electrodes' area. For simplicity, the symmetric supercapacitor devices are denoted based on the type of electrodes used. Electrochemical performance of the two symmetric supercapacitors was first evaluated at 20 °C. The performance of N-MCA and MCA can be initially compared by their CV curves. N-MCA has a larger enclosed area in the CV curves than MCA which typically indicates higher capacitance (**Figure 2.5 a, c**). The volumetric capacitance of N-MCA and MCA were calculated based on their GCD curves (**Figure 2.5 b, d**). N-MCA achieved a volumetric capacitance of 2224.0 mF cm^{-3} at 0.5 mA cm^{-2} and retained 67.2% of it at 20 mA cm^{-3} (**Figure 2.4b**). Meanwhile, MCA achieved a volumetric capacitance of 1570.6 0 mF cm^{-3} at 0.5 mA cm^{-2} and retained 53.0% of it at 20 mA cm^{-3}.

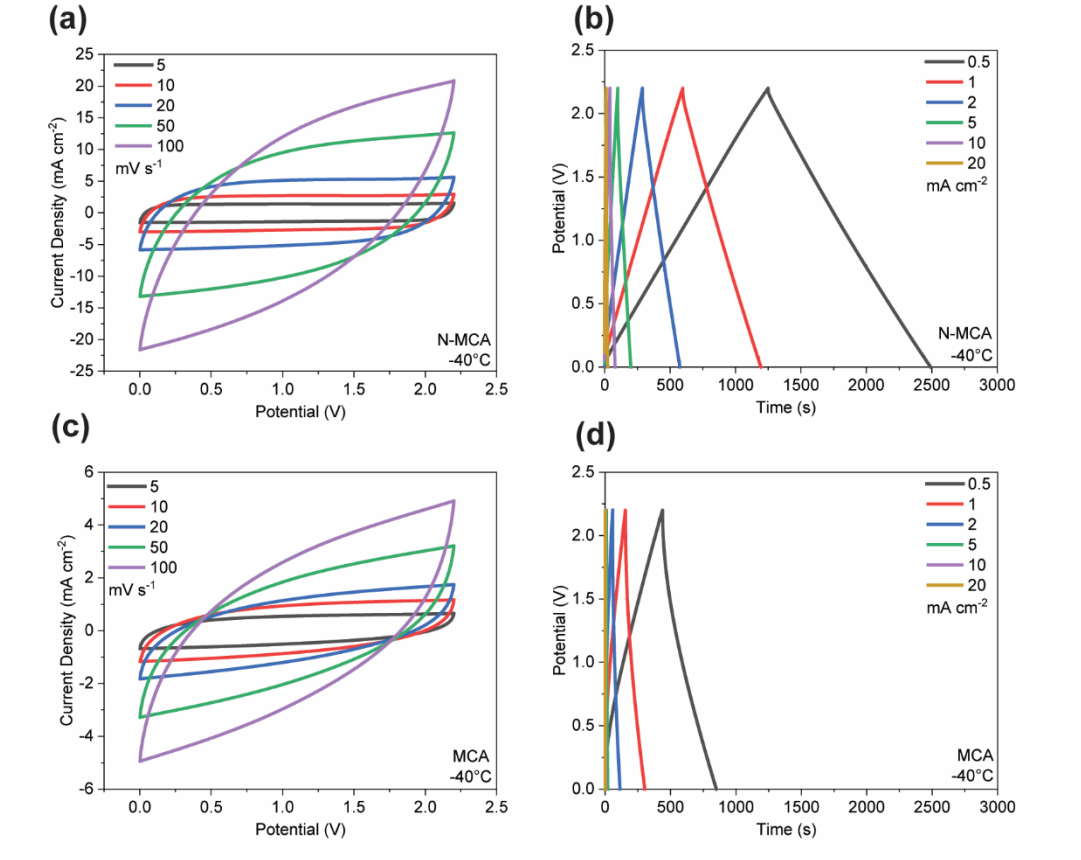


Figure 2.6. Cyclic voltammetry (CV) and galvanostatic charging and discharging (GCD) curves of (a,b) N-MCA and (c,d) MCA collected at -40°C, respectively.

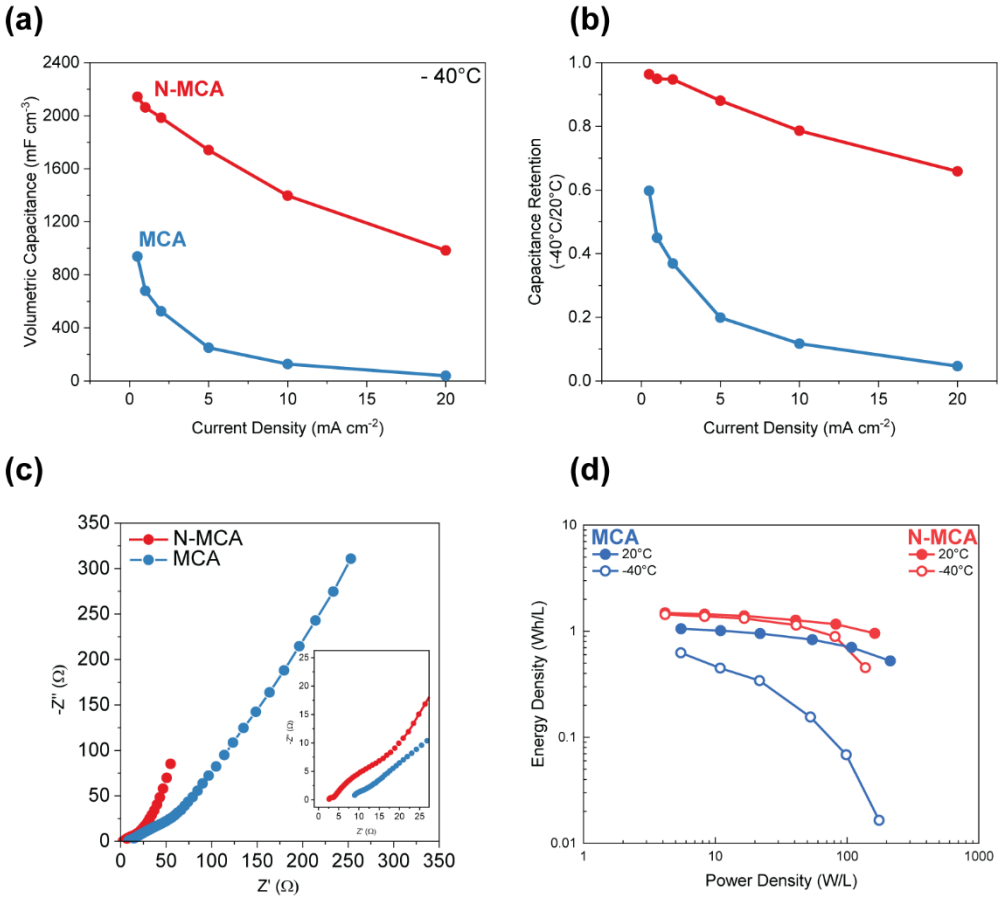


Figure 2.7 (a) Volumetric Capacitance of N-MCA and MCA obtained at -40 °C at different current densities. (b) Capacitance retention ratio of N-MCA and MCA as a function of current densities obtained at -40 °C and 20 °C. (c) Nyquist plots of MCA and N- MCA devices at operating temperature of -40 °C. (d) Ragone plot of N-MCA and MCA devices at 20°C and -40°C.

The discrepancy between the performance of N-MCA and MCA became more pronounced as the operating temperature reduced to -40°C (**Figure 2.6, Figure 2.7**). Even at -40°C, N-MCA exhibited the more rectangular-shaped cyclic voltammogram profile at scan rate of 5 mV s^{-1} than MCA (**Figure 2.6a,a**). This suggests that electron

transport and ion diffusion are highly efficient. Similarly, the GCD profile of N-MCA at -40 °C and low current density of 1 mA cm^{-2} exhibited more triangular than the MCA, supporting the same conclusion. (**Figure 2.6b, d**). At -40°C, N-MCA electrode achieved a volumetric capacitance of 2142.7 mF cm^{-3} at current density of 0.5 mA cm^{-2} which is significantly higher than that of MCA (938.3 mF cm^{-3}) (**Figure 2.7a**). Most importantly, the N-MCA electrode retained 46% of its volumetric capacitance from 0.5 to 20 mA cm^{-2} at -40 °C and MCA electrode only retained 4.1% at the same conditions. The ability of the device to retain their room temperature capacitance at low operating temperature plays a critical role in determining their overall performance.[9] N-MCA achieved a high capacitance retention ratio of a 0.95 ratio at the current density of 1mA cm^{-2} which is significantly higher than that of MCA (0.45) (**Figure 2.7b**). It also outperforms previously reported carbon electrodes tested at similar temperatures (**Table 2.1**).[15,19–23] The resistance of N-MCA and MCA were compared via the electrochemical impedance spectroscopy (EIS) analysis (**Figure 2.7c**). Nyquist plot revealed that N-MCA has a very small series resistance and has steep slope in the low frequency domain compared to MCA which indicates that ion transport in the porous electrode is very efficient even at -40°C. These results reflect the high energy and power density retention of N-MCA at low operating temperature compared to MCA (**Figure 2.7d**). At -40°C, N-MCA delivered a maximum energy density of 1.43 Wh L^{-1} (4.16 W L^{-1}) and retained 0.45 Wh L^{-1} at high power density of 138 W L^{-1}. Meanwhile, MCA delivered a maximum energy density of 0.63 Wh L^{-1} (5.48 W L^{-1}) and retained only 0.02 Wh L^{-1} at high power density of 175.24 W L^{-1}. These results suggest that

introducing nitrogen functional groups is essential for retaining device's capacitive performance even at low operating temperatures.

The enhanced capacitance of N-MCA can be attributed to the synergistic effect of additional pseudocapacitance from nitrogen functional groups and electronic structure modulation, which increase the quantum capacitance, electrical conductivity, and ion adsorption energies.[2,17,24–29] Previous works by Zhan et al. elucidated the role of nitrogen-doping in the capacitance of the graphene.[24] Through probing the electric density of states near the Fermi level, they found that graphitic-N and pyridinic-N shift the Dirac point to high and lower energy position. They also found that pyrrolic does not alter the electronic structure of the pure graphene. This work is complementary to the theoretical analysis part conducted by Dai et al. where they elucidate the effect of each nitrogen functional group (pyrrolic-N, pyridinic-N, and graphitic-N) on the performance enhancement of the carbon-based supercapacitors.[30] Dai et al. found that adsorption energy increases in the order of pyrrolic-N. graphitic-N, and pyridinic-N.[30] The higher the adsorption energies, the stronger the attraction between the electrolyte ions and the electrode surface and thus results higher capacitance.[30,31]

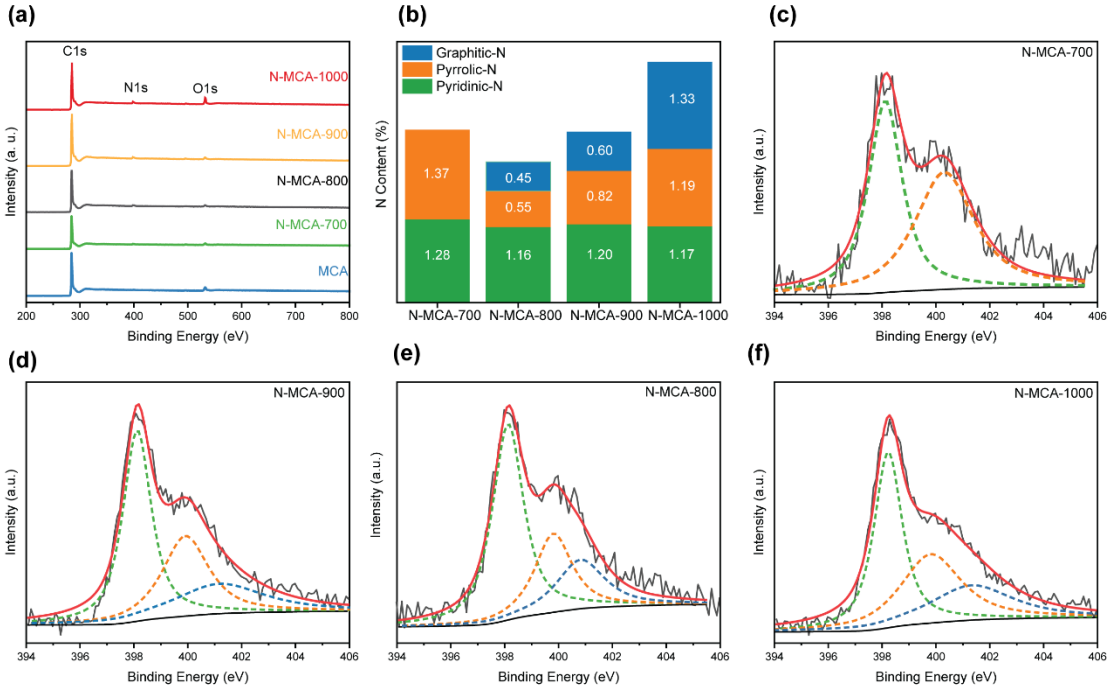


Figure 2.8. a. XPS survey spectra of MCA, N-MCA-700, N-MCA-800, N-MCA-900, and N-MCA-1000. b. Histograms comparing the atomic concentration of pyridinic-N, pyrrolic-N, and graphitic-N of N-MCAs. N 1s core level XPS spectra of c. N-MCA-700, d. N-MCA-800, e. N-MCA-900, and f. N-MCA-1000. Dashed lines outline the deconvoluted peaks corresponding to pyridinic-N (green), pyrrolic-N (orange), and graphitic-N (blue).

Previous works showed that capacitance is directly proportional to dopant concentration.[14,17,32] Here, we tuned the nitrogen doped concentration by adjusting the NH_3/N_2 post-treatment temperature. The highly porous MCA underwent NH_3/N_2 post-treatment at lower temperatures of 700, 800, and 900 °C. The resultant electrodes were donated as N-MCA-700, N-MCA-800, and N-MCA-900. From the XPS survey

spectrum of N-MC-A-700, N-MCA-800, N-MCA-900, and N-MCA-1000, the nitrogen content was quantified by integrating the N1s peak area as a function of photon energy (394-406 eV) and normalizing it to the sum of the corrected elemental areas using their respective photo-ionization cross section.[33] The calculated nitrogen contents are 2.65%, 2.16% 2.62%, 3.69% for N-MC-A-700, N-MCA-800, N-MCA-900, and N-MCA-1000, respectively **(Figure 2.8a-b**). The nitrogen content decreased as the treatment temperature increased from 700°C to 800°C and then increase again at 900 °C is consistent with previous observations.[34,35] Above the NH_3 /N_2 treatment temperature 800°C, the nitrogen content increased due to the corrosion effect of NH_3 which etched the carbon and introduced more sites for nitrogen doping.[17] The ratio between different N moieties changed with respect to the treatment temperature. The N 1s core level XPS spectra were analyzed and revealed the chemical nature of the N functionalities of the doped MCA at different post-treatment temperatures (**Figure 2.8c-f**). Not just the dopant concentration is important, the capacitance of the electrode also depends on the type of functional groups.[2,30,34] As treatment temperature increased, the content of pyridinic-N remained relatively the same, pyrrolic-N decreased and then increased above 800 °C, and graphitic-N increased as expected.[34,36] It is reported that the incorporated N sites can further react with NH_3, introducing micropore and mesopores, and thus increase the surface.[27,37]

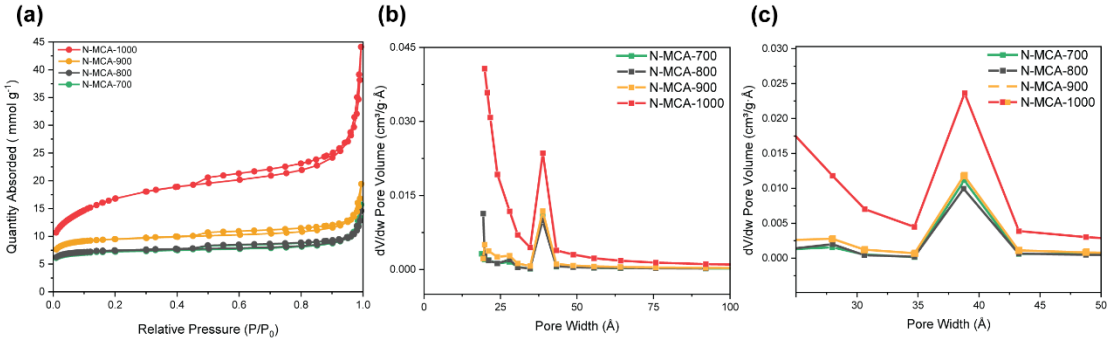


Figure 2.9. (a) Nitrogen absorption–desorption isotherm and (b) pore size distribution profile of N-MCA-700, N-MCA-800, N-MCA-900, and N-MCA-1000. (c) Inset in (b) shows the pore volume from 25 to 50 Å pore width.

Brunauer-Emmett-Teller measurements (BET) were conducted on the N-doped MCAs. The nitrogen adsorption-desorption isotherms of all N-MCAs were compared (**Figure 2.9a**). Increased in the adsorbed nitrogen at low ($P/P_0 < 0.1$) and high pressure suggests the presence of micropores and macropores, respectively.[12,13] The presence of mesopores is suggested by the hysteresis observed at $0.4 < P/P_0 < 1.0$. N-MCA-1000 electrode has the highest absorbed nitrogen compared to the rest of the N-doped MCA electrodes. The pore distribution profile (**Figure 2.9b, c**) shows that N-MCA-1000 has a substantially higher amount of micropores and mesopores compared to N-MC-A-700, N-MCA-800, and N-MCA-900. This result indicates that NH_3 etching also occurs at 1000°C aside from N-doping. N-MC-A-700, N-MCA-800, N-MCA-900, and N-MCA-1000 exhibited a BET specific surface area of 636.4, 649.1, 832.2, 1296.4 $m^2 g^{-1}$, respectively. These results demonstrated the direct relationship between NH_3 /N_2 treatment temperature, surface area, and nitrogen content.

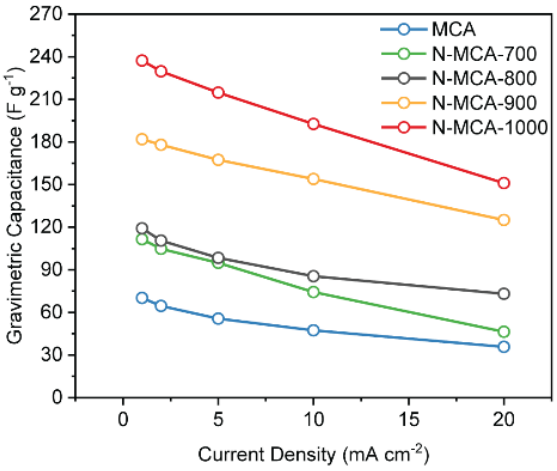


Figure 2.10. Gravimetric capacitance of MCA and N doped MCA collected in 0.5M $TEABF_4$ in 1:1 acetonitrile and methyl formate electrolyte via three-electrode testing configuration with carbon paper and platinum wire as counter and reference electrodes, respectively.

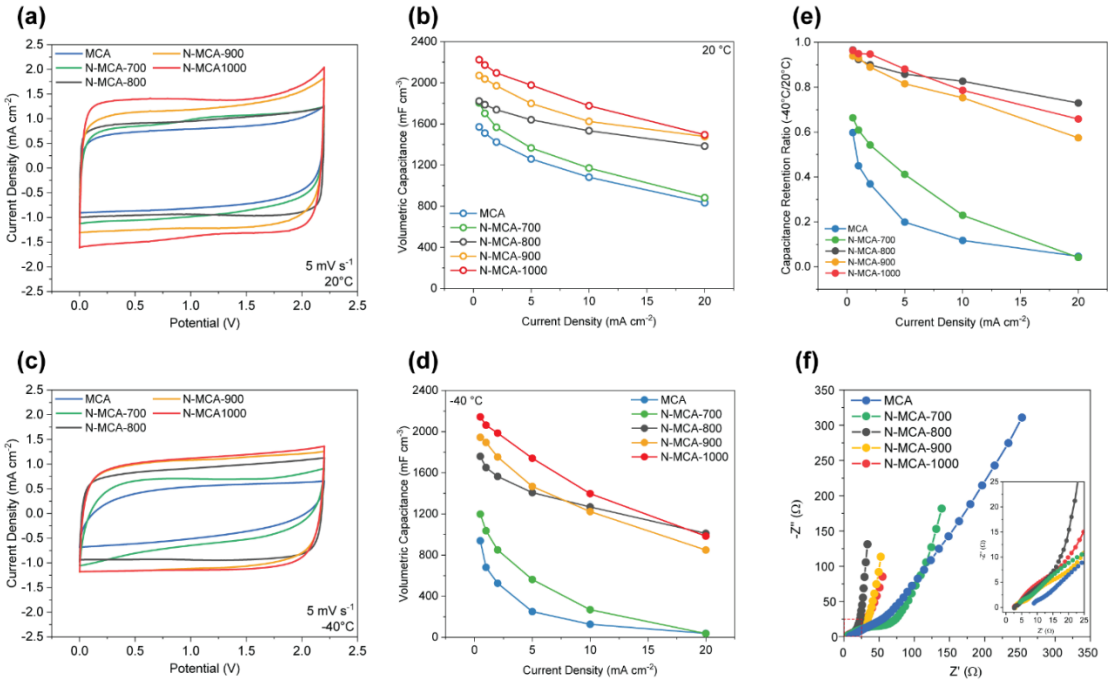


Figure 2.11. CV curves of N-doped and undoped MCAs devices collected at scan rate

of 5 mV s^{-1} and at operating temperature of (a) 20°C and (c) -40°C. Volumetric capacitance of N doped and undoped MCA obtained at operating temperature of (b) 20 °C and (d) -40 °C as a function of current density. (e) Capacitance retention ratio of N-doped and undoped as a function of current densities obtained at -40 °C and 20 °C. (f) Nyquist plot of MCA and N doped MCA devices at operating temperature of -40 °C. Inset highlighting high- and intermediate-frequency domains.

The performance of N-MCAs electrodes was first evaluated in a three-electrode cell at room temperature using 0.5M $TEABF_4$ in 1:1 AN/MF as the electrolyte, and carbon paper and platinum wire as counter and reference electrodes, respectively. As presented in **Figure 2.10**, gravimetric capacitance of the electrodes increases as the NH_3/N_2 post-treatment temperature increased. To evaluate the performance of the other three electrodes as a function of operating temperature, symmetric supercapacitors based on these electrodes (N-MCA-700, N-MCA-800, N-MCA-900) were also fabricated. CV and GCD curves of symmetric supercapacitor devices with N-MCA-700, N-MCA-800, N-MCA-900 electrodes as a function of scan rates and current densities were collected at 20°C. **Figure 2.11 a** compares the CV curves of MCA, N-MCA-700, N-MCA-800, N-MCA-900, and N-MCA-1000 symmetric devices at 5 mV s^{-2} and at 20°C. The volumetric capacitance of the supercapacitor devices was calculated from the GCD curves. At 20°C, the volumetric capacitance of the devices is directly proportional to the NH_3/N_2 post-treatment temperature, with N-MCA-1000 achieved the highest capacitance due to the optimized nitrogen content (**Figure 2.11b**).

The difference between the performance of the five different devices became more pronounced at the operating temperature of -40°C (**Figure 2.11c-d**). **Figure 2.11c** displays that the CV curves of N-MCA-800, N-MCA900, and N-MCA-1000 at -40°C and scan rate of 5 mV s^{-1} are more rectangular shape than MCA and N-MCA-700, indicating that NH_3/N_2 post-treatment temperature of 800-1000°C enhanced ion diffusion kinetics and electron transport property of the electrode. Linear relationship between the NH_3/N_2 post-treatment temperature and the volumetric capacitance were also observed when the supercapacitor devices were tested at low current densities and at - 40°C (**Figure 2.11d**). As the current density increased from 0.5 mA cm^{-2} to 20 mA cm^{-2}, N-MCA-800, N-MCA-900 and N-MCA-1000 retained 57%, 44% and 46% of their capacitance, respectively. Meanwhile, the capacitance of N-MCA-700 and MCA drastically decreased to 4%. Compared to N-MCA-700 and MCA, the other three N-MCAs contain graphitic-N which could increase the electrical conductivity of the electrode via its electron-donating nature.[17,38,39] The volumetric capacitance retention ratio of the devices at -40°C relative to their performance at 20°C under a current density of 1mA cm^{-2} were calculated, and found that N-MCA-800, N-MCA-900, and N-MCA-1000 exhibited high ratio of 0.92, 0.93, and 0.95, respectively (**Figure 2.11e**). Even at current density of 20 mA cm^{-2}, all the three devices maintained high capacitance retention ratio. However, N-MCA-800 maintained higher retention ratio than N-MCA-1000 at high charging rates. The reduction of the capacitance of N-MCA-1000 at higher charging rates can be ascribed to higher surface defects than N-MCA-800. Electrochemical impedance spectroscopy was performed at -40°C and fitted the

data with proper equivalent circuits (**Figure 2.11f).** At high frequency region on the Nyquist plot, N-MCA-700, N-MCA-800, N-MCA-900 and N-MCA-1000 exhibit similar series resistances (3.7, 2.7, 2.9, and 2.6 Ω, respectively). Meanwhile, MCA exhibits high series resistance (7.9 Ω). However, these initial resistance values primarily indicate electrical connectivity and intrinsic material conductivity, thus having limited significance in evaluating pseudocapacitive behavior (**Table 2.2**). In contrast, in the low-frequency regions, the N-doped MCAs demonstrate notably steep slopes compared to the undoped MCA, highlighting their superior transport efficiency and enhanced pseudocapacitive properties. Further insight into the electrodes' characteristics can be derived through analysis of the constant phase element (CPE, Q) from the equivalent circuit modeling of the electrochemical impedance spectroscopy data.[40–42] The magnitude of Q directly correlates with the pseudocapacitive capacity of the electrodes; higher Q values indicate increased electrochemically active surface areas and/or superior capacitive behavior. Additionally, the CPE exponent (α) quantifies the degree of surface heterogeneity. In particular, N-MCA-1000 exhibits the lowest α value (0.747) among the N-doped MCAs, suggesting a more porous and heterogeneous structure. This observation aligns well with the BET surface area results. These results confirm that increasing the NH_3/N_2 post-treatment temperature not only increases the N content, but also enhanced active surface area, and thus improving the overall capacitance.

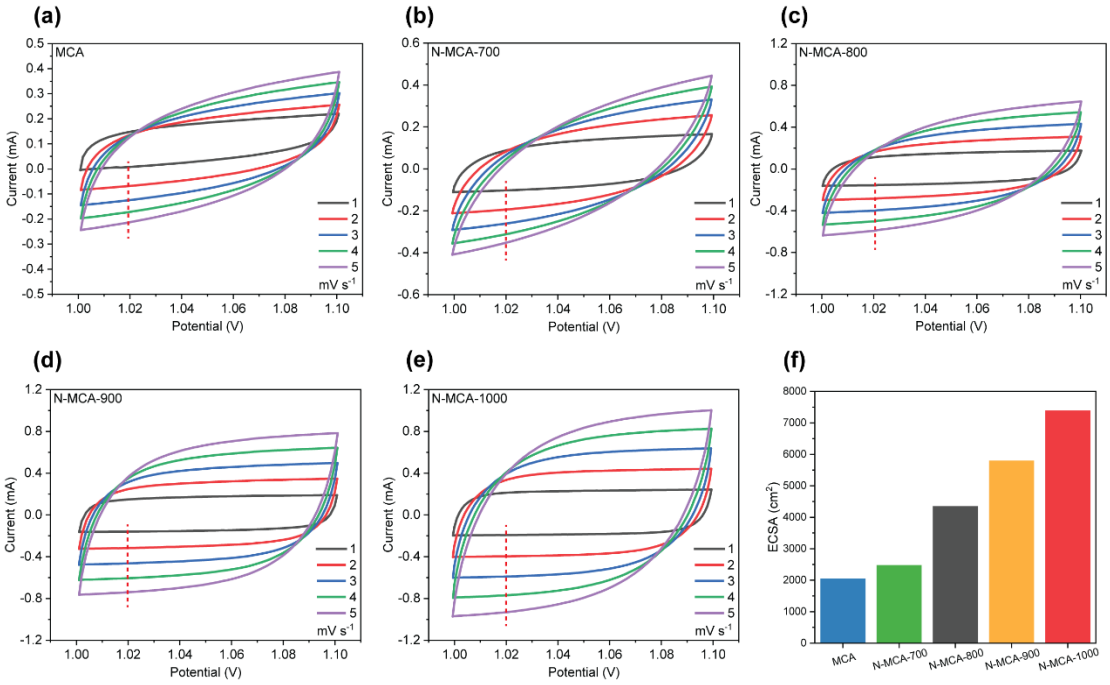


Figure 2.12. CV curves of (a) MCA, (b) N-MCA-700, (c) N-MCA-800, (d) N-MCA-900, and e. N-MCA-1000 collected at 20°C. Dashed lines in the CV curves highlight the current collected at 1.02 V. f. Cathodic current obtained at 1.02V plotted as a function of scan rates. (f) Histogram of the calculated ECSAs of MCA (2055.1 cm^2), N-MCA-700 (2482.5 cm^2), N-MCA-800 (4350.1 cm^2), N-MCA-900 (5797.9 cm^2), and N-MCA-1000 (7395.2 cm^2).

The electrochemical surface area of symmetric devices based on MCA, N-MCA-700, N-MCA-800, N-MCA-900, N-MCA-1000 electrodes were determined using the method from previous work.[13] Cyclic voltammetry curves were collected within the potential window of 1 to 1.1V. EDLCs ($C_{EDLC,}$ F) of the devices were determined by linearly fitting the cathodic and anodic current (mA) at 1.02V against scan rates from 1 to 5 mV s^{-1} (**Figure 2.12a-e**). It's noteworthy that ECSA varies with

the scan rates used. The C_{EDLC} of each device was divided by the nominal capacitance (C_{ref}) of the electrode material on a unit surface area, as stated in the Eq.6:

$$ECSA = \frac{C_{EDLC}}{C_{ref}} \qquad \text{(Eq 2.6)}$$

For the calculation, we used 25 μF cm^{-2} as the nominal capacitance (C_{ref}) for carbon.[13] The calculated ECSA values show that N-MCA-1000 (7395.3 cm^2) has the highest surface area among all N-doped MCAs (**Figure 2.12f**).

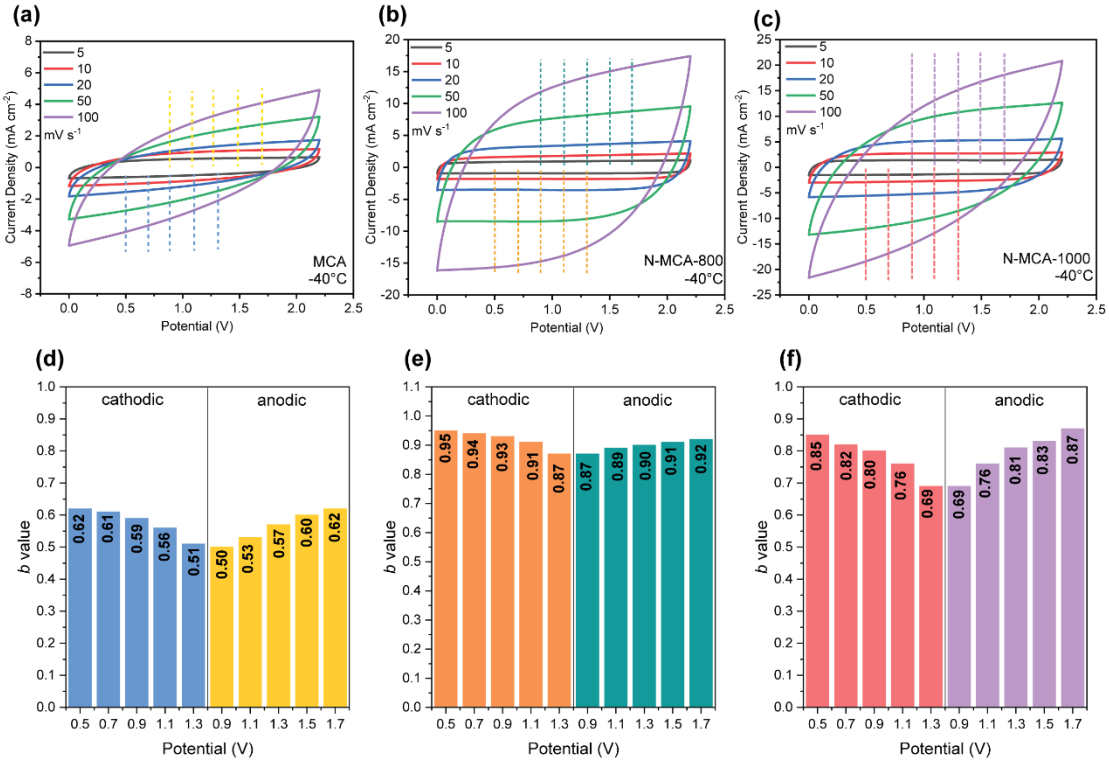


Figure 2.13. CV curved of (a) MCA, (b) N-MCA-800, and (c) N-MCA-1000 at -40 °C. Dashed lines highlight the potential selected for calculating the *b* values. Histogram of the *b* values of (d) MCA, (e) N-MCA-800, and (f) N-MCA-1000 calculated from cathodic and anodic currents of CV curves.

Kinetic analysis was conducted to better understand the low temperature capacitance behavior of MCA and the N-doped MCAs with the highest capacitance retention under high charge-discharge rates (N-MCA-800) and volumetric capacitance (N-MCA-1000). Cyclic voltammetry could provide insight into the difference in charge storage kinetics.[43] The quasi-rectangular shaped of N-MCA-800's CV curves at -40°C signifies fast electron and ion transport (**Figure 2.13a**). In contrast, the N-MCA-1000 and MCA's CV curves are less rectangular shaped (**Figure 2.13b, c**). Current density (i) is relates with the scan rate (v) through $i=kv^b$.[13,16,44–46] The b exponent indicates whether the charge storge kinetics represent the ideal capacitive behavior (b= 1) or a diffusion-controlled process (b=0.5).[13,16,44,46] The b value can be calculated by plotting the logarithm of the absolute current densities versus the logarithm of scan rate ($\log i = b\log v$ +k). At the potential of 0.5 V and operating temperature of -40°C, the calculated b value for N-MCA-800, N-MCA-1000, and MCA are 0.95, 0.85, and 0.62, respectively. To get a full picture of the kinetics of N-MCA-800, N-MCA-1000, and MCA at -40°C, the b values under different potentials for both cathodic and anodic currents were analyzed (**Figure 2.13 d-f**). The b values of N-MCA-800 and N-MCA-1000 are considerably higher than those of MCA. This indicates that nitrogen functional groups allow efficient ion diffusion, especially at low operating temperatures. The b value of N-MCA-800 is higher than that N-MCA-1000, indicating faster ion diffusion, which reflects its excellent volumetric capacitance retention at high charge-discharge rates.

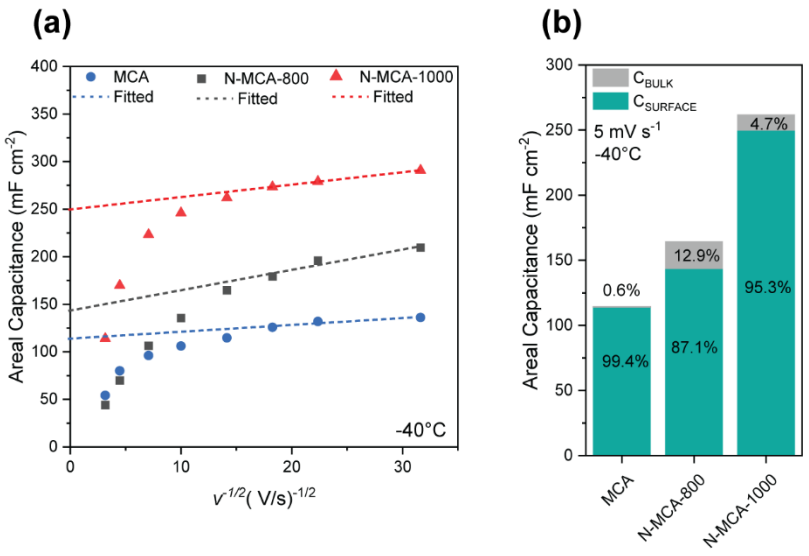


Figure 2.14. (a) Plot of areal capacitance versus $v^{-1/2}$ for MCA, N-MCA-800, and N-MCA-1000. Capacitance contributed by the surface obtained from the slope of the linear fit. (b) Histogram illustration of capacitance contributions in MCA, N-MCA-800, and N-MCA-1000 at a scan rate of 5 mV s^{-1}.

Quantitative analysis on the capacitance contribution of N doped and undoped MCA at -40°C were conducted via Trasatti method.[18,47] The areal capacitance based on the area of the electrodes were calculated from the cyclic voltammetry curves obtained from the scan rates ranging from 1-100 mV s^{-1} and plotted against $v^{-1/2}$ (v is scan rate) (**Figure 2.14a**). Linear fit was extrapolated at low scan rates and the determined the y-intercept ($v \rightarrow +\infty$) which represents the areal capacitance contributed by the surface ($C_{SURFACE}$). At 5mV/s, capacitance of MCA is mainly from the surface (**Figure 2.14b**). Meanwhile, the capacitance of N-MCA-800 and N-MCA-1000 are from the bulk (C_{BULK}) and surface ($C_{SURFACE}$) which increases its overall capacitance

at -40°C. The higher capacitance contributed by the surface observed for N-MCA-1000 compared to N-MCA-800 is most likely attributed to its larger surface area.

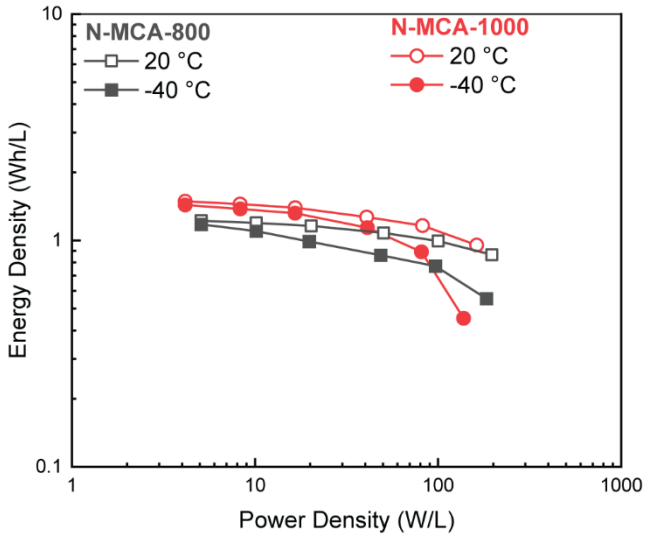


Figure 2.15. Volumetric energy and power densities of symmetric device with N-MCA-800 and N-MCA-1000 electrodes tested at 20 and -40 °C.

The volumetric energy and power densities of N-MCA-800 and N-MCA-1000 at 20°C and -40°C were calculated and compared in the Ragone plot on **Figure 2.15**. The high volumetric capacitance of N-MCA-1000 leads to a maximum energy density of 1.49 Wh L^{-1} (4.16 W L^{-1}) and maintained at 0.95 Wh L^{-1} at high power density of 1624.30 W L^{-1}. At -40°C, N-MCA-1000 delivered a maximum energy density of 1.43 Wh L^{-1} (4.16 W L^{-1}) and maintained at 0.45 Wh L^{-1} at high power density of 138 W L^{-1}. In addition, N-MCA-800 delivered slightly lower energy density but higher power density than N-MCA-1000. N-MCA-8000 possesses a maximum energy density of 1.22 Wh L^{-1} (5.09 W L^{-1}) and maintained at 0.87 Wh L^{-1} at high power density of 196.43 W L^{-1} at 20°C. At low temperature of -40°C, N-MCA-800 delivered a maximum energy

density of 1.18 Wh L^{-1} (5.08 W L^{-1}) and maintained at 0.55 Wh L^{-1} at high power density of 183.56 W L^{-1}. Both N-MCA-800 and N-MCA-1000 achieved high retention rates at low operating temperature. Furthermore, the performance of N-MCA-800 and N-MCA-1000 suggests that there's compromise between achieving high capacitance and maintaining high retention rate at low operating temperatures.

2.5 Conclusion

In conclusion, we have demonstrated that nitrogen dopant enhances the capacitance of multiscale porous carbon at low operating temperature. The N-doped MCA exhibited a higher volumetric capacitance than the pristine MCA, especially at low operating temperature. At -40°C, N-doped MCA (N-MCA-1000) achieved a high volumetric capacitance of 2142.7 mF cm^{-3} and retained 95% of its room temperature capacitance. Meanwhile, MCA only achieved 938.3 mF cm^{-3} which is 45% of its room temperature capacitance. This enhancement arises from the synergistic contributions of pseudocapacitance and electronic structure modulation, which increase electrical conductivity and ion adsorption energies. In addition, the content of nitrogen dopant can be adjusted by tuning the NH_3/ N_2 post-treatment temperature. At post-treatment temperature of 1000°C, NH_3 NH_3 etching also occurs at the same time as N- doping. Although N-MCA-1000 possesses high nitrogen content, porosity, and delivers the highest capacitance, N-MCA-800 demonstrated superior volumetric capacitance retention under low operating temperatures. We found that the balance between porosity and nitrogen content plays a critical role in enhancing the ion diffusion and

electron transport which are limiting factors for electrode performance at low operating temperature. Findings from this work demonstrate a new electrode design principle.

Table 2.1 The electrochemical performance of other carbon-based electrodes at -40°C.

Electrodes	Electrolyte	Temp. (°C)	Retention Relative to room temp.	Ref.
Microwave exfoliated graphite oxide// Microwave exfoliated graphite oxide	PYR_{14}-FSI	-40	70% @ 1 mV s^{-1}	[19]
N-doped graphene/carbon nanotube hydrogel// N-doped graphene/carbon nanotube hydrogel	37% H_2SO_4	-40	90% @ 1mA cm^{-2}	[20]
Carbon fabric // Carbon fabric	37% H_2SO_4	-40	83% @ 1mA cm^{-2}	[21]
3DP DQ/GC// 3DP PANI/GC	9.5 M H_3PO_4	-40	66% @ 1mA cm^{-2}	[22]
3D WO_3/CNT/KB// 3D PBA/CNT/ KB	0.5M H_2SO_4 /ethylene glycol	-40	64% @ 1mA cm^{-2}	[23]
3DP PDAN/CNT/rGO// 3DP PBA/CNT/rGO	9.5 M H_3PO_4	-40	73% @ 2mA cm^{-2}	[15]
N-MCA-1000//N-MCA-1000	0.5M $TEABF_4$ in AN/MF	-40	96% @ 2mA cm^{-2}	This work

Table 2.2. Electrode characteristic values derived through analysis of the constant phase element (CPE, Q) from the equivalent circuit modeling of the electrochemical impedance spectroscopy data.

Electrodes	**Q (F $s^{(\alpha-1)}$)**	**α**
MCA	0.01457	0.6274
N-MCA-700	0.04918	0.7875
N-MCA-800	0.1096	0.9569
N-MCA-900	0.1112	0.9026
N-NCA-1000	0.0921	0.7470

2.6 References

1. Viola, W. & Andrew, T. L. An Aqueous Eutectic Electrolyte for Low-Cost, Safe Energy Storage with an Operational Temperature Range of 150 °C, from −70 to 80 °C. *J. Phys. Chem. C* **125**, 246–251 (2021).
2. Komal Zafar, H. *et al.* Recent Advances on Nitrogen-Doped Porous Carbons Towards Electrochemical Supercapacitor Applications. *The Chemical Record* **24**, e202300161 (2024).
3. Li, Z. *et al.* 40 Years of Low-Temperature Electrolytes for Rechargeable Lithium Batteries. *Angewandte Chemie International Edition* **62**, e202303888 (2023).
4. Pinongcos, A. B., Xue, X., Chandrasekaran, S., Worsley, M. A. & Li, Y. Innovative Electrode Design for Low-Temperature Electrochemical Energy Storage: A Mini Review. *Energy Fuels* **39**, 6078–6096 (2025).
5. Chodankar, N. R. *et al.* Supercapacitors operated at extremely low environmental temperatures. *J. Mater. Chem. A* **9**, 26603–26627 (2021).
6. Zhao, T. *et al.* A Supercapacitor Architecture for Extreme Low-Temperature Operation Featuring MXene/Carbon Nanotube Electrodes with Vertically Aligned Channels and a Novel Freeze-Resistant Electrolyte. *Advanced Functional Materials* **34**, 2314825 (2024).
7. Hong, J.-Y., Bak, B. M., Wie, J. J., Kong, J. & Park, H. S. Reversibly Compressible, Highly Elastic, and Durable Graphene Aerogels for Energy Storage Devices under Limiting Conditions. *Advanced Functional Materials* **25**, 1053–1062 (2015).

8. Smart, M. C. *et al.* The use of lithium-ion batteries for JPL's Mars missions. *Electrochimica Acta* **268**, 27–40 (2018).
9. Liu, Y. *et al.* Flexible supercapacitors with high capacitance retention at temperatures from −20 to 100 °C based on DMSO-doped polymer hydrogel electrolytes. *J. Mater. Chem. A* **9**, 12051–12059 (2021).
10. Brandon, E. J., Smart, M. C. & West, W. C. Low-temperature performance of electrochemical capacitors using acetonitrile/methyl formate electrolytes and activated carbon fabric electrodes. *Journal of Materials Research* **35**, 113–121 (2020).
11. Huang, Z. *et al.* A comprehensive review on liquid electrolyte design for low-temperature lithium/sodium metal batteries. *Energy & Environmental Science* **17**, 5365–5386 (2024).
12. Zhang, F. *et al.* Multiscale Pore Network Boosts Capacitance of Carbon Electrodes for Ultrafast Charging. *Nano Lett.* **17**, 3097 (2017).
13. Yao, B. *et al.* Printing Porous Carbon Aerogels for Low Temperature Supercapacitors. *Nano Lett.* **21**, 3731–3737 (2021).
14. Ilnicka, A. *et al.* Combined effect of nitrogen-doped functional groups and porosity of porous carbons on electrochemical performance of supercapacitors. *Sci Rep* **11**, 18387 (2021).
15. Zhang, M. *et al.* 3D-printed redox-active polymer electrode with high-mass loading for ultra-low temperature proton pseudocapacitor. *Advanced Powder Materials* **4**, 100247 (2025).

16. Yao, B. *et al.* 3D-Printed Structure Boosts the Kinetics and Intrinsic Capacitance of Pseudocapacitive Graphene Aerogels. *Advanced Materials* **32**, 1906652 (2020).
17. Liu, T. *et al.* Tuning the Electrochemical Properties of Nitrogen-Doped Carbon Aerogels in a Blend of Ammonia and Nitrogen Gases. *ACS Appl. Energy Mater.* **1**, 5043–5053 (2018).
18. Ardizzone, S., Fregonara, G. & Trasatti, S. "Inner" and "outer" active surface of RuO2 electrodes. *Electrochimica Acta* **35**, 263–267 (1990).
19. Tsai, W.-Y. *et al.* Outstanding performance of activated graphene based supercapacitors in ionic liquid electrolyte from −50 to 80 °C. *Nano Energy* **2**, 403–411 (2013).
20. Liang, S. *et al.* Nitrogen-doped graphene/carbon nanotube hydrogel for high-performance, low-temperature supercapacitor. *Ionics* **31**, 6191–6203 (2025).
21. Xiang, M. *et al.* Low temperature electrochemical properties and energy storage mechanisms of gently modified porous carbon fabric-based flexible supercapacitors. *Chemical Engineering Journal* **501**, 157620 (2024).
22. Zhang, M. *et al.* An Ultrafast and Ultralow-Temperature 3D-Printed All-Organic Proton Pseudocapacitor. *Advanced Functional Materials* **35**, 2413436 (2025).
23. Zhang, M. *et al.* A 3D-Printed Proton Pseudocapacitor with Ultrahigh Mass Loading and Areal Energy Density for Fast Energy Storage at Low Temperature. *Advanced Materials* **35**, 2209963 (2023).

24. Zhan, C., Zhang, Y., Cummings, P. T. & Jiang, D. Enhancing graphene capacitance by nitrogen: effects of doping configuration and concentration. *Phys. Chem. Chem. Phys.* **18**, 4668–4674 (2016).

25. Tang, R. Evolution of the understanding of quantum capacitance through advancements in graphene-related carbon materials. *Carbon Lett.* **34**, 1845–1849 (2024).

26. Xu, Q., Yang, G., Fan, X. & Zheng, W. Improving the Quantum Capacitance of Graphene-Based Supercapacitors by the Doping and Co-Doping: First-Principles Calculations. *ACS Omega* **4**, 13209–13217 (2019).

27. Luo, W. *et al.* Pyrolysis of Cellulose Under Ammonia Leads to Nitrogen-Doped Nanoporous Carbon Generated Through Methane Formation. *Nano Lett.* **14**, 2225 (2014).

28. Ghosh, S., Barg, S., Jeong, S. M. & Ostrikov, K. (Ken). Heteroatom-Doped and Oxygen-Functionalized Nanocarbons for High-Performance Supercapacitors. *Advanced Energy Materials* **10**, 2001239 (2020).

29. Karakaya, M. *et al.* Roll-to-roll production of spray coated N-doped carbon nanotube electrodes for supercapacitors. *Appl. Phys. Lett.* **105**, 263103 (2014).

30. Dai, P. *et al.* Cotton fabrics-derived flexible nitrogen-doped activated carbon cloth for high-performance supercapacitors in organic electrolyte. *Electrochimica Acta* **354**, 136717 (2020).

31. Bo, Z. *et al.* Design of Supercapacitor Electrodes Using Molecular Dynamics Simulations. *Nano-Micro Lett.* **10**, 33 (2018).

32. Sun, L. *et al.* Nitrogen-doped graphene with high nitrogen level via a one-step hydrothermal reaction of graphene oxide with urea for superior capacitive energy storage. *RSC Adv.* **2**, 4498–4506 (2012).

33. Yeh, J. J. & Lindau, I. Atomic subshell photoionization cross sections and asymmetry parameters: $1 \leqslant Z \leqslant 103$. *Atomic Data and Nuclear Data Tables* **32**, 1–155 (1985).

34. Nagaiah, T. C., Kundu, S., Bron, M., Muhler, M. & Schuhmann, W. Nitrogen-Doped Carbon Nanotubes as A Cathode Catalyst for the Oxygen Reduction Reaction in Alkaline Medium. *Electrochem. Commun.* **12**, 338 (2010).

35. Xu, X. *et al.* Natural Honeycomb-like structure cork carbon with hierarchical Micro-Mesopores and N-containing functional groups for VOCs adsorption. *Applied Surface Science* **565**, 150550 (2021).

36. Zuo, S., Zhang, W., Wang, Y. & Xia, H. Low-Cost Preparation of High-Surface-Area Nitrogen-Containing Activated Carbons from Biomass-Based Chars by Ammonia Activation. *Ind. Eng. Chem. Res.* **59**, 7527–7537 (2020).

37. Song, Y. *et al.* Nitrogen-Doped Carbon "Spider Webs" Derived From Pyrolysis of Polyaniline Nanofibers in Ammonia for Capacitive Energy Storage. *J. Mater. Res.* **33**, 1109 (2018).

38. Miao, Y. *et al.* Polydopamine/Melamine Sponge-Derived Compressible Carbon Foam for High-Performance Supercapacitors. *Langmuir* **41**, 2181–2190 (2025).

39. Wang, D. *et al.* Nitrogen-containing graphene networks with high volumetric capacitance and exceptional rate capability. *Carbon* **154**, 13–23 (2019).

40. Brug, G. J., van den Eeden, A. L. G., Sluyters-Rehbach, M. & Sluyters, J. H. The analysis of electrode impedances complicated by the presence of a constant phase element. *Journal of Electroanalytical Chemistry and Interfacial Electrochemistry* **176**, 275–295 (1984).
41. Lazanas, A. Ch. & Prodromidis, M. I. Electrochemical Impedance Spectroscopy─A Tutorial. *ACS Meas. Sci. Au* **3**, 162–193 (2023).
42. Mei, B.-A. *et al.* Physical Interpretations of Electrochemical Impedance Spectroscopy of Redox Active Electrodes for Electrical Energy Storage. *J. Phys. Chem. C* **122**, 24499–24511 (2018).
43. Kim, H.-S. *et al.* Oxygen vacancies enhance pseudocapacitive charge storage properties of MoO3−x. *Nature Mater* **16**, 454–460 (2017).
44. Wang, J., Polleux, J., Lim, J. & Dunn, B. Pseudocapacitive Contributions to Electrochemical Energy Storage in TiO2 (Anatase) Nanoparticles. *J. Phys. Chem. C* **111**, 14925–14931 (2007).
45. Lindström, H. *et al.* Li+ Ion Insertion in TiO2 (Anatase). 2. Voltammetry on Nanoporous Films. *J. Phys. Chem. B* **101**, 7717–7722 (1997).
46. Liu, T., Zhou, Z., Guo, Y., Guo, D. & Liu, G. Block copolymer derived uniform mesopores enable ultrafast electron and ion transport at high mass loadings. *Nat Commun* **10**, 675 (2019).
47. Lin, D. *et al.* 3D-Printed Graded Electrode with Ultrahigh MnO2 Loading for Non-Aqueous Electrochemical Energy Storage. *Advanced Energy Materials* **13**, 2300408 (2023).

Chapter 3

Mechanically Reinforced 3D-Printed Graphene Aerogel Electrodes via Covalent Crosslinking

3.1 Abstract

The poor mechanical properties of 3D printed graphene oxide aerogels hinder their applicability in practical device fabrication. Typically, the graphene sheets of the 3D printed graphene oxide aerogels are bonded through van der Waals forces which makes the overall structure mechanically unstable. Covalent crosslinking of the graphene sheets via gelation process enhanced the mechanical integrity of the graphene-based aerogels. Herein we reported a new method on developing 3D printed thin freestanding graphene aerogel electrodes with enhanced mechanical and surface chemistry properties. The 3D gelled GA achieved a high gravimetric capacitance of 35.7 F g^{-1} which is 8-fold higher than the non-gelled 3D GA at the same current density of 0.5 mA cm^{-2}. Furthermore, the surface property of 3D gelled GA boosts its capacitance even at low operating temperature of -40°C. Thus, the synergistic effect of the engineered porous structure and unique intrinsic properties of the 3D gelled GA electrode would make it a promising candidate for high performance thin electrode.

3.2 Introduction

The rapid development of portable, wearable, and miniature energy storage devices has prompted continuous advancements in material design and manufacturing technologies.[1] Three-dimensional (3D) printing has emerged as a promising technology for fabrication of electrochemical energy storage (EES) devices such as supercapacitors and batteries due to its customizability, process flexibility, precise geometry controllability, and minimizing fabrication cost. [2–8] While effective, traditional manufacturing methods including chemical vapor deposition, spin coating, and solution casting limit versatility and flexibility of device design and fabrication. Advances in 3D printing techniques provide flexibility in implementing state-of-the-art electrode designs, offering new possibilities in addressing challenges of energy storage such sluggish mass transport.[3,5,7]

Carbon aerogels have gained much attention as supercapacitor electrodes due to their unique porous structure that offers high surface area and good electrical conductivity properties.[9,10] In the past years, researchers utilized an extrusion-based 3D printing technique, also known as direct ink writing (DIW), to fabricate carbon aerogel electrodes with periodic pores which facilitate efficient ion diffusion, and thus improves its overall capacitance.[1,4,7,11] The synthesis method of the 3D printed graphene oxide-based aerogels are critical towards constructing the final product.[12] Most works on 3D printed graphene aerogel (GA) have been fabricated using the freeze-drying method which creates porous microstructures that are beneficial for variety of applications, particularly for energy storage.[4,13–15] However, these

microstructures often compromised the mechanical integrity of the material limiting their applicability in practical device fabrication. Devices such as coin cells generally require thin electrodes. Unfortunately, the 3D printed GAs are not well suited for fabricating thin electrodes. Although thickness can be adjusted by controlling the number of printed lattices in the z direction, we found that post-processing steps often induce structural damage such as cracking and several volumetric shrinkages. Therefore, a new way to develop mechanically robust, thin freestanding aerogels is needed.

Here, we present the development of 3D printed gelled graphene aerogels (3D gelled GA) with sufficient mechanical integrity and with 300 μm thickness. Our approach is based on directly cross-linking the functional groups (*e.g.* hydroxide and epoxide) which process interconnected graphene sheets.[16,17] The developing a printable graphene-ink capable of withstanding post-processing steps is the key challenges in this process. The 3D printed thin gelled GA electrode that combines high porosity with sufficient mechanical integrity, making it as a promising candidate for high performance thin electrode applications.

3.3 Experimental

3.3.1 3D gelled GA synthesis

The graphene oxide (GO) suspension with a concentration of 40 mg/mL was prepared by sonicating single layers GO sheets in MilliQ water at 12°C sonication bath for 24h. The suspension was then mixed with 3-4wt% of hydroxypropyl methylcellulose, 18-22wt% Pluronic F127, and 18.5wt% of 20wt% ammonium carbonate solution with respect to the GO suspension in a Thinky planetary mixer at 2000 rpm for 5 min.

3.3.2 3D printing

The prepared GO ink was loaded into a 10 mL syringe barrel and centrifuged at 5000 rpm for 2 minute to remove air bubbles. The ink was extruded through a micro nozzle (200 μm diameter) to pattern 3D structure on a glass substrate. The ink was then extruded by means of an air-powered fluid dispenser (Ultimus V, EFD), which provides pressure around 30-40 psi. The writing speed was kept at 10 mm sec^{-1}. Six layers of simple cubic lattices with multiple orthogonal layers of parallel cylindrical rods were printed. Each layer was stacked on the structure with a z spacing of 0.12 mm. After printing, the printed sample with the glass substrate was places in the sealed glass jar with Kimwipes® wetted with isooctane. The sealed glass jar was kept at 80°C for 48 h for the gelation process. The 3D printed samples were rinsed with water to remove from the glass substrate. The 3D printed samples were immersed in dry ice and freeze dried for 48 h in vacuum. The 3D printed aerogels

are then annealed in a tube furnace under nitrogen atmosphere at 1050°C for 3h with a heating rate of 2°C min^{-1} to form graphene aerogels.

3.3.3 Material Characterization

The structural properties of the 3D gelled GA were investigated with scanning electron microscopy (SEM) and energy-dispersive spectroscopy (EDS) using Thermo Scientific Scios 2 DualBeam, equipped with an Oxford Instruments AZtecLive Ultim Max 100 EDS detector. The chemical composition of the functional groups was investigated by X-ray photoelectron spectroscopy (XPS, Nexus X-ray Photoelectron Spectrometer) using monochromatic Al Kα X-ray (1486.6 eV) with 400 μm spot size. All the electrochemical measurements were conducted using electrochemical stations (BioLogic EC-Lab SP-300 and VMP-3e). The electrochemical performance of individual electrode was measured in a three-electrode configuration with carbon rod and saturated calomel electrode (SCE) as the counter and references electrodes, respectively.

3.3.4 Fabrication of Supercapacitors (SCs):

1. *Fabrication of aqueous SC:* The aqueous SC was fabricated a Kaptop tape-based pouch cell with two 3D gelled GA, separated with glass microfiber filter (Whatman 1820-125 GF/A, 1.6μm). Electrochemical measurements were performed in a 7.86 M LiCl solution at different temperatures. To evaluate the performance of the 3D gelled GA under applied pressure, split coin cell was fabricated with 3M KOH electrolyte. The two pieces of 3D

gelled GA were separated with cellulose-based separator (NKK separator, Nippon Kodoshi Corporation).

2. *Fabrication of solid-state SCs:* The solid-state symmetric SC device was assembled by separating the 3D gelled GA with glass microfiber filter (Whatman 1820-125 GF/A, 1.6μm). Gel electrolyte was prepared by mixing Polyvinyl alcohol (PVA) and 5M LiCl aqueous solution heated at 95°C for 2 h under vigorous stirring. The separator was soaked with the PVA/LiCl solution and then dried at 60°C for 2 hours before final assembly.

3.3.5 Calculations

All the electrochemical measurements were conducted using electrochemical stations (BioLogic EC-Lab SP-300 and VMP-3e). The gravimetric capacitance (C_G, F g^{-1}), areal capacitance (C_A, m F cm^{-2}), and volumetric capacitance (C_V, m F cm^{-3}) were calculated based on the galvanostatic charging and discharging (GCD) curves using Eq. 1, 2, and 3, respectively.

$$C_G = \frac{I \times t}{\Delta U \times m} \quad \text{(Eq. 3.1)}$$

$$C_A = \frac{I \times t}{\Delta U \times A} \quad \text{(Eq. 3.2)}$$

$$C_V = \frac{I \times t}{\Delta U \times V} \quad \text{(Eq. 3.3)}$$

where I *is* the current (mA), t is the discharge time (s), ΔU is the potential window excluding the iR drop, m is the mass (mg), A is the geometric electrode working area

(cm^2), and V is the volume of the electrodes (cm^3). For the symmetric device, m and V are the total mass and volume of the two electrodes, respectively.

The volumetric energy density (E, Wh L^{-1}) and power density (P, W L^{-1}) of the symmetric supercapacitor device are calculated using the following equations:

$$E_V = \frac{C_V \Delta U^2}{2 \times 3600} \quad \text{(Eq.3.4)}$$

$$P_V = \frac{E_V \times 3600}{t} \quad \text{(Eq. 3.5)}$$

where C_V is the volumetric capacitance (mF cm^{-3}), ΔU is the potential window excluding the iR drop, and t is the discharge time (s) obtained from the GCD curve.

3.4 Results and Discussion

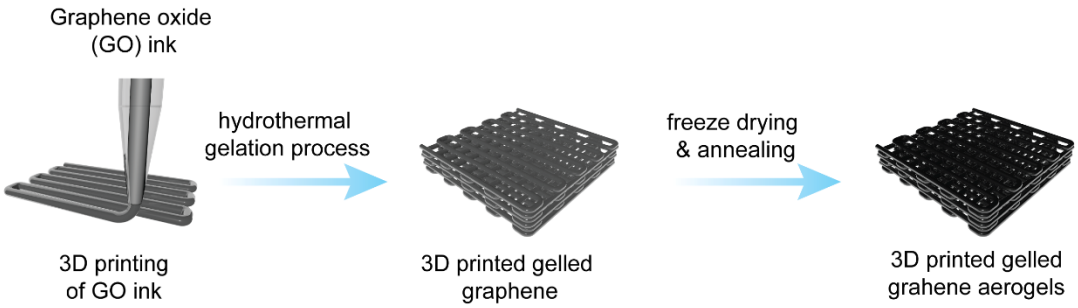


Figure 3.1. Schematic illustration of fabrication of 3D printed gelled graphene aerogel.

Figure 3.1 illustrates the fabrication process of the 3D printed gelled graphene aerogel (3D gelled GA). The 3D gelled GA was fabricated via direct ink writing method using an ink containing a mixture of graphene oxide (GO) suspension (40 mg/mL), ___% hydroxypropyl methylcellulose, Pluronic (F127), and $(NH_4)_2CO_3$. The 3D printed lattice structures were constructed by a simple cubic lattice with multiple

orthogonal layers of parallel cylindrical rod ligaments similar to the conventional 3D graphene aerogel reported eleswhere.[13] The diameter of the cylindrical rods is determined by the nozzle size of 200 μm and the center-to-center rod spacing is set to be 400 μm The 3D printed lattices were cured in sealed glass vials at 80°C for 48 hours. After gelation, the samples were washed with water to remove impurities and freeze-dried for 48 hours. This was followed by annealing in nitrogen gas at 1050°C for 3 hours to convert the GO to conductive graphene.

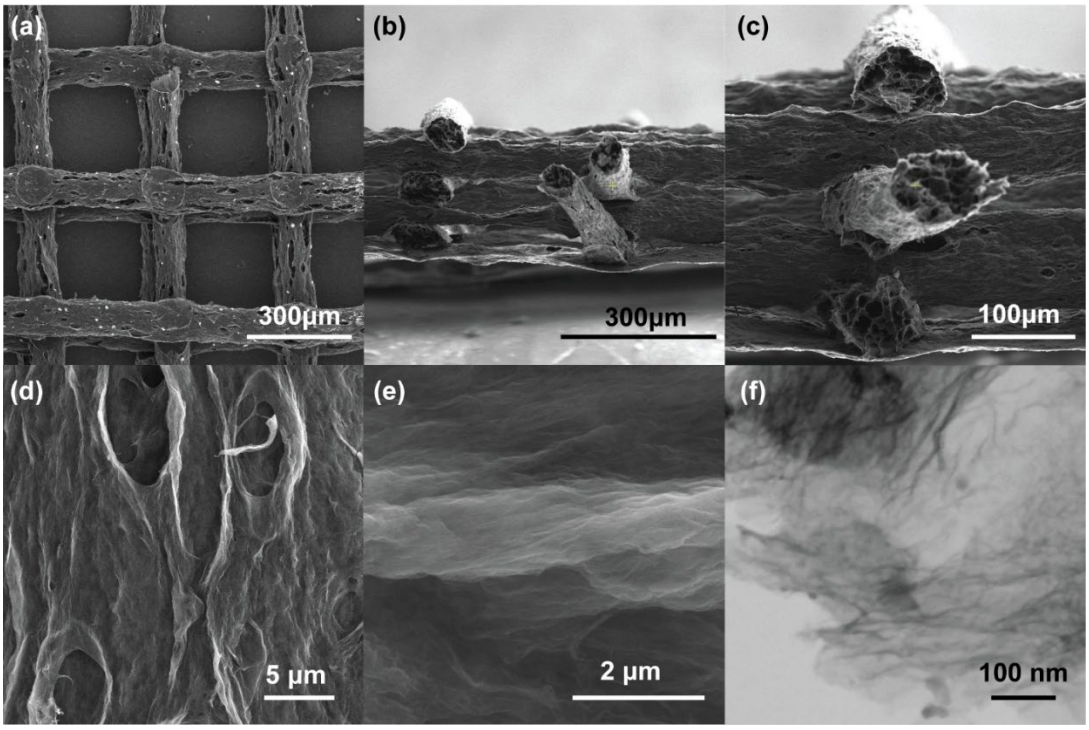


Figure 3.2. Top-view (a) and cross-sectional SEM images (b,c) of 3D gelled GA. (d,e) Higher magnification reveals the ligament surface of 3D gelled GA. (f) STEM image of 3D gelled GA's graphene sheets.

Top-view and cross-sectional SEM images were obtained from the 3D gelled GA which shows pore channels in the layer-by-layer woodpile structure (**Figure 3.2)**. The diameter of the cylindrical rod of 3D gelled GA is around 100 μm. Surprisingly, the center-to-center rod distance did not change significantly compared to the ligament size (**Figure 3.2a**). The cross-sectional SEM images revealed that 3D gelled GA contain pores (**Figure 3.2b, c**). Notably, the top-view SEM images obtained showed that the surface of the 3D gelled GA's ligament contains minimal porosity (**Figure 3.2d**). This could be attributed to the gelation process that crosse-linked the graphene oxide sheets. **Figure 3.2e** shows the interconnected graphene sheets results from the gelation process. Image from the secondary transmission electron microscopy (STEM) revealed a wrinkled paper-like texture to the sheets (**Figure 3.2f**).

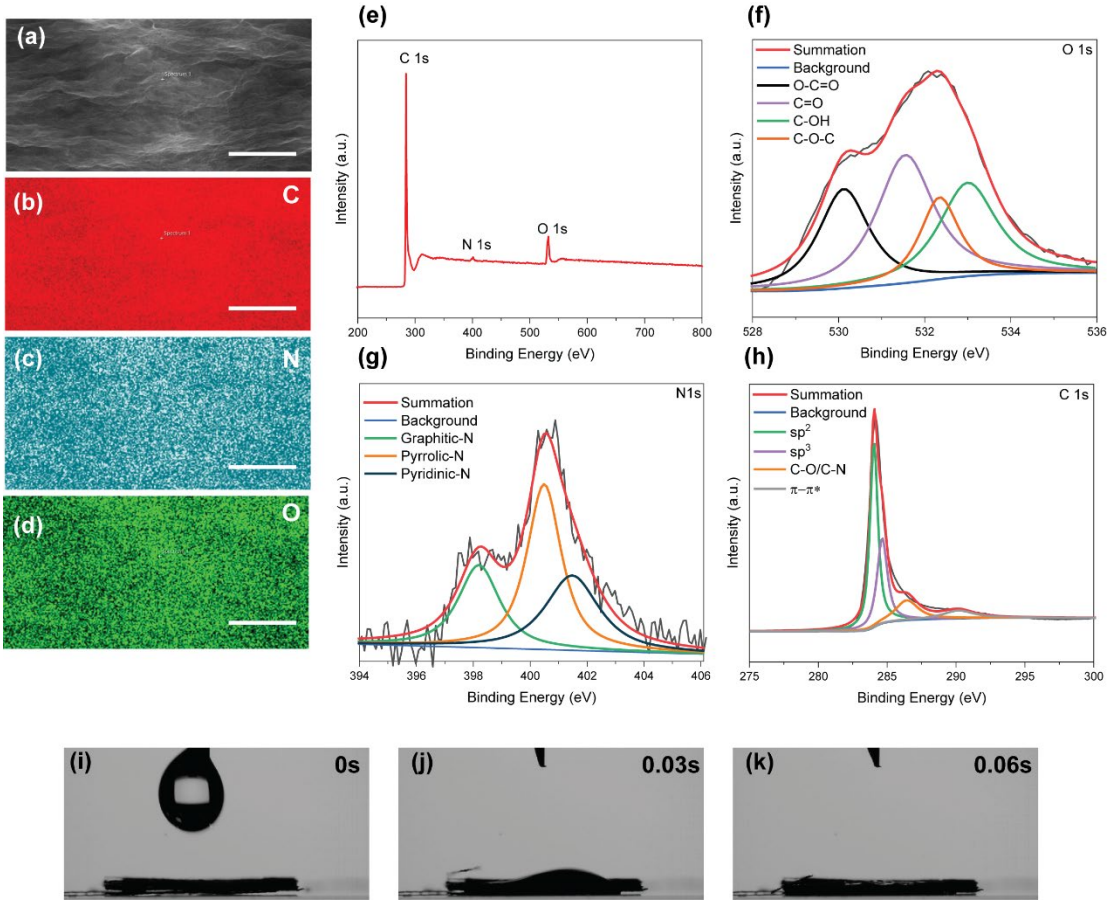


Figure 3.3. (a) SEM image of the surface of 3D gelled GA and its corresponding (b-d) EDS elemental mapping images. (e) XPS survey spectra of 3D gelled GA. Core level (f) O 1s, (g) N 1s, and (h) C 1s XPS spectra of the 3D gelled GA. (i-k) Digital images illustrating the dynamic contact angle test of 3D gelled GA.

Energy dispersive spectroscopy (EDS) elemental mapping analysis suggests that 3D gelled GA contains C, O, and N elements (**Figure 3.3a-d**). Furthermore, the chemical composition of 3D gelled GA was analyzed with X-ray photoelectron spectroscopy (XPS) (**Figure 3.3e-h**). XPS survey spectra revealed that 3D gelled GA is composed of C, O, and N (**Figure 3.3e**). 3D gelled GA has a broad O 1s peak, which

can be deconvoluted into peaks corresponding to O-C=O at 530.1 eV, C=O at 531.6 eV, C-OH at 532.4 eV, and C-O-C at 533.4 eV (**Figure 3.3f**).[18] The N 1s core peak was deconvoluted into three synthetic peaks: graphitic-N at 401.3 eV, pyrrolic-N at 400.2 eV, and pyridinic-N at 398.2 eV.[19–22] Oxygen and nitrogen moieties are critical towards the wettability of 3D gelled GA. Contact angle measurement shows that 3D gelled GA surface is super hydrophilic (**Figure 3.3i-k**). Meanwhile, the reported contact angle for 3D GA is 140°.[4]

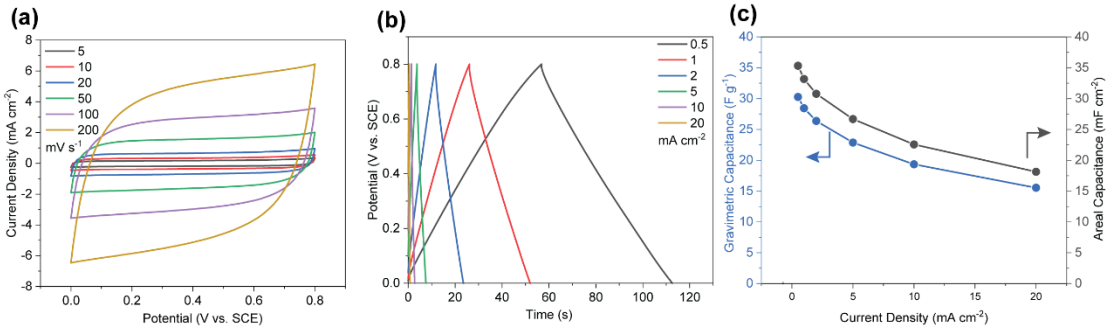


Figure 3.4. (a) Cyclic voltammetry (CV) and (b) galvanostatic charging and discharging (GCD) curves of 3D gelled GA collected in three-electrode configuration. (c) Gravimetric (blue) and areal (black) capacitance of the 3D gelled GA electrode

The electrochemical performance of 3D gelled GA was first studied in a three-electrode cell using a 3M LiCl solution as the electrolytes, and carbon rod and SCE as the counter and reference electrodes, respectively (**Figure 3.4**). Compared to 1mm thick 3D GA reported elsewhere, 3D gelled GA has a highly rectangular shape of CV and isosceles triangular galvanostatic charging discharging (GCD) profiles, suggesting the electron transport and ion diffusion are highly efficient (**Figure 3.4a, b**).[13]

Generally, areal capacitance of highly porous electrode linearly increases with electrode thickness due to the great ion accessibility.[4,13] The 3D gelled GA which thickness of 300 μm achieved a high areal capacitance of 39.7 mF cm^{-2} at 0.5 mA cm^{-2}, which is twice as high as the freeze-dried 3D GA with thickness of 1 mm at the same current density (**Figure 3.4c**)[13]. In addition, the gravimetric capacitance of the 3D gelled GA (35.7 F g^{-1}) is 8-fold higher than the gravimetric capacitance of 3D GA (4.5 F g^{-1}) at the same current density of 0.5 mA cm^{-2}.[13] The substantial enhanced capacitance of 3D gelled GA is likely due to the increased contribution of pseudocapacitance from the surface functional groups participate in redox reaction. Furthermore, owing to the microstructure features of 3D gelled GA, it retained 70% and 60% of its initial capacitance at the current density of 10 and 20 mA cm^{-2}, respectively. The electrochemically active surface area (ECSA) of the 3D gelled GA was measured on basis of its double layer capacitance in a narrow voltage window (Figure x). By linearly fitting the current with the scan rate, electrical double layer capacitance was determined through the obtained slope. The calculated ECSA of 3D gelled GA (654.1 cm^{-2}) was found to be higher than the reported 3D GA (374.8 cm^{-2}).[13] This indicates that the intrinsic functional groups of 3D gelled increases its active surface area which contributed to electrode's higher capacitance than the 3D GA.

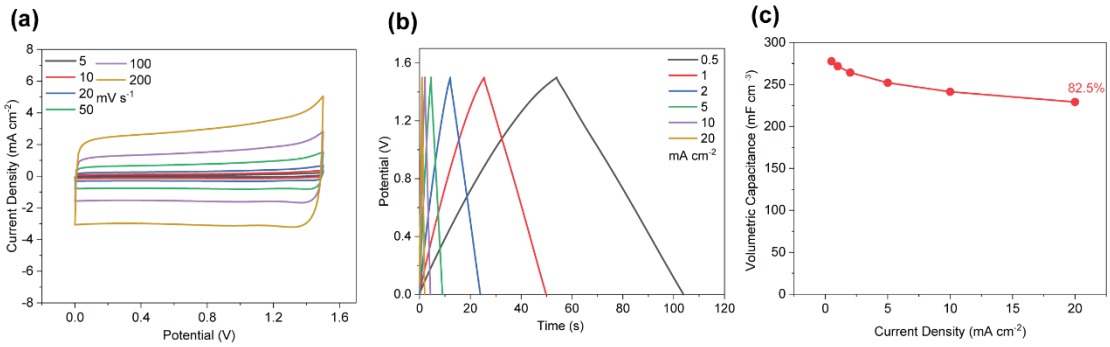


Figure 3.5. (a) Cyclic voltammetry (CV) and (b) galvanostatic charging and discharging (GCD) curves of symmetric aqueous device. (c) Calculated volumetric capacitance of the symmetric aqueous device.

We tested the feasibility of 3D gelled GA as the electrode for a device by assembling a symmetric aqueous supercapacitor. The device was fabricated with a Kapton tape-based pouch cell by assembling two 300 µm thick 3D gelled GA electrodes with 7.86M LiCl electrolyte. The 3D gelled GA symmetric device achieved a stable working voltage of 1.5V. The quasi-rectangular cyclic voltammograms and symmetric triangular GCD curves suggest that the device has an excellent capacitive behavior (**Figure 3.5a, b**). Calculated from the GCD curves, the device achieved a maximum volumetric capacitance of 277.6 mF cm^{-3} at 0.5 mA cm^{-2} (**Figure 3.5c**). The symmetric device retained 82.5% of its initial capacitance at high current density of 20 mA cm^{-2}.

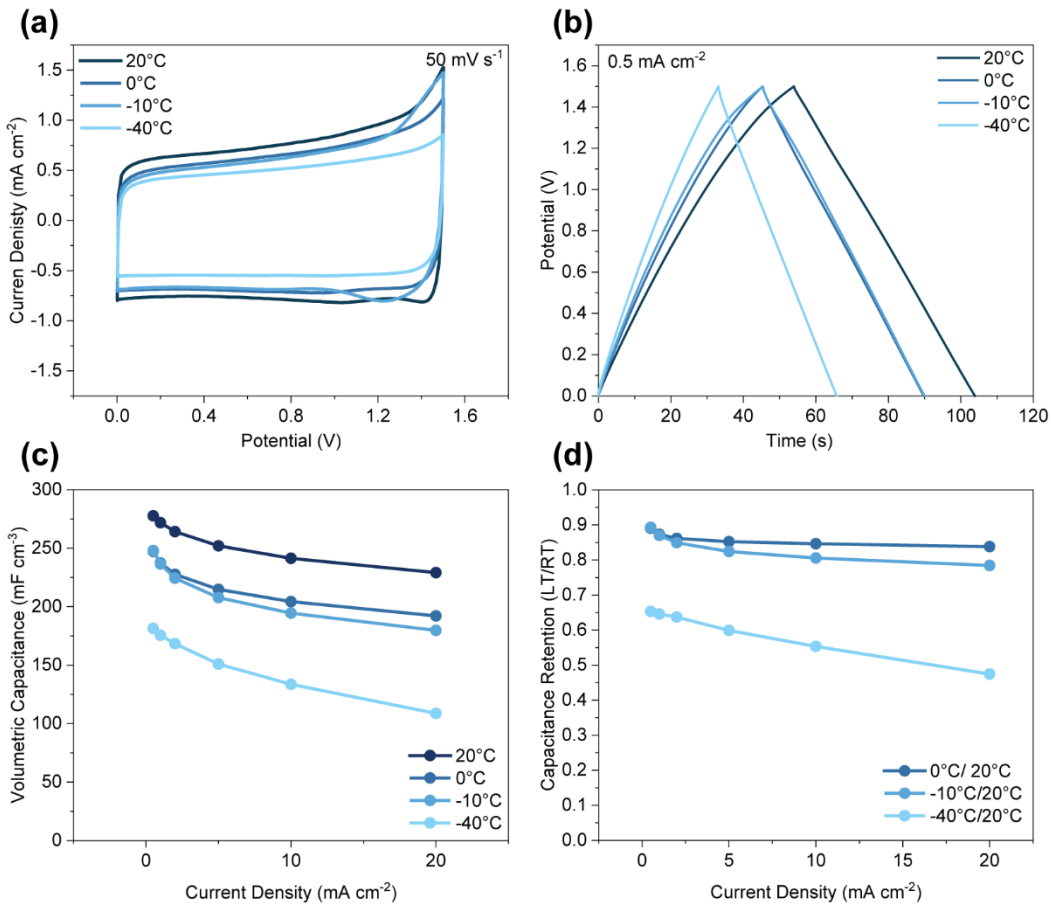


Figure 3.6. (a) CV and (b) GCD curves of symmetric aqueous device at 20, 0, -10, and -40 °C. (c) Calculated volumetric capacitance of the symmetric aqueous device at different temperatures. (d) is the capacitance retention at 0, -10, and -40°C with respect to its room temperature capacitance.

We further investigate the feasibility of the electrode under different operating temperatures. Previous studies have showed that increasing the porosity of carbon electrode enhances the ion and charge transports which are the limiting factors that deteriorate the performance at low operating temperatures.[23–25] Introducing heteroatom have also shown to boost the capacitance of the electrode by increasing its electrode-

electrolyte interaction and can participate in the redox reaction, providing additional pseudocapacitance.[26] The electrochemical performance of the 3D gelled GA symmetric supercapacitor was further investigated at low temperatures. It is worth noting that the high solubility of lithium chloride in water greatly depressed the freezing point at eutectic point (7.86M LiCl) which makes it suitable for low temperature application.[27] Symmetric supercapacitor device with 3D gelled GA was evaluated at 0, -10, and -40°C. As expected, the performance of the aqueous symmetric device at decreases as the temperature decreased. **Figure 3.6a, b** shows that even at low temperatures, the device retained highly rectangular shape of CV and isosceles triangular GCD profile, suggesting that even at low operating temperature of -40°C electron transport and ion diffusion are highly efficient. At 0 and -10°C, aqueous symmetric device achieved comparable volumetric capacitance of 247 mF cm^{-3} at low current density of 0.5 mA cm^{-2} due to the close temperature difference (**Figure 3.6c**). At 20 mA cm^{-2}, the device achieved volumetric capacitance of 192.1 and 179.7 mF cm^{-3}. Capacitance retention ratio of the device at 0 and -10 °C were calculated (**Figure 3.6d**). Even at high current density of 20 mA cm^{-2}, the device retained a capacitance retention ratio of 0.84 and 0.78 at 0 and-10°C, respectively. We further evaluated the electrochemical performance of 3D gelled GA at -40°C. At 0.5 mA cm^{-2}, the device achieved 181.4 mF cm^{-3} which is 65% of its room temperature capacitance under the same current density. At high charge-discharge rate of 20 mA cm^{-2}, the device achieved 108.7 mF cm^{-3} and retained a capacitance retention ratio of 0.47 with respect to its room temperature performance. This shows that the synergic effect of engineered porous structure and unique intrinsic

properties of the 3D gelled GA electrode enhanced the performance of carbon-based aqueous SC even at low operating temperatures.

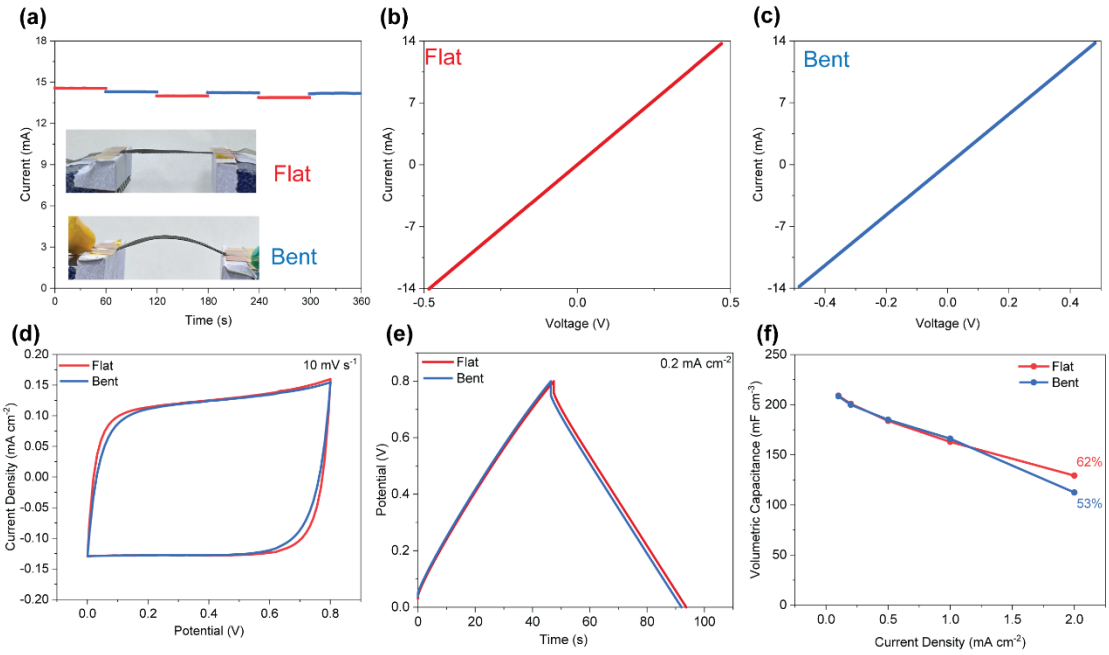


Figure 3.7. Current-time curves of 3D gelled GA at alternating bending condition. The insets are the digital images if the 3D gelled GA at the two bending states. Current-voltage curve of 3D gelled GA without (b) and with (c) bending. (d) CV and (e) GCD curves of symmetric solid-state with and without bending. Calculated volumetric capacitance of the symmetric solid-state SC device with and without bending collected at the current density of 0.1-2 mA cm^{-2}.

One of the major drawbacks of 3D printed GA fabricated via freeze drying is its mechanical properties. Ice-templated graphene-based electrodes normally suffer from poor mechanical structure due to their high porosity and weak graphene sheets interaction.[28,29] The graphene oxide sheets of 3D gelled GA was directly cross-linked

through hydrothermal gelation process under mild basic conditions. The inherent oxygen functional groups of graphene oxide sheets serve as chemical cross-linking sites. Upon thermal reduction, these cross-links are transformed into conductive carbon bridges and provide structural support and thus enhanced the mechanical integrity of the electrode.[30] To evaluate the mechanical properties electrode, we investigated the flexibility and compressibility of the 3D gelled GA. We first assessed the flexibility of the 3D gelled GA. It was found that 3D gelled GA was able to achieve a bending angle of 60°. Meanwhile, bending the 3D GA at the same angel would completely break the 3D printed ligaments and its overall structure. We evaluated conductance stability of the 3D gelled GA by monitoring the current at a fixed voltage of 0.5V. **Figure 3.7a-c** shows that the conductance of the 3D gelled GA is hardly affected after alternating the bending states. It can be observed that the current was nearly unchanged after alternating bending, revealing that the conductance of 3D gelled GA is hardly affected by the bending stress. Moreover, the results shows that the cross linking the graphene oxide sheets increase added flexibility to the 3D printed carbon aerogel. To evaluate the feasibility of the 3D gelled GA for flexible energy storage device, a symmetric solid-state supercapacitor was fabricated with LiCl/PVA electrolyte (**Figure 3.7d-f)**. **Figure 3.7d** shows that CV curves collected at 5 mV s^{-1} did not significantly change between the two bending states. The GCD curve at current density of 0.2 mA cm^{-2} at both bending states also shares the same behavior (**Figure 3.7e**). Volumetric capacitance of the solid-state supercapacitor was calculated from GDC curves collected at the current density of 0.1-2 mA cm^{-2}. **Figure 3.7f** shows that at the low current

density the device's volumetric capacitance is comparable at both bending states. However, at the current density of 2 mA cm^{-2} the performance of the device at the bent state is lower than the flat state. The results demonstrate that 3D gelled could withstand mechanical stress from bending.

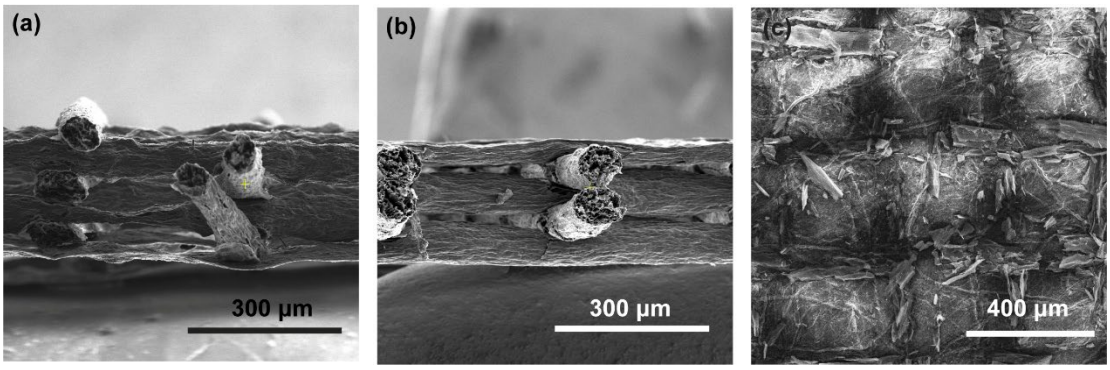


Figure 3.8. Cross section SEM images of the 3D gelled GA at the (a) initial state and after applying (b) 0.4 MPa. (c) Top-view SEM image of the 3D gelled GA compressed on the separator at the pressure above 1.0 MPa.

Another factor that determines the mechanical integrity of the electrode is its compressibility. During device manufacturing, external pressure typically applied to ensure good electrical contact between the electrodes and the current collectors.[31,32] Excessive applied pressure can induce internal deformation of electrode structure, leading to pore collapse and increased internal resistance, which degrades its electrochemical performance.[31,33] The electrochemical performance of symmetric 3D gelled GA under different applied pressures was conducted using the pressure controlled split coin cell. Notably, 3M KOH was used as electrolyte instead of LiCl to prevent the current collector corrosion. Using the pressured controlled split coin cell,

the electrochemical performance of the symmetric device with 3D gelled GA electrodes was evaluated under different pressure applied. Assuming that the no frictional force from the split cell, the device was tested under an applied pressure ranging from 0.2 to 1.0 MPa. The maximum pressure the thin 3D gelled AG can tolerate is 1.0 MPa (**Figure 3.8**). Beyond that pressure, the electrode's structure completely collapses. The device's electrochemical performance was also tested without external pressure (0 MPa). Figure 9 shows the SEM images of 3D gelled GA tested at different applies pressure. At initial state, the 3D gelled GA has a thickness of ~ 300 µm. After tested under the applied pressure around 0.4 MPa, some of the ligaments compressed giving the total thickness of 240 µm. At 1.0 MPa, the samples completely compressed into the separator.

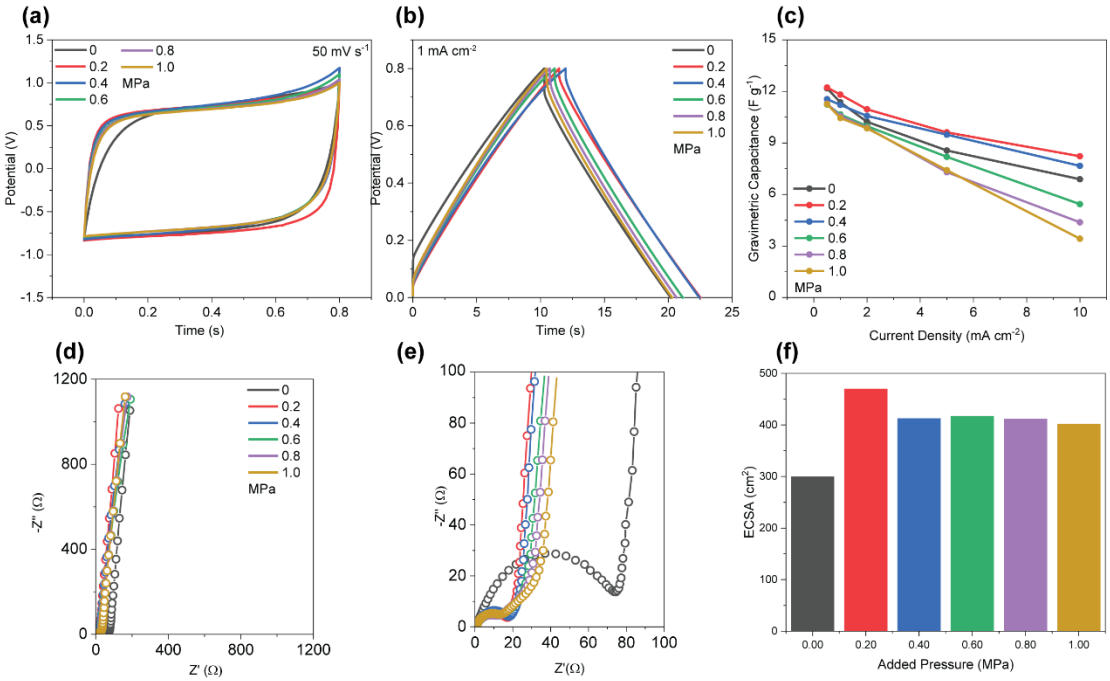


Figure 3.9. (a) CV curves collected at the scan rate of 50 mV s^{-1} and (b) GCD curves collected at 1 mA cm^{-2} of 3D gelled GA symmetric device under different

applied pressure. (c) Gravimetric capacitance of the 3D gelled GA device at the current density of 0.5 to 10 mA cm^{-2}. (d) Nyquist plot of 3D gelled GA symmetric device. (e) Nyquist plot of 3D gelled GA symmetric device highlighting high and intermediate-frequency region). (f) Calculated electrochemical surface area of 3D gelled GA device under different applied pressure.

Figure 3.9 a. show's the CV curves of symmetric SC at a scan rate of 50 mV s^{-1} under different compressive stress. All CV curves of the device with different applied pressure show an excellent quasi-rectangular shape at high scan rate of 50 mV s^{-1}. GCD curve at 1 mA cm^{-2} shows an increased and then decrease in charging-discharging time of the symmetric SC under different applied pressure (**Figure 3.9 b**). The capacitance of the 3D gelled GA device was calculated from GCD curve collected at the current density of 0.5-10 mA cm^{-2}. **Figure 3.9 c** shows that device performance increased at an applied pressure of 0.2MPa but declined with further increases in pressure. At initial state (0MPa), the device achieved a high capacitance of 14.73 F g^{-1} (12.18 mF cm^{-2}) at the current density of 0.5 mA cm^{-2}, retaining 57% of its initial capacitance at 10 mA cm^{-2}. Upon the application of 0.2MPa pressure, the capacitance increased to 14.79 F g^{-1} (12.23 mF cm^{-2}) and achieved higher retention rate of 67% at 10 mA cm^{-2} with respect to its initial capacitance at 0.5 mA cm^{-2}. This is due to the enhancement of the contact between the electrodes and the current collector. As the applied pressure continues to increase from 0.4 to 1.0MPa, capacitance slightly decreased as well as its rate capability at 10 mA cm^{-2} due to reduction of pores which allows sufficient ion diffusion. The resistance 3D gelled Ga under different applied pressure were compared

via the electrochemical impedance spectroscopy (EIS) analysis (**Figure 3.9d, e**). EIS studies reveal that as the applied pressure increases, the charge transfer resistance decreases. Furthermore, in the low frequency region, the 3D gelled GA SC demonstrate notably steep slopes when lower applied pressure, indicating the charging process was not diffusion limited.[34] However, the nonvertical line at the intermediate frequency emerged as the pressure applied increased to 1.0 MPa. The existence of the nonvertical line at intermediate frequency indicates ion transport limitation.[34,35] This again shows the importance of the porosity for high performing energy storage device. Electrochemical surface area was calculated from the CV curves collected at narrow potential of 0.4 to 0.5V. EDLCs (C_{EDLC}) of the devices were determined by linearly fitting the anodic current densities at 0.45 V against scan rates 1 to 5 mV s^{-1}. Figure 10f shows the histogram of the calculated ECSA of the device collected at different applied pressure. At applied pressure of 0.2 MPa, the device achieved an ECSA of 469.6 cm^2. As the applied pressure increased from 0.4MPa to 1.0MPa, the ECSA decreased, and the values became comparable. These results suggest that, despite the collapse of the 3D printed structure, the thin 3D gelled GA electrode was able to deliver sufficient capacitance, making it a promising candidate for high performance thin electrode.

3.5 Conclusion

In summary, we developed a new graphene oxide-based ink for thin, freestanding, highly conductive, and mechanically robust electrodes. The 3D printed graphene with $(NH_3)_2CO_3$ additive was converted to 3D gelled graphene aerogel which successfully maintained its structure after high temperature post-processing and

exhibited enhanced mechanical integrity. The physical cross-linking of the graphene sheets via the gelation process allows the graphene aerogels to withstand sufficient mechanical stress caused by bending and compression compared to freeze-dried counterparts. Even at banding angle of 60°, the 3D gelled GA shows excellent conductance stability. Furthermore, the 3D gelled GA is also composed of oxygen and nitrogen functional groups which boost its capacitance even at low operating temperature. Even at extremely low temperatures of -40°C, 3D gelled GA symmetric device retained 65% of its room temperature capacitance. Thus, the synergistic effect of the engineered porous structure and unique intrinsic properties of the 3D gelled GA electrode would make it a promising candidate for high performance thin electrode.

3.6 References

1. Zhu, C. *et al.* Supercapacitors Based on Three-Dimensional Hierarchical Graphene Aerogels with Periodic Macropores. *Nano Lett.* **16**, 3448–3456 (2016).
2. Son, J., Kim, H., Choi, Y. & Lee, H. 3D printed energy devices: generation, conversion, and storage. *Microsyst Nanoeng* **10**, 93 (2024).
3. Cross, N. R. *et al.* Viability of Additively Manufactured Electrodes for Lithium-Ion Batteries. *ACS Appl. Eng. Mater.* **3**, 214–224 (2025).
4. Yao, B. *et al.* 3D-Printed Structure Boosts the Kinetics and Intrinsic Capacitance of Pseudocapacitive Graphene Aerogels. *Advanced Materials* **32**, 1906652 (2020).
5. Lin, T. Y. *et al.* Shape Matters: Understanding the Effect of Electrode Geometry on Cell Resistance and Chemo-Mechanical Stress. *J. Electrochem. Soc.* **171**, 100515 (2024).
6. Camposeo, A., Persano, L., Farsari, M. & Pisignano, D. Additive Manufacturing: Applications and Directions in Photonics and Optoelectronics. *Advanced Optical Materials* **7**, 1800419 (2019).
7. Chandrasekaran, S., Lin, D., Li, Y. & Worsley, M. A. Aerogels, additive manufacturing, and energy storage. *Joule* **7**, 866–883 (2023).
8. Zhang, F. *et al.* 3D printing technologies for electrochemical energy storage. *Nano Energy* **40**, 418–431 (2017).
9. Pekala, R. W. & Alviso, C. T. Carbon Aerogels and Xerogels. *MRS Online Proceedings Library* **270**, 3–14 (1992).

10. Chandrasekaran, S. *et al.* Direct ink writing of organic and carbon aerogels. *Mater. Horiz.* **5**, 1166–1175 (2018).
11. Zhou, B. *et al.* Controlling surface porosity of graphene-based printed aerogels. *npj 2D Mater Appl* **6**, 34 (2022).
12. Kim, G. W. *et al.* Additive-Free Gelation of Graphene Oxide Dispersions via Mild Thermal Annealing: Implications for 3D Printing and Supercapacitor Applications. *Advanced Materials* **36**, 2411479 (2024).
13. Yao, B. *et al.* Efficient 3D Printed Pseudocapacitive Electrodes with Ultrahigh MnO2 Loading. *Joule* **3**, 459–470 (2019).
14. Yun, X. *et al.* Direct 3D printing of a graphene oxide hydrogel for fabrication of a high areal specific capacitance microsupercapacitor. *RSC Advances* **9**, 29384–29395 (2019).
15. Qi, Z. *et al.* 3D-Printed, Superelastic Polypyrrole–Graphene Electrodes with Ultrahigh Areal Capacitance for Electrochemical Energy Storage. *Advanced Materials Technologies* **3**, 1800053 (2018).
16. Zhu, C. *et al.* Highly compressible 3D periodic graphene aerogel microlattices. *Nat Commun* **6**, 6962 (2015).
17. Worsley, M. A. *et al.* High Surface Area, sp2-Cross-Linked Three-Dimensional Graphene Monoliths. *J. Phys. Chem. Lett.* **2**, 921–925 (2011).
18. Al-Gaashani, R., Najjar, A., Zakaria, Y., Mansour, S. & Atieh, M. A. XPS and structural studies of high quality graphene oxide and reduced graphene oxide

prepared by different chemical oxidation methods. *Ceramics International* **45**, 14439–14448 (2019).

19. Liu, T. *et al.* Tuning the Electrochemical Properties of Nitrogen-Doped Carbon Aerogels in a Blend of Ammonia and Nitrogen Gases. *ACS Appl. Energy Mater.* **1**, 5043–5053 (2018).
20. Long, D. *et al.* Preparation of Nitrogen-Doped Graphene Sheets by a Combined Chemical and Hydrothermal Reduction of Graphene Oxide. *Langmuir* **26**, 16096–16102 (2010).
21. Sun, L. *et al.* Nitrogen-doped graphene with high nitrogen level via a one-step hydrothermal reaction of graphene oxide with urea for superior capacitive energy storage. *RSC Adv.* **2**, 4498–4506 (2012).
22. Chen, P. *et al.* Hydrothermal Synthesis of Macroscopic Nitrogen-Doped Graphene Hydrogels for Ultrafast Supercapacitor. *Nano Energy* **2**, 249 (2013).
23. Yao, B. *et al.* Printing Porous Carbon Aerogels for Low Temperature Supercapacitors. *Nano Lett.* **21**, 3731–3737 (2021).
24. Zhang, M. *et al.* An Ultrafast and Ultralow-Temperature 3D-Printed All-Organic Proton Pseudocapacitor. *Advanced Functional Materials* **35**, 2413436 (2025).
25. Zhang, M. *et al.* 3D-printed redox-active polymer electrode with high-mass loading for ultra-low temperature proton pseudocapacitor. *Advanced Powder Materials* **4**, 100247 (2025).
26. Liang, S. *et al.* Nitrogen-doped graphene/carbon nanotube hydrogel for high-performance, low-temperature supercapacitor. *Ionics* **31**, 6191–6203 (2025).

27. Viola, W. & Andrew, T. L. An Aqueous Eutectic Electrolyte for Low-Cost, Safe Energy Storage with an Operational Temperature Range of 150 °C, from −70 to 80 °C. *J. Phys. Chem. C* **125**, 246–251 (2021).
28. Zhu, P., Slater, P. R. & Kendrick, E. Insights into architecture, design and manufacture of electrodes for lithium-ion batteries. *Materials & Design* **223**, 111208 (2022).
29. Xu, X. *et al.* Highly crumpled graphene-like material as compression-resistant electrode material for high energy-power density supercapacitor. *Chemical Engineering Journal* **397**, 125525 (2020).
30. A. Worsley, M. *et al.* Mechanically robust 3D graphene macroassembly with high surface area. (2012) doi:10.1039/C2CC33979J.
31. Wang, H. *et al.* Internal pressure regulation enables reliable electrochemical performance evaluation of lithium-ion full coin cell. *Journal of Power Sources* **600**, 234235 (2024).
32. Li, R. *et al.* Effect of external pressure and internal stress on battery performance and lifespan. *Energy Storage Materials* **52**, 395–429 (2022).
33. Zeng, L. *et al.* Direct Ink Writing 3D Printing for High-Performance Electrochemical Energy Storage Devices: A Minireview. *Adv Sci (Weinh)* **10**, 2303716 (2023).
34. Mei, B.-A. *et al.* Physical Interpretations of Electrochemical Impedance Spectroscopy of Redox Active Electrodes for Electrical Energy Storage. *J. Phys. Chem. C* **122**, 24499–24511 (2018).

35. Liu, C.-L. *et al.* Influence of KOH followed by oxidation pretreatment on the electrochemical performance of phenolic based activated carbon fibers. *Journal of Electroanalytical Chemistry* **611**, 225–231 (2007).

Chapter 4

Electrochemical Behavior of Electrodeposited γ- and ε- Manganese dioxide in Aqueous and Non-aqueous Systems

4.1 Abstract

Manganese dioxide (MnO_2) has received great attention in the past few years due to low cost, environmental friendliness, and high theoretical specific capacity. One of the unique features of MnO_2 is its diverse crystallographic structures, which allow tuning of the material's electronic and ionic conductivity. Electrodeposition allows faster and controllable synthesis of MnO_2. Although ε-MnO_2 has high capacity, its low electrical conductivity and highly disordered crystal structure, making it the least favorable for electrochemical reaction. Other crystal phases of MnO_2 such as γ-MnO_2 that have higher electrical conductivity and more ordered channel structures that can better facilitate electron and ion transport are more desirable. Here, we explored the influence of the crystal structure on the electrochemical performance of electrodeposited MnO_2 in aqueous and non-aqueous system. Overall, each phase of MnO_2 has its own advantages and disadvantages depending on operating system. The findings from this study open avenues for understanding the complex charge storage mechanisms of MnO_2 polymorphs and other metal oxide-based materials.

4.2 Introduction

The demand for energy storge devices with high energy density and fast charging and discharging has driven the development of pseudocapacitors, which store energy through faradaic charge transfer (redox) mechanism.[1–4] Among the pseudocapacitive materials, manganese dioxide (MnO_2) has received great attention in the past few years due to low cost, environmental friendliness, and high theoretical specific capacity of 308 mAh g^{-1} for one-electron transfer.[5–8] In addition, MnO_2 is also widely used in different battery systems, such as Mn-Zn, Mn-Li, and Mn-Na, making it one of the variable material for energy storage [9–12] One of the unique features of MnO_2 is its diverse crystallographic structures, which allow tuning of the material's electronic and ionic conductivity. The formation of these phases depends on specific growth conditions, and each phase exhibits unique electronic and electrochemical properties.[13]

Previous studies have shown that the primary phase of electrochemically deposited MnO_2 in aqueous electrolytes is ε-phase.[13] Based on the theoretical calculation of Sun et al, ε-phase has the highest volumetric capacity among the MnO_2.[14] The ε phase of MnO_2 adopts a NiAs-type lattice structure with Mn^{4+} and vacancies randomly occupying 50% of all available octahedral sites.[15] However, due to its low electrical conductivity and highly disordered crystal structure, making ε-MnO_2 the least favorable for electrochemical reaction.[13,14] In contrast, tunnel phases such as γ-phase can mitigate volume expansion during lithiation of ions. The phase of MnO_2 can be controlled by adjusting the deposition temperature as stated in the previous study

elsewhere.[13] Increasing the deposition temperature of the acidic electrolyte 0from 20°C to above 90°C leads to the formation of γ-MnO_2 which has 2x1 and 1x1 tunnel structure domains. The crystal structure of the γ-MnO2 is between the R-MnO_2 (2x1 domain) and β-MnO_2 (1x1 domain).[16,17] This tunnel structure of the γ-MnO_2 not only can mitigate volume expansion during lithiation of ion but also demonstrated to have substantially higher electrical conductivity than ε-MnO_2, making it more favorable electrode material.[13,14]

Among the various synthesis methods of MnO_2, electrodeposition has emerged as the most desirable technique due to its short processing time, which lowers production costs.[13,18–20] Recently, enhancing the electrodes' structure attracts a lot of attention to improve the trade-ff between capacity and rate performance present in conventional planar electrode.[21] In general, the goal of electrodes with 3D structures is to reduce the distance of electron and ion transport pathways and increasing the active material loading.[21] Electrodeposition provide a versatile approach for depositing active materials onto a electrodes.[3,22–25] Recently, Yao et al. electrodeposited high mass loading of ε-MnO_2 on a 3D printed porous carbon aerogels without sacrificing their gravimetric and volumetric capacitive performance due to sluggish ion diffusion in bulk material.[3] Xue et al. also utilize electrodeposition to incorporate active materials onto an electrode with complex design.[24] These studies demonstrated how electrodeposition offers great flexibility in both structural design and material selections, ultimately enabling the achievement of high-performance energy storage.

Depending on the crystal structure, electrolyte, and electrochemical conditions, MnO_2 stores charge through mechanisms like surface ion adsorption, ion intercalation/deintercalation, and dissolution/deposition. Here, we explored the influence of the crystal structure on the electrochemical performance of electrodeposited MnO_2 polymorphs in aqueous and non-aqueous system. In aqueous system, the ε-MnO_2 was found to have higher capacitance than the γ-phase. This is due to the defects on the ε-MnO_2 structure which boost reaction kinetics. However, the opposite results were found in non-aqueous system. The γ-phase achieved higher capacity than that of ε-phase due to the tunnels that enhanced the mobility of the ions. The difference in the trend shows the advantages and disadvantages of both polymorphs in different systems. This work opens new avenues for understanding the complex charge storage mechanisms of MnO_2 polymorphs and other metal oxide-based materials.

4.3 Experimental

4.3.1 Electrodeposition

γ-MnO_2 nanocrystals were electrodeposited on the carbon cloth (CC) electrode at 90°C under a constant current density of 40 mA cm^{-2} using 1M manganese sulfate and 0.1M sulfuric acid mixed solution with carbon paper as the counter electrode. Before electrodeposition, the electrodes were presoaked in the electrolyte at 90°C for 30 min. to stabilize the temperature deposition. Afterwards, the CC/ γ-MnO_2 was washed with deionized water. The CC/ γ-MnO_2 underwent hydrothermal treatment, Ostwald ripening, in 25 mL Teflon-lined stainless -steel autoclave with

20 mL of water at 90°C. The sample was then dried at 65°C overnight. Similarly, ε-MnO_2 nanosheets were electrodeposited on the CC using the same electrolyte and current density, but at 20°C. After electrodeposition, the CC/ ε-MnO_2 was post-treated at 300°C for 2 hours to remove structural water.

4.3.2 Material Characterization

Surface morphology was analyzed using the field emission SEM (FEI Quanta 3D FEG dual beam). X-ray diffraction (XRD) spectra of the samples were collected at beamline 2-1 at the Stanford Radiation Lightsource (SSRL) using monochromatic X-rays with an incident wavelength of 0.729625 Å. The electrochemical performance of the MnO_2 polymorphs in the aqueous system were evaluated in a 3M LiCl aqueous electrolyte with carbon rod and saturated calomel electrode (SCE) as the counter and references electrodes, respectively. The performance of the MnO_2 polymorphs were also evaluated in non-aqueous system CR-2032-type coin cells were fabricated using Li metal as the anode and CC/MnO_2 as the cathode separated with Celgard membrane. We used 1M lithium bis(fluorosulfonyl)imide (LiFSI) in diethyl ether (DEE) as the electrolyte. All electrochemical performance were evaluated using the electrochemical stations BioLogic EC-Lab SP-300 and VMP-3e.

4.3.3 Calculations

The gravimetric capacitance ($C_{G,}$ F g^{-1}) of single electrodes was calculated based on the galvanostatic charging and discharging (GCD) curves using Eq. 1:

$$C_G = \frac{I \times t}{\Delta U \times m} \quad \text{(Eq. 4.1)}$$

where *I is* the current (mA), *t* is the discharge time (s), *ΔU* is the potential window excluding the *iR* drop, and *m* is the mass of the active material (mg).

The areal capacitance (C_A, mF cm^{-2}) of the symmetric device calculated based on the GCD curves using Eq. 2:

$$C_A = \frac{I \times t}{\Delta U \times A} \quad \text{(Eq.4.2)}$$

where *I is* the current (mA), *t* is the discharge time (s), *ΔU* is the potential window excluding the *iR* drop, *A* is the electrodeposited material (cm^2).

The gravimetric capacity (Q_G) of single electrodes was calculated in the galvanostatic charging and discharging tests using Eq.3

$$Q_G = \frac{Q_{dis}}{m} \quad \text{(Eq. 4.3)}$$

where Q_G is the gravimetric capacities (mA h g^{-1}), Q_{dis} is the discharging capacity (mA h) obtained from the galvanostatic discharging voltage profile, and *m* is the mass loading of the active material on the electrode (g).

Trasatti Capacitance Contribution Analysis

Trasatti method was utilized to quantify the capacitance contribution by the surface and bulk.[26] Areal capacitance (*C*) at different scan rates were evaluated from the cyclic voltammetry (CV) curves using Eq 5:

$$C = \frac{S_{CV}}{2v\,\Delta U} \qquad \text{(Eq.4.4)}$$

where S_{CV} is the area enclosed by the CV curve (mA V cm^{-2}), v is the scan rate (V s^{-1}), and ΔU is the working potential (V). By assuming a semi-finite ion diffusion, a linear dependence of C vs. $v^{-1/2}$ can be drawn at slow scan rates (1–5 mV s^{-1}). A linear fit was extrapolated at low scan rates and the determined the y-intercept ($v \rightarrow +\infty$) which represents the areal capacitance contributed by the surface ($C_{SURFACE}$). Since the total capacitance (C) at each scan rate was a sum of $C_{SURFACE}$ and C_{BULK}, the percentage of capacitance from surface and bulk can be calculated.

4.4 Results and Discussions

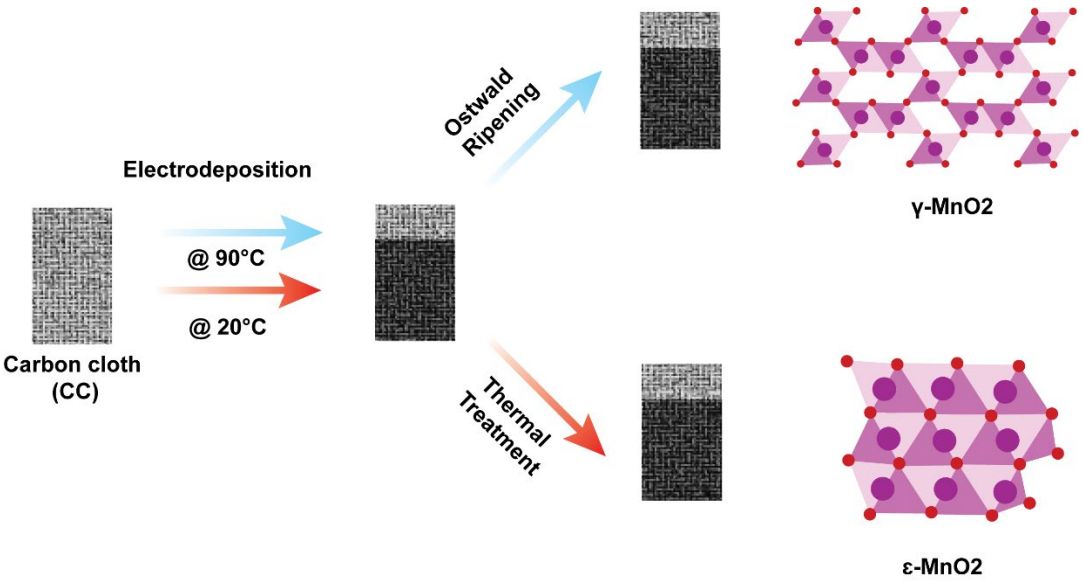


Figure 4.1. Schematic illustration of CC/γ-MnO_2 and CC/ε-MnO_2 fabrication.

The fabrication process for CC/ε-MnO_2 and CC/γ-MnO_2 electrodes is illustrated in **Figure 4.1**. The ε-MnO_2 nanosheets were deposited on CC using an acidic electrolyte

at 20°C. Meanwhile, γ-MnO_2 nanocrystals were obtained by electrodeposition at high temperature (90°C) .[13] The lattice energy between polymorphs are usually small, thus tuning the synthesis temperature could alter the phase of MnO_2.[13,27] After electrodeposition, CC/ε-MnO_2 was dried at 300°C for 2 hours to remove structural water and CC/γ-MnO_2 underwent Ostwald ripening at 90°C for 20 min. It is worth mentioning that Ostwald ripening time is dependent on the mass loading of the MnO_2.[23] The mass loading is dependent on the deposition time. After 4 min of deposition, both samples achieved a mass loading of 3 mg cm^{-2}.

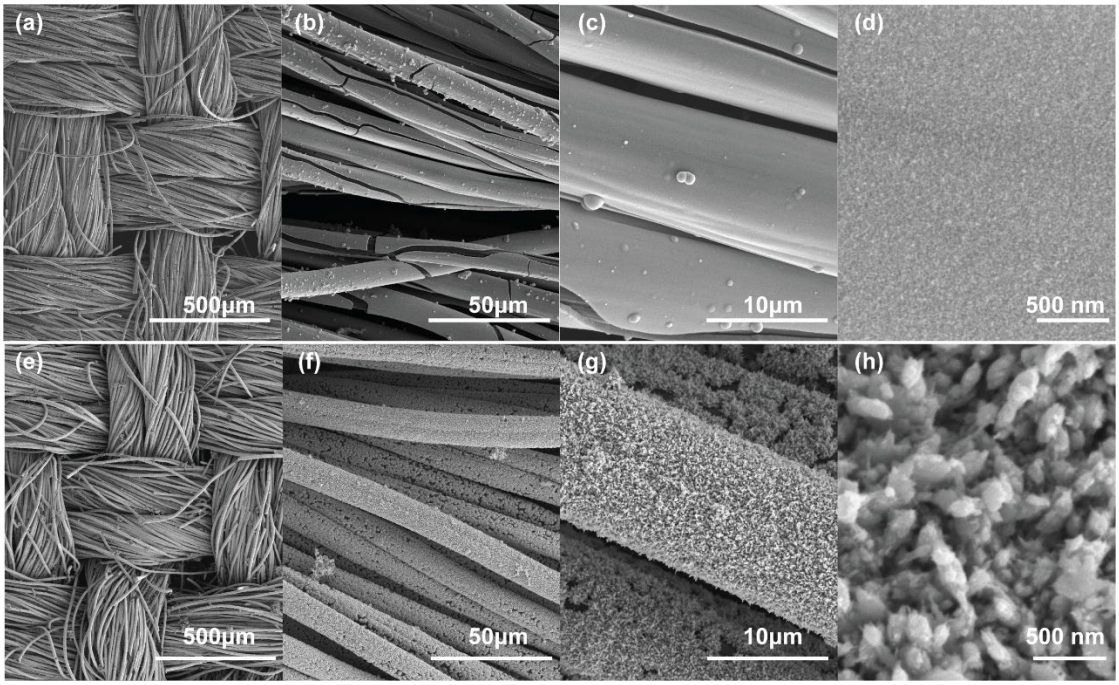


Figure 4.2. Top-view SEM images of (a-d) CC/ε-MnO_2 and (e-h) CC/γ-MnO_2 at different magnification.

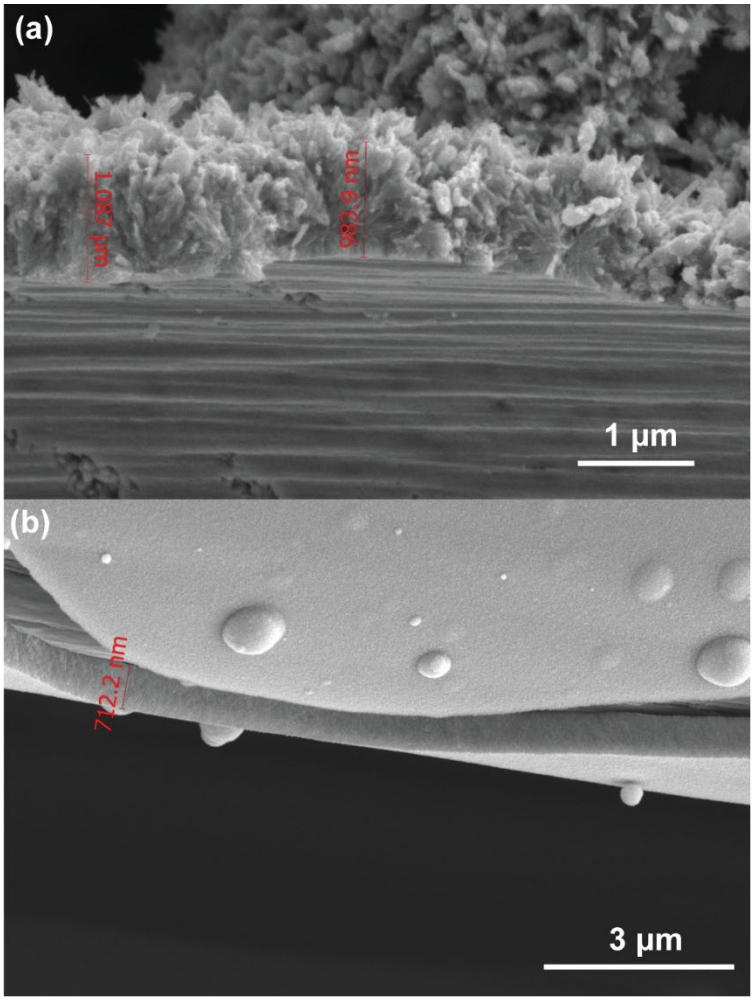


Figure 4.3. Cross-section SEM images of (a) CC/γ-MnO_2 and (b) CC/ε-MnO_2.

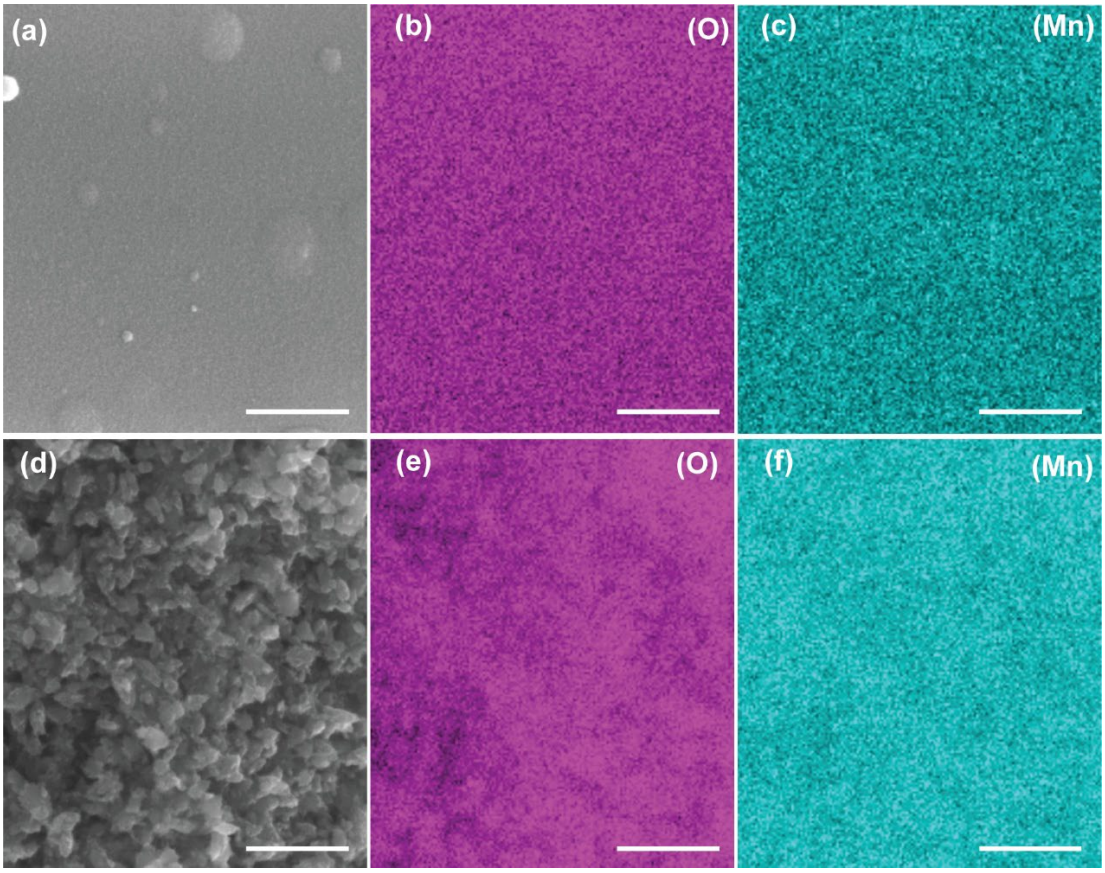


Figure 4.4 SEM and EDS images of (a-c) CC/ε-MnO_2 and (d-f) CC/γ-MnO_2. Scale bars are 1 μm.

SEM images on **Figure 4.2** show the difference in the morphology of MnO_2 deposited on CC at different temperatures. Through the process of electrodeposition, the CC was completely covered with ε-MnO_2 (**Figure 4.2 a-d)** and γ-MnO_2 (**Figure 4.2 e-h).** The electrodeposited at 20°C resulted on MnO_2 with fine nanosheet features. Meanwhile, electrodeposition at high temperature results in a rough feature of MnO_2. The differences in the morphology of the two samples synthesized using the same electrolyte suggest that different phases were obtained. Although the two samples has

around the same MnO_2 mass loading, their film thickness is different. **Figure 4.3 a** and **b** shows that electrodeposited γ-MnO_2 is thicker than the electrodeposited ε-MnO_2. γ-MnO_2 a thickness of 983 nm to 1 μm. Meanwhile, electrodeposited ε-MnO_2 nanosheet has a thickness of 712 nm. Energy-dispersive X-ray spectroscopy (EDS) elemental mapping analysis on a CC/ MnO_2 revealed a uniform distribution of the Mn and O signals (**Figure 4.3**). However, the distribution of the Mn and O signals for the γ-MnO_2 seems stronger than that ε-MnO_2.

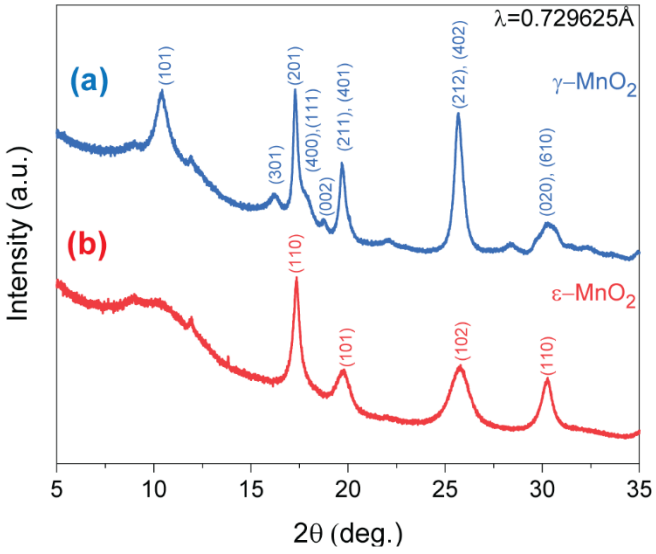


Figure 4.5 HRXRD of (a) γ-MnO_2 and (b) ε-MnO_2 electrodeposited on a carbon substrate.

MnO_2 electrodeposited on carbon substrates typically appears amorphous due to the broad peak contributed from carbon. High resolution XRD from the Stanford Radiation Lightsource (SSRL) using monochromatic X-rays with an incident

wavelength of 0.729625 Å was utilized to confirm the formation of γ-MnO_2 and ε-MnO_2. Comparing the XRD peaks of the two polymorphs, γ-MnO_2 shows sharper peaks than the ε-MnO_2. This indicates that γ-MnO_2 is more crystalline than ε-MnO_2. The major XRD peaks of MnO_2 on **Figure 4.5a** appeared at 2θ angles of 10.4°, 17.3°, 19.7°, and 25.7°, which corresponds to crystallographic planes (*hkl*) of (101), (201), (211), and (212), respectively. These can be attributed to the crystallographic phase of γ-MnO_2.[16] The XRD peaks of MnO_2 on **Figure 4.5b** appeared at 2θ angles of 17.3°, 19.9°, 25.8°, and 30.2° °, which corresponds to crystallographic planes (*hkl*) of (110), (101), (102), and (110), respectively. These peaks can be attributed to ε-MnO_2 (JCPDS 30-0820).

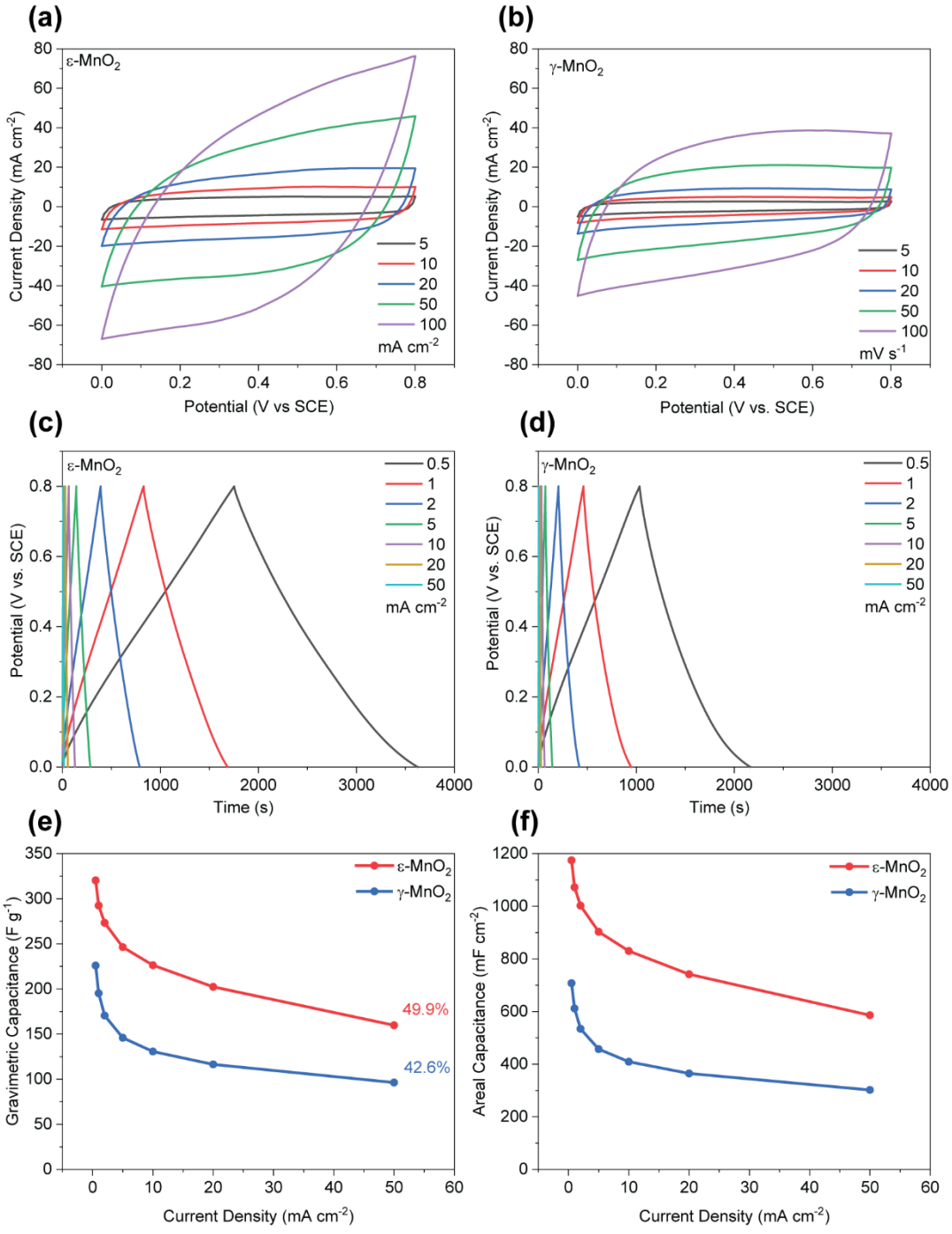


Figure 4.6. Cyclic voltammetry (CV) of (a) ε-MnO_2 and (b) γ-MnO_2. Galvanostatic charging and discharging (GCD) curves of (c) ε-MnO_2 and (d) γ-MnO_2. Calculated (e) gravimetric and (f) areal capacitance of ε-MnO_2 and γ-MnO_2.

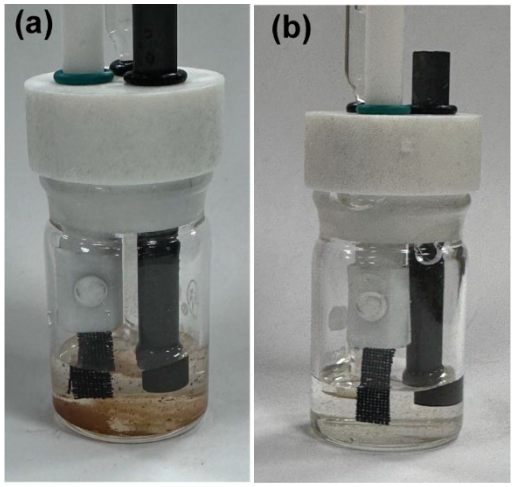


Figure 4.7 Digital images of (a) CC/ε-MnO_2 and (b) CC/γ-MnO_2 after electrochemical testing.

The electrochemical performance of the electrodeposited MnO_2 electrodes with the same mass loading of 3 mg/cm^{-2} were first evaluated in 3M LiCl solution as the electrolytes, and carbon rod and SCE as the counter and reference electrodes, respectively. In comparison to CC/γ-MnO_2, the CC/ε-MnO_2 showed substantially increased area in their cyclic voltammograms (CV), proving that amorphous phase has more pseudocapacitance than crystalline phase (**Figure 4.6a, b)**. The galvanostatic charging/discharging (GCD) profile of CC/ε-MnO_2 also showed longer charging-discharging time at different current densities than CC/γ-MnO_2, suggesting higher capacitance (**Figure 4.6 c,d**). The gravimetric and areal capacitance of the two electrodes were calculated from the GCD. The CC/ε-MnO_2 achieved higher capacitance than CC/γ-MnO_2 (**Figure 4.6e, f**). At the current density of mA cm^{-2}, CC/ε-MnO_2 achieved a gravimetric capacitance of 320.3 F g^{-1} (areal capacitance of 1174.4 mF cm^{-2}) and retained 49.9% if it at 50mA cm^{-2}. Meanwhile, CC/γ-MnO_2 achieved a

gravimetric capacitance of 225.9 F g^{-1} (areal capacitance of 7.7.8 mF cm^{-2}) at the same current density and retained 42.6% of it at 50 mA cm^{-2}. The high gravimetric and areal capacitance of CC/ε-MnO_2 compared to the CC/γ-MnO_2 is likely due to higher degree of disorder ε-phase which exhibiting better transport kinetics.[28,29] Previous reports stated that charge storage in amorphous MnO_2 takes place mainly on the surface.[2,30] Given that ε-phase is more amorphous than the γ-phase of MnO_2, the capacitance the of ε-MnO_2 based on the surface redox should be higher than the more crystalline one. The results here follow the trend from previous studies in the lietrature.[28–30]

After electrochemical testing in 3M LiCl, great amount of exfoliated MnO_2 was observed for CC/ε-MnO_2 (**Figure 4.7a**). Meanwhile, these precipitates observed in the electrolyte are less for CC/γ-MnO_2 (**Figure 4.7b**) This is likely related to the stability of different phases of MnO_2.[14] Although ε-MnO_2 delivers higher capacitance than the γ-MnO_2, its stability can become problematic.

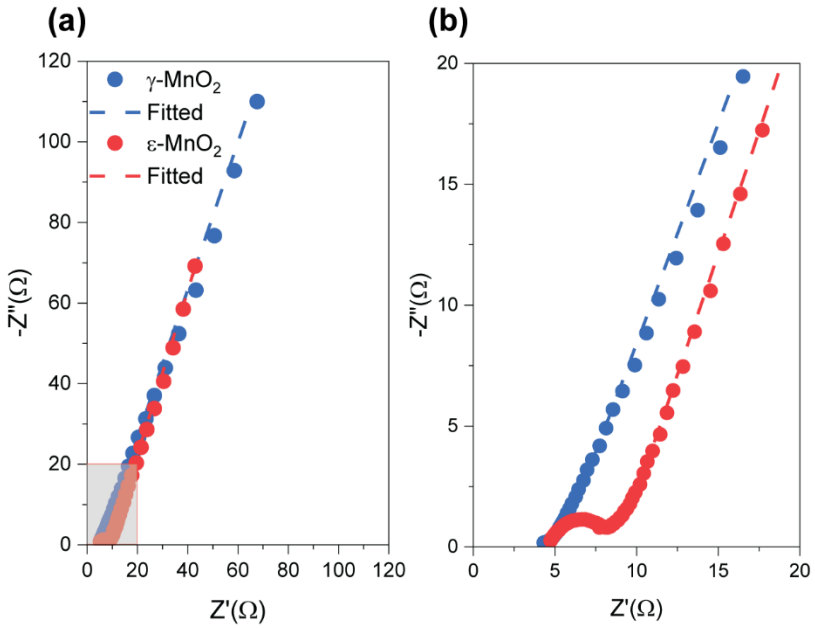


Figure 4.8. (a) Nyquist plot of CC/ε-MnO_2 and CC/γ-MnO_2 in 3M LiCl. (b) Nyquist plot of CC/ε-MnO_2 and CC/γ-MnO_2 highlighting the high frequency region.

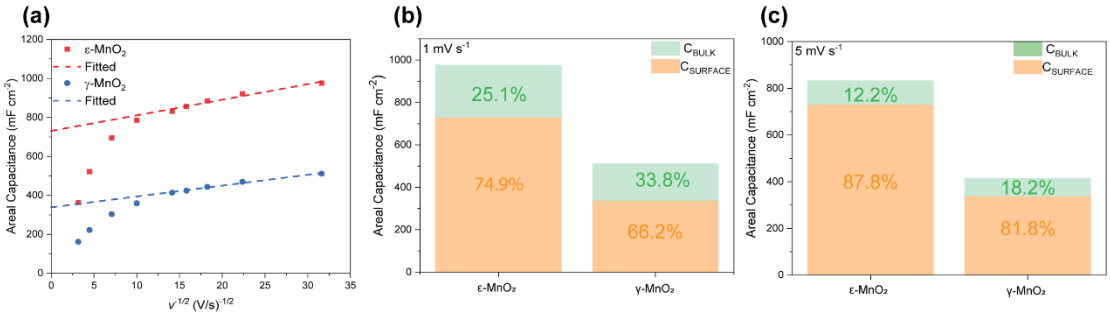


Figure 4.9 (a) Plot of areal capacitance versus $v^{-1/2}$ for CC/ε-MnO_2 and CC/γ-MnO_2. Capacitance contributed by the surface obtained from the slope of the linear fit. (b) Histogram illustration of capacitance contributions in CC/ε-MnO_2 and CC/γ-MnO_2 at a scan rate of 1 mV s^{-1}. (c) Histogram illustration of capacitance contributions in CC/ε-MnO_2 and CC/γ-MnO_2 at a scan rate of 5 mV s^{-1}.

Electrochemical impedance spectroscopy was performed for CC/ε-MnO_2 and CC/γ-MnO_2. The data were fitted with proper equivalent circuits (**Figure 4.8a**). At high frequency, the series resistances of CC/γ-MnO_2 and CC/ε-MnO_2 are comparable. However, CC/ε-MnO_2 has high charge transfer resistance. This shows that the gamma phase of MnO_2 is more conductive than the epsilon phase. The following results are consistent with the literature.[13] We quantitative analyzed the capacitance contribution by the surface and the bulk using the Trasatti method.[23,26,31] The areal capacitance based on the area of the electrodes were calculated from the cyclic voltammetry curves obtained from the scan rates ranging from 1-100 mV s^{-1} and plotted against $v^{-1/2}$ (v is scan rate) (**Figure 4.9a**). Linear fit was extrapolated at low scan rates and the determined the y-intercept ($v \rightarrow +\infty$) which represents the areal capacitance contributed by the surface ($C_{SURFACE}$). At 1mV s^{-1}, capacitance of CC/γ-MnO_2 and CC/ε-MnO_2 are both mainly from the surface (**Figure 4.9b**). Although γ-MnO_2 has lower than areal capacitance than ε-MnO_2, 33.8% of the total capacitance of γ-MnO_2 is contributed from the bulk. As the scan rate increases to 5 mV s^{-1}, the contribution from the surface was further increased to 87.8% and 81.8% for CC/ε-MnO_2 and CC/γ-MnO_2, respectivelyb (**Figure 4.8c**). These results relate to the difference between the crystal structure of ε-MnO_2 and γ-MnO_2.

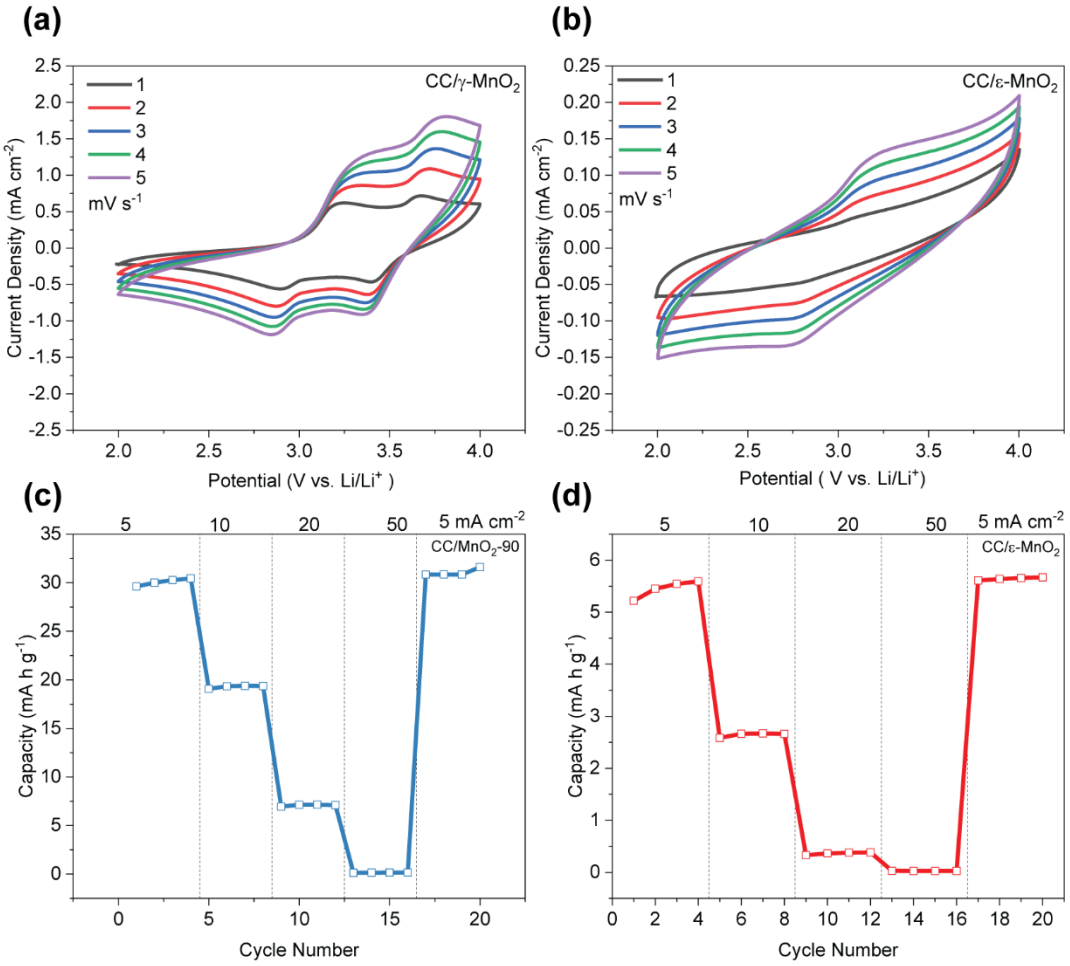


Figure 4.10 CV curves of (a) CC/γ-MnO_2 and (b)CC/ε-MnO_2 at the potential window of 2-4V vs Li/Li^+. Calculated specific capacity of (c) CC/γ-MnO_2 and (d)CC/ε-MnO_2.

Electrochemical performance of ε-MnO_2 and γ-MnO_2 were also evaluated in non-aqueous system using 1M LiFSI in DEE as the electrolyte. Coin cell devices were fabricated with CC/MnO2 as the cathode and Li metal as the anode separated by a Celgard membrane separator**.** Ensure the better contact between the cathode electrode and the current collector, MnO_2 were only deposited on one side of the carbon substrate. This was conducted by covering one side of the substrates with a plastic film. Coin cell

configuration was chosen in this study to prevent the evaporation of the DEE solvent. **Figure 4.10a** and **4.10b** shows the CV curves of CC/γ-MnO_2 and CC/ε-MnO_2 at the potential window of 2-4V vs Li/Li^+. At different scan rates, the CC/γ-MnO_2 shows a total of four peaks on CV curves (**Figure 4.10a**). Meanwhile, CC/ε-MnO_2 shows only two peaks (**Figure 4.10b**). Both the CV of γ-MnO_2 shows and ε-MnO_2 have peaks at around 3.2V and 2.8 V which corresponds to the oxidation and reduction of the Mn, respectively. As mentioned above, the γ-MnO_2 crystal structure has 2x1 and 1x1 tunnels that allow efficient diffusion of the ion. Sun et al. conducted a systematic first-principles evaluation on the physicochemical properties of MnO_2 polymorphs.[14] They found that Li-ion diffusion in the inter/cross-layer of ε-MnO_2 was found to be challenging due to the presence of densely packed MnO_6 octahedral.[14] In contrary, because of its the complex crystal structure, γ-MnO_2 allows better Li-ion transport kinetics especially at the vacancy-diluted limit.[14] Due to these tunnel structures, crystal structure of the electrodeposited γ-MnO_2 can go through structural transformation correspond to the Li-ion insertion and extraction as the Mn undergo oxidation or reduction. Alfaruqi et al. conducted a study on the structural transformation in γ-MnO_2 during electrochemical reaction in a zin-ion battery using *in situ* Synchrotron XANES and XRD.[32] Similar to their work, the CV curves of the γ-MnO_2 in this work have two peaks on the discharge as well as two peaks on the changing profile. Alfaruqi et al. suggest that these extra peaks are due to the structural transformation during intercalation and de-intercalation of the ion.[32] From their work, they concluded that the electrochemical mechanism of γ-MnO_2 cathode and Zn is subjected to structural

transformation of an orthorhombic Mn(IV) phase to a spinel-type Mn(III) phase ($ZnMn_2O_4$) and two new intermediary Mn(II) phases, namely, γ-Zn_xMnO_2 (tunnel-type) and L-Zn_yMnO_2 (layered-type).[32] We hypothesized that this could also happen in the electrodeposited γ-MnO_2. The two peaks at the charging and discharging profile of the CV curves represent the redox reaction of Mn as well as the structural transformation. As the scan rate increases, the peak position remains at the same potential suggesting that structural transformation is stable.[33] Further analysis on the structural property during charging and discharging such *as in situ* synchrotron XRD and XANES studies as well as *ex situ* TEM are needed.

The gravimetric capacity of the electrodeposited MnO_2 electrodes were calculated from the galvanostatic discharge curve. Both the CC/ε-MnO_2 and CC/γ-MnO_2 were cycled at the current density of 5, 10, 20, and 50 mA cm^{-2}. **Figure 4.10c** and **4.10d** shows the gravimetric capacity of the CC/γ-MnO_2 and CC/ε-MnO_2, respectively. At the current density of 5 mA cm^{-2}, CC/γ-MnO_2 achieved a capacity 30.5 mA h g^{-1} which is 6 times higher than the capacity of the CC/ε-MnO_2 (5.6 mA h g^{-1}). At high current density of 50 mA cm^{-2}, CC/γ-MnO_2 achieved a capacity of 0.16 mA h g^{-1}. The higher performance of the γ-MnO_2 compared to that of ε-MnO_2 is likely due to the tunneled structures of the γ-phase which allows rapid Li-ion transport. In addition, conductivity of the γ-MnO_2 also plays a role in achieving higher capacity than ε-MnO_2.

4.5 Conclusion

In this work, we demonstrated the behavior between the two types of electrodeposited MnO_2 polymorphs with different crystal structures. Electrodeposition at high temperature leads to the formation of γ-MnO_2 which has an intergrowth structure consisting of 2x1 and 1x1 tunnel domains. Meanwhile, electrodeposition at room temperature leads to the formation of ε-MnO_2, which has highly disorder structure due to partial occupancy of Mn^{+4} at the cation. Both polymorphs show advantages and disadvantages depending on the operating system used. At aqueous system, ε-MnO_2 achieved a gravimetric capacitance of 320.3 F g^{-1} at the current density of 0.5 mA cm^{-2} which is higher than that of γ-MnO_2 (225.9 F g^{-1}) at the same current density. This is due to its disordered nature of ε-phase which allows more redox reaction with proton to occur. The capacitance of ε-MnO_2 mostly originating from fast reversible surface electrochemical reactions. In comparison, about 30% of γ-MnO_2 capacitance is from the bulk. However, in the system where charge storage is dominated by ion intercalation and de-intercalation reaction, γ-MnO_2 achieved a capacity of 30.5 mA h g^{-1} which is 6 times higher than that of ε-MnO_2. The tunneled crystal structure of the γ-MnO_2 allows faster diffusion of the ions which results in higher capacity than the phase without tunnels. Overall, each phase of MnO_2 has its own advantages and disadvantages depending on operating system. The findings from this study open avenues for understanding the complex charge storage mechanisms of MnO_2 polymorphs and other metal oxide-based materials.

4.6 References

1. Bhojane, P. Recent advances and fundamentals of Pseudocapacitors: Materials, mechanism, and its understanding. *Journal of Energy Storage* **45**, 103654 (2022).
2. Augustyn, V., Simon, P. & Dunn, B. Pseudocapacitive oxide materials for high-rate electrochemical energy storage. *Energy Environ. Sci.* **7**, 1597–1614 (2014).
3. Yao, B. *et al.* Efficient 3D Printed Pseudocapacitive Electrodes with Ultrahigh MnO2 Loading. *Joule* **3**, 459–470 (2019).
4. Pinongcos, A. B., Xue, X., Chandrasekaran, S., Worsley, M. A. & Li, Y. Innovative Electrode Design for Low-Temperature Electrochemical Energy Storage: A Mini Review. *Energy Fuels* **39**, 6078–6096 (2025).
5. Li, X. *et al.* A Static Tin–Manganese Battery with 30000-Cycle Lifespan Based on Stabilized Mn3+/Mn2+ Redox Chemistry. *ACS Nano* **17**, 5083–5094 (2023).
6. Xue, X. *et al.* Regulated Interfacial Proton and Water Activity Enhances Mn2+/MnO2 Platform Voltage and Energy Efficiency. *ACS Energy Lett.* **8**, 4658–4665 (2023).
7. Song, Y. *et al.* Ostwald Ripening Improves Rate Capability of High Mass Loading Manganese Oxide for Supercapacitors. *ACS Energy Lett.* **2**, 1752–1759 (2017).
8. Julien, C. M. & Mauger, A. Nanostructured MnO2 as Electrode Materials for Energy Storage. *Nanomaterials* **7**, 396 (2017).

9. Huang, Y. *et al.* Novel Insights into Energy Storage Mechanism of Aqueous Rechargeable Zn/MnO2 Batteries with Participation of Mn2+. *Nano-Micro Lett.* **11**, 49 (2019).
10. Tompsett, D. A. & Islam, M. S. Electrochemistry of Hollandite α-MnO2: Li-Ion and Na-Ion Insertion and Li2O Incorporation. *Chem. Mater.* **25**, 2515–2526 (2013).
11. Song, M., Tan, H., Chao, D. & Fan, H. J. Recent Advances in Zn-Ion Batteries. *Advanced Functional Materials* **28**, 1802564 (2018).
12. Pandit, B. *et al.* Regulated electrochemical performance of manganese oxide cathode for potassium-ion batteries: A combined experimental and first-principles density functional theory (DFT) investigation. *Journal of Colloid and Interface Science* **633**, 886–896 (2023).
13. Xiao, X. *et al.* Ultrahigh-Loading Manganese-Based Electrodes for Aqueous Batteries via Polymorph Tuning. *Advanced Materials* **35**, 2211555 (2023).
14. Sun, W., Orme, C. A., Worsley, M. A. & Wan, L. F. First-principles evaluation of MnO2 polymorphs as cathode material in lithium-ion batteries. *Sustainable Energy Fuels* **8**, 2718–2729 (2024).
15. Kim, C.-H. *et al.* The structure and ordering of ε-MnO2. *Journal of Solid State Chemistry* **179**, 753–774 (2006).
16. Hatakeyama, T., Okamoto, N. L. & Ichitsubo, T. Thermal stability of MnO2 polymorphs. *Journal of Solid State Chemistry* **305**, 122683 (2022).

17. Liu, L. *et al.* Polymorph γ-MnO2 with Optimal Phase Composition for Stable Oxygen Evolution Reaction in Acid. *ACS Sustainable Chem. Eng.* **12**, 17613–17620 (2024).
18. Chou, S., Cheng, F. & Chen, J. Electrodeposition synthesis and electrochemical properties of nanostructured γ-MnO2 films. *Journal of Power Sources* **162**, 727–734 (2006).
19. Zhang, M., Chen, Y., Yang, D. & Li, J. High performance MnO2 supercapacitor material prepared by modified electrodeposition method with different electrodeposition voltages. *Journal of Energy Storage* **29**, 101363 (2020).
20. Patil, R. B., Yadav, A. D., Kanamadi, C. M. & Patil, S. P. Electrochemical advancements: MnO2-based electrode materials for supercapacitors. *Ionics* **31**, 1203–1231 (2025).
21. Lin, T. Y. *et al.* Shape Matters: Understanding the Effect of Electrode Geometry on Cell Resistance and Chemo-Mechanical Stress. *J. Electrochem. Soc.* **171**, 100515 (2024).
22. White, M. *et al.* Recent Advances in Scalable, High-Mass Loaded Electrodes for Grid-Scale Energy Storage. *Advanced Materials* **n/a**, 2417128.
23. Lin, D. *et al.* 3D-Printed Graded Electrode with Ultrahigh MnO2 Loading for Non-Aqueous Electrochemical Energy Storage. *Advanced Energy Materials* **13**, 2300408 (2023).
24. Xue, X. *et al.* Interpenetrated Structures for Enhancing Ion Diffusion Kinetics in Electrochemical Energy Storage Devices. *Nano-Micro Lett.* **16**, 255 (2024).

25. Luo, Y. *et al.* Stable cycling of high-mass loaded MnO 2 electrodes for sodium-ion batteries. *EES Batteries* **1**, 922–934 (2025).
26. Ardizzone, S., Fregonara, G. & Trasatti, S. “Inner” and “outer” active surface of RuO2 electrodes. *Electrochimica Acta* **35**, 263–267 (1990).
27. Cruz-Cabeza, A. J., Reutzel-Edens, S. M. & Bernstein, J. Facts and fictions about polymorphism. *Chem. Soc. Rev.* **44**, 8619–8635 (2015).
28. Xue, C. *et al.* Research advances of amorphous metal oxides with the feature of Pseudocapacitance behavior in Lithium ion battery. *Journal of Colloid and Interface Science* **700**, 138331 (2025).
29. Yan, S. *et al.* Research Advances of Amorphous Metal Oxides in Electrochemical Energy Storage and Conversion. *Small* **15**, 1804371 (2019).
30. Ragupathy, P., Vasan, H. N. & Munichandraiah, N. Synthesis and Characterization of Nano- MnO2 for Electrochemical Supercapacitor Studies. *J. Electrochem. Soc.* **155**, A34 (2007).
31. Baronetto, D., Krstajić, N. & Trasatti, S. Reply to “note on a method to interrelate inner and outer electrode areas” by H. Vogt. *Electrochimica Acta* **39**, 2359–2362 (1994).
32. Alfaruqi, M. H. *et al.* Electrochemically Induced Structural Transformation in a γ-MnO2 Cathode of a High Capacity Zinc-Ion Battery System. *Chem. Mater.* **27**, 3609–3620 (2015).
33. Liu, T. *et al.* Correlation between manganese dissolution and dynamic phase stability in spinel-based lithium-ion battery. *Nat Commun* **10**, 4721 (2019).

Chapter 5
Outlook

Over the past decade, numerous strategies have been pursued to tackle the challenges of developing high-performance electrochemical energy storage (EES) systems for wide range of applications. Despite significant progress, further research and development are needed to enable the widespread implementation of these devices in real-world applications. Beyond the effect of electrolyte, performance degradation of EES devices is caused by slow interfacial kinetics at the electrode/electrolyte interface, sluggish ion diffusion within the electrode, and limitations in electrode conductivity and ion accessibility.

In this dissertation, various strategies are proposed and demonstrated to address current challenges of EES electrodes. In the first chapter, we introduced different types of EES devices and their limitations. Second chapter focused on enhancing the intrinsic properties of porous carbon material to increase its energy density and maintain high power density even at low operating temperatures. The third chapter highlighted the development of new ink formation to achieve thin, light, freestanding electrode that could operate under different mechanical stress. Lastly, the fourth chapter opens new avenues on unraveling the complex charge storage properties of an earth-abundant pseudocapacitive material.

Moving forward, improving electrode-electrolyte interface and device fabrication remain critical for enhancing the performance of electrochemical energy storage devices especially at extreme operating conditions, such as low temperatures. Reducing

charge transfer energy barrier at electrode–electrolyte interface, coupling structural and surface engineering, shortening ion diffusion path, and further understanding the material properties are some of the new research areas that are needs to be considered when developing energy storage devices for wide range of applications.

The high energy barrier in the charge-transfer process substantially reduces EES device's capacity at low temperatures. This is closely related to the strength of solvated ion binding energy at the interface. One potential solution is to modify the geometric surface of the electrode. Lu et al. constructed a carbon-based anode material with a non-coplanar sp^2/sp^3 hybridized carbon network, which promotes local charge accumulation and increase Li^+ ion affinity compared to a flat surface, thereby reducing the desolvation energy barrier for charge-transfer process.[1] They synthesized multilayer onion-like carbon nanospheres anchored on a dodecahedral carbon framework with a non-coplanar Riemannian surface and a positively curved structure. A LIB device using this material achieved a high room temperature capacity of 823 mAh g^{-1} at a current density of 0.1 A g^{-1}, and retained 85.9% of its room temperature capacity at -20°C. Although still in its early stages, this experimental work, supported by computational studies, shows promise for addressing sluggish charge-transfer processes at low temperatures. This strategy could potentially be extended to non-carbon materials as well.

One should consider coupling structural and surface engineering to enhance EES devices. Dendrite growth poses a significant challenge to the performance of EES devices, particularly in alkaline metal batteries, at low temperatures. To mitigate this,

electrodes must have good ion-accessibility and a homogeneous active surface area.[2] Coupling structural and surface engineering can increase ion accessibility area and better control the active surface. Additive manufacturing techniques offer a way to improve performance by printing layers of materials with different Li affinities, optimizing material composition for low-temperature operations. The development of specialized inks and resins that precisely control material composition is essential to advancing this approach.

To overcome sluggish ion diffusion within the electrodes, researchers have developed 3D-printed lattice structures.[3–9] However, even when assembling a device using two 3D-printed lattices, devices can still experience high resistance due to the tortuous and extended ion transport pathways, which poses challenges for low-temperature performance. Addressing these issues is crucial for effective operation at low temperatures. Three common 3D architectures: interdigitated, concentric, and aperiodic, have been developed over the past decade to optimize ion diffusion.[10,11] Most studies on these designs have been computational or focused on ambient temperature applications.[11,12] Advances in state-of-the-art additive manufacturing techniques now allow for the creation of complex and customizable electrode and device structures, helping to reduce time and cost for large-scale production.[9]

Lastly, as technologies advance, gaining a deeper understanding of electrode behavior under extreme conditions, such as low temperature environments, becomes increasing important. Although *ex situ* characterizations give insight into the materials, the properties of energy storage material could change before and after operation. *In*

situ and *operando* measurements are widely used by recent studies to give a full picture on the mechanism and properties of the materials.[13] The distinction between *situ* and *operando* are often confusing, particularly by early-career researchers. *In situ* refers to the characterization of a material or system at its relevant environment (e.g. the electrode in the electrolyte). Meanwhile, *operando* refers to the characterization of the materials during actual operation. [13,14] Yan et al. did ex *situ* and *in situ* microscopy investigations to demonstrate the relationship between the operating temperature and the Li deposition.[15] Xue et al. used *in situ* atomic force microscopy to confirm the redox mediation mechanism of VO^{2+}/VO_2^{+} manganese dioxide (MnO2) deposition/dissolution. Lin et al. used *operando* transmission X-ray microscopy to understand the role of Sb in improving the cycling stability of Sn compared to pure Sn anodes for Li ion batterries.[16]

As researchers continue to explore this critical aspect of EES, this work aims to encourage collaborative efforts across research institutions to advance the development of robust EES devices and facilitate their widespread implementation in real-world applications.

5.2 References

1. Lu, Z. *et al.* Riemannian Surface on Carbon Anodes Enables Li-Ion Storage at −35 °C. *ACS Cent. Sci.* **8**, 905–914 (2022).
2. Chen, K. *et al.* Flower-shaped lithium nitride as a protective layer via facile plasma activation for stable lithium metal anodes. *Energy Storage Materials* **18**, 389–396 (2019).
3. Yao, B. *et al.* Printing Porous Carbon Aerogels for Low Temperature Supercapacitors. *Nano Lett.* **21**, 3731–3737 (2021).
4. Lin, D. *et al.* 3D-Printed Graded Electrode with Ultrahigh MnO2 Loading for Non-Aqueous Electrochemical Energy Storage. *Advanced Energy Materials* **13**, 2300408 (2023).
5. Xue, X. *et al.* Interpenetrated Structures for Enhancing Ion Diffusion Kinetics in Electrochemical Energy Storage Devices. *Nano-Micro Lett.* **16**, 255 (2024).
6. Reale Batista, M. D. *et al.* Design and additive manufacturing of optimized electrodes for energy storage applications. *Carbon* **205**, 262–269 (2023).
7. Zhang, M. *et al.* A 3D-Printed Proton Pseudocapacitor with Ultrahigh Mass Loading and Areal Energy Density for Fast Energy Storage at Low Temperature. *Advanced Materials* **35**, 2209963 (2023).
8. Yao, B. *et al.* 3D-Printed Structure Boosts the Kinetics and Intrinsic Capacitance of Pseudocapacitive Graphene Aerogels. *Advanced Materials* **32**, 1906652 (2020).

9. Chandrasekaran, S., Lin, D., Li, Y. & Worsley, M. A. Aerogels, additive manufacturing, and energy storage. *Joule* **7**, 866–883 (2023).
10. Long, J. W., Dunn, B., Rolison, D. R. & White, H. S. 3D Architectures for Batteries and Electrodes. *Advanced Energy Materials* **10**, 2002457 (2020).
11. Hung, C.-H., Allu, S. & Cobb, C. L. Modeling Current Density Non-Uniformities to Understand High-Rate Limitations in 3D Interdigitated Lithium-ion Batteries. *J. Electrochem. Soc.* **168**, 100512 (2021).
12. Li, X., Li, H., Fan, X., Shi, X. & Liang, J. 3D-Printed Stretchable Micro-Supercapacitor with Remarkable Areal Performance. *Advanced Energy Materials* **10**, 1903794 (2020).
13. Zoric, M. R., Fabbri, E., Herranz, J. & Schmidt, T. J. In Situ and Operando Spectroscopic Techniques for Electrochemical Energy Storage and Conversion Applications. *J. Phys. Chem. C* **128**, 19055–19070 (2024).
14. Nelson Weker, J. & Toney, M. F. Emerging In Situ and Operando Nanoscale X-Ray Imaging Techniques for Energy Storage Materials. *Advanced Functional Materials* **25**, 1622–1637 (2015).
15. Yan, K. *et al.* Temperature-Dependent Nucleation and Growth of Dendrite-Free Lithium Metal Anodes. *Angewandte Chemie* **131**, 11486–11490 (2019).
16. Lin, T. C. *et al.* Understanding Stabilization in Nanoporous Intermetallic Alloy Anodes for Li-Ion Batteries Using Operando Transmission X-ray Microscopy. *ACS Nano* **14**, 14820–14830 (2020).